LOS ALAMOS SCIENTIFIC LABORATORY
of the
University of California
LOS ALAMOS, NEW MEXICO

Environmental Effects of the Kiwi-TNT Effluent:
A Review and Evaluation

LOS ALAMOS SCIENTIFIC LABORATORY
of the
University of California
LOS ALAMOS, NEW MEXICO

Environmental Effects of the Kiwi-TNT Effluent:

A Review and Evaluation

by
R. V. Fultyn

CONTENTS

ABSTRACT

The Kiwi Transient Nuclear Test (Kiwi-TNT) was a controlled excursion in which reactivity was inserted into a nuclear rocket engine prototype fast enough to vaporize a significant portion of the reactor core. The test studied the neutronic behavior of the reactor and the environmental effects of the radioactive materials released. This report discusses in detail only the determination of environmental effects.

The test was conducted at the Nuclear Rocket Development Station, Jackass Flats, Nevada, on January 12, 1965, at 1058 PST. The Los Alamos Scientific Laboratory collected environmental data from the test point to approximately 50 miles downwind. The U.S. Public Health Service monitored the neighborhood and collected milk samples in southern Nevada and California to beyond 200 miles downwind. The course of the effluent cloud was tracked by aircraft from the U. S. Public Health Service and EG&G.

From 5 to 20% of the reactor core was vaporized, with approximately 67% of the products from about 3×10^{20} fissions released to the effluent cloud. Radiation effects from the cloud passage were less than predicted in the pretest safety evaluation report. The maximum off-site, integrated, whole-body exposure was 5.7 mrad about 15 miles from the test point. No fresh fission products were detected in any of the milk samples.

FOREWORD

The principal concern of this report is to summarize and interpret all available data concerning the environmental effects of the Kiwi Transient Nuclear Test (Kiwi-TNT). In addition to data obtained by the Los Alamos Scientific Laboratory (LASL), the report includes summaries of data collected by other participating agencies, notably the U. S. Public Health Service (USPHS), the U.S. Weather Bureau (USWB), EG&G, Inc., and Pan American World Airways, Inc. This report collects under a single cover all the significant information about the environmental effects. Pertinent data and figures from referenced works are reproduced in this report to enable the reader to understand the overall interpretation of environmental effects. Some of the original reports received only limited distribution and their availability will decrease with time; the interested reader is referred to the source reports for fuller treatment of sampling, measurement, and analytical techniques and for details of the neutronics and mechanical aspects of the experiment.

I. INTRODUCTION

The Kiwi Transient Nuclear Test (Kiwi-TNT) was a controlled power excursion in which reactivity was inserted into a nuclear rocket engine prototype at an unusually high rate calculated to vaporize a significant portion of the reactor core. The objectives of this simulated reactor accident were to examine the material and neutronic behavior of the reactor and to study the effects of the radiation and radioactive materials released.

The reactor, including the core and pressure vessel, was, with few exceptions, a typical, late model Kiwi-B4. The nozzle was replaced with a mirror apparatus that permitted high-speed photography of the core top during the test. Coolant supply piping to the reactor shell was removed because no hydrogen coolant-propellant was used. A point worthy of emphasis is that to achieve a reactivity insertion rate sufficient to vaporize a significant fraction of the core, the control rod mechanisms were modified to rotate at approximately 100 times the normal rate.

The reactor core is extremely refractory, designed for normal operation above 2,000°C. Even in normal operation, the core materials are incandescent, and any abnormal operation that causes structural damage, so that core materials are expelled from the reactor by the exhausted coolant, produces a shower of sparks. In early tests, before many structural problems were solved, some fuel elements broke and were ejected from the nozzle with the exhaust gases. This spectacle resembled a Roman candle. Therefore,

in an experiment of the Kiwi-TNT type, it was apparent that the released vapor would be incandescent. Except for the pressure vessel normally used with a Kiwi reactor, the core was unshielded and uncontained; therefore, all vaporized and pulverized materials would be immediately released before any appreciable cooling could take place.

A few months before the test, the best neutronics estimates indicated that the excursion would produce approximately 9×10^{20} fissions, with approximately 1.8% of the core being vaporized, assuming that the carbon vapor was monoatomic, and would release the products from approximately 4×10^{20} fissions. A few days before the test, these estimates were revised to approximately 36% of the core vaporized and 75% of the fission products released, or the products from approximately 7×10^{20} fissions. There was no fission-product inventory in the reactor at the time of the test. As discussed later, the excursion produced 3.1×10^{20} fissions, 5 to 20% of the core was vaporized (assuming monoatomic carbon vapor), and approximately 67% of the fission products were released in the effluent cloud. The total energy release was about 1×10^4 MW-sec; an estimated 1% was kinetic energy. Normal runs of this type of reactor produced a maximum of about 5×10^5 MW-sec of energy.

Details of the neutronics and mechanical aspects of the experiment are given in References 1-4.

II. THE EXPERIMENTAL PLAN

The test was conducted at the Nuclear Rocket Development Station (NRDS), Jackass Flats, on January 12, 1965, at 1058 PST. Figure 1 shows the topography of the test point and downwind terrain out to approximately 50 miles. Jackass Flats and the Amargosa Desert form a flat plain, bordered by mountains, which slopes gently down to the southwest for about 30 miles from the test point. Death Valley, California, is approximately 50 miles from the test point. The LASL sampling array covered this entire area; the more distant stations are also shown in Fig. 1.

The weather requirements for the test were northeasterly winds in excess of 5 mph blowing toward 240° ± 20°, neutral to slightly unstable vertical temperature profile, nearly clear skies, and a reasonable certainty of persistence of these conditions to ensure that the effluent cloud would traverse the entire instrumented array.

For cloud sampling, LASL trailer-mounted equipment was located at approximately 10° intervals between 180 and 270° on arcs at 4,000, 8,000, and 16,000 ft, and at 6, 12, 25, and 50 miles from the test point. A typical sampling trailer contains an engine-driven generator, one or more high-volume air samplers with filter paper and charcoal cartridges as collection media, a cascade impactor for particle size measurement, and a set of cycling, high-volume samplers with filter paper collectors for timing cloud passage. The trailers are radio-equipped so that sampling equipment may be started and stopped remotely. Resin-coated trays for the collection of deposited activity were placed on stands near the trailers at each sampling location. Stations for collecting cloud deposition activity and reactor debris extended from 100 to 2,000 ft from the test point.

Collectors for particles and fragments of near-microscopic size consisted of resin-coated Mylar film on special frames, which also held large sheets of x-ray film for autoradiography of collected particles. After the event, the Mylar film was examined visually and microscopically to characterize the collected particles. The auto-radiographs helped to distinguish the radioactive particles from desert dust. Specially mounted groups of microscope slides were placed with the Mylar films to provide samples for microscopic examination and analysis. Approximately half of these close-range stations also contained large, 4 × 4 ft funnel-shaped hoppers to collect fragments large enough to separate by sieving. To correlate data between close- and long-range activity deposition, resin-coated trays identical to those used at the extended range stations were placed at 5° intervals around the reactor at distances of 500, 1,000, and 2,000 ft. The test point was on a railroad culvert damming a wash approximately 500 ft wide and 30 ft deep. Thus, many of the short-range stations were at levels below the reactor.

The Southwestern Radiological Health Laboratory (SWRHL) of the USPHS provided off-site radiation surveillance by aerial tracking of the effluent cloud, monitoring radiation dosage of the off-site population, and collecting environmental samples in southern Nevada and California. Twelve ground monitoring teams equipped with portable instruments tracked the cloud passage. Dose-rate recording instruments were placed at eight downwind locations bracketing the anticipated path of the effluent cloud. Film badges were issued to 157 people in Lathrop Wells, Amargosa Desert, and Death Valley. Forty-five routine air samplers were operated in Nevada, Utah, Arizona, and California, supplemented by 18 samplers at anticipated downwind locations. All these high-volume air samplers were equipped with filter papers and charcoal cartridges.

An Air Force U3-A aircraft carrying two USPHS monitors tracked the reactor effluent and assisted in positioning ground monitors. Two other PHS aircraft containing sampling equipment were used in cloud tracking, although their primary purpose was to determine cloud size and inventory.

Following the test, 74 milk samples were collected from two ranches in the Amargosa Desert and from 14 locations in southern California. The milk sampling program continued for approximately a week. Vegetation samples were obtained at most milk sampling locations; attempts were made to make these representative of the cows' feed but the forage samples were taken primarily as early indicators of areas of milk contamination rather than to yield cow intake-excretion data.[5]

An aircraft of the Nevada Aerial Tracking System, manned by EG&G personnel, tracked the effluent cloud from Death Valley over the Los Angeles area and terminated contact over the Pacific Ocean.[6]

Neutron and gamma radiation measurements

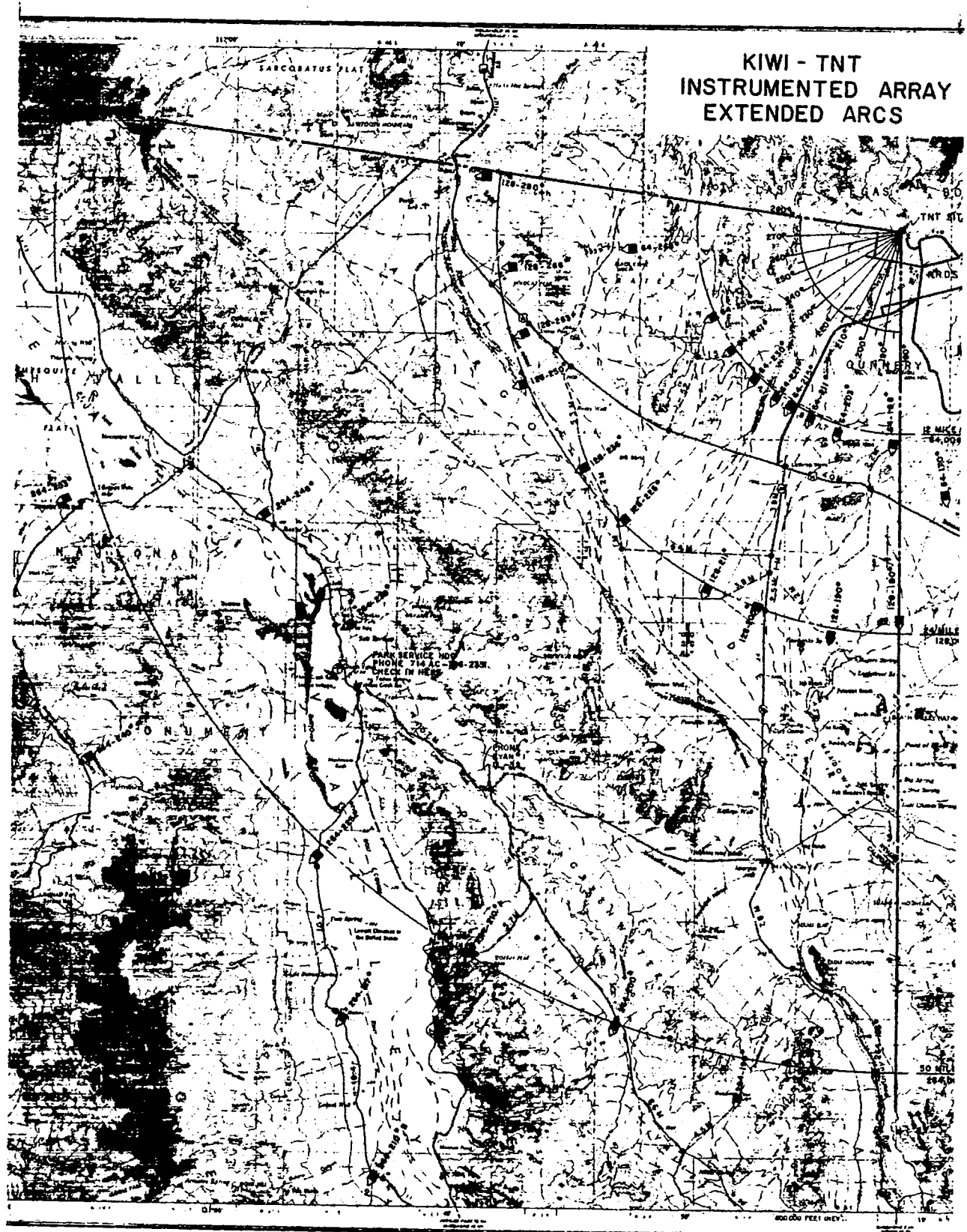**KIWI - TNT**
INSTRUMENTED ARRAY
EXTENDED ARCS

Fig. 1. Topography out to 50 miles downwind from test point showing instrumented array on extended arcs.

3

were obtained by LASL by methods used in other Kiwi reactor tests. Neutron integral fluxes and doses were determined by threshold detectors consisting of ^{239}Pu, ^{237}Np, and ^{238}U fission foils complemented by gold and sulfur activation detectors.[7] Gamma doses were measured by gamma-sensitive glass dosimeters and by dosimetry films. Combinations of these detectors were positioned near the reactor to measure the prompt radiation. Dosimetry films were placed at all cloud sampling stations downwind to indicate gamma doses from the radioactive effluent cloud and subsequent deposited activity. Gamma dose-rate detectors with remote readout equipment were placed around the test point, but concentrated downwind, out to 8,000 ft. Although the dose-rate instruments were inadequate to measure prompt radiation, they were useful in determining the decay of activity deposited around the test site.

For several days after the test, radiation surveys of the area were made by monitors from LASL and the Radiation Services of Pan American World Airways, Inc.; isodose rate contours were made from these hand-held instrument surveys to follow the decay of the deposited activity.

During decontamination of the test point area, recovered reactor fragments were placed in containers marked to indicate where they were found. After all locatable fragments had been recovered, they were sorted by size distribution and location. [8,9]

III. THE WEATHER

The material in this chapter is largely from WBRS-LA-9, "Analysis of Meteorological Data for the Kiwi-TNT Reactor Test" by Mueller and Wilson.[10]

The weather at the time of the test fulfilled the desired conditions in every respect: it was clear, windy, and mild. The winds were northeasterly at all levels, ranging from 14 to 27 knots. Persistent northeasterly winds were the result of a surface high-pressure cell centered over eastern Oregon. South of this high, a fairly strong pressure gradient over Nevada helped prevent surface winds from turning toward the northeast, as frequently results from daytime surface solar heating. In addition, a pressure ridge over the Pacific Northwest, combined with a weak low off Baja California, produced the desired northeasterly winds over NRDS. Synoptic charts of these conditions are shown in Fig. 2.

Temperature soundings made at the NRDS weather station a few minutes after run time, and in the Amargosa Desert at about the time of cloud arrival, were similar. The lapse rate was unstable near the surface, nearly neutral up to approximately 9,000 ft MSL, and more stable above that height. These temperature profiles are shown in Fig. 3.

Upper-air data for Jackass Flats and the Amargosa Desert shortly after the test are listed in Table I. Table II gives winds-aloft data from five stations near the test point for several hours before and after the test. Fallout hodographs made from these data and plotted from the test point using Jackass Flats data for 1100 PST, and from Lathrop Wells using its 1115 PST data are shown in Fig. 4. Air trajectories plotted from these and other wind data for 5,000, 7,000, and 9,000 ft MSL are shown in Fig. 5. The theoretical trajectories of the lower levels correspond well with actual trajectories constructed from aircraft tracking data, as can be seen by comparing Fig. 5 with Figs. 52 and 53. The small amount of shear in the lower winds (approximately 10° up to 2,500 ft above the surface) led one to expect a narrow cloud and deposition sector, with a centerline bearing of 215°. At higher altitudes the shear increased to about 25°, and a centerline bearing of 220° was suggested. These expectations were consistent with the cloud and deposition patterns constructed from sampling data, as discussed in Chapter VIII.

Two constant-level balloons (tetroons), released from the NRDS weather station at 1035 and 1133 PST on the day of the run, were tracked from the Lathrop Wells radar station and were first contacted approximately 6 miles from the release point. They were inflated to fly at 5,000 to 6,000 ft MSL, but considerable fluctuation in height occurred because of up- and downdrafts. The tracks of the tetroons plotted in Fig. 6 have been shifted about 2 miles to the west to simulate a release from the test point. This is considered to be valid because wind soundings from various stations in the area were similar at this time. The tracks were similar for about 15 miles south of the test point. Both balloons traveled this distance in about 40 minutes. Beyond this distance the tracks diverge, but both tetroons remained over areas where radioactive material from the effluent cloud was collected by ground-level samplers.
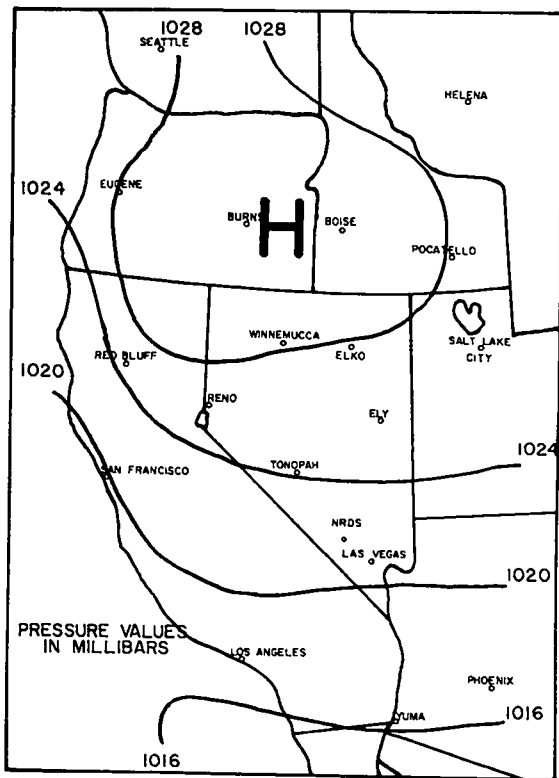
SURFACE ANALYSIS
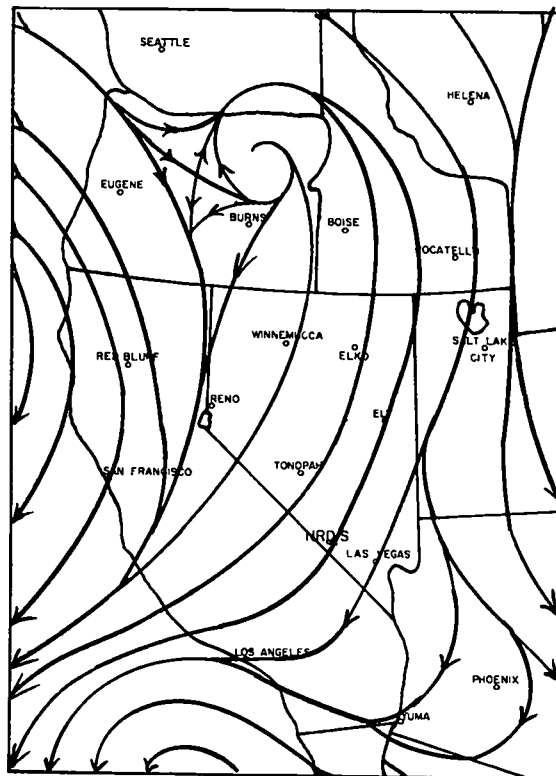
SECOND STANDARD LEVEL STREAMLINES
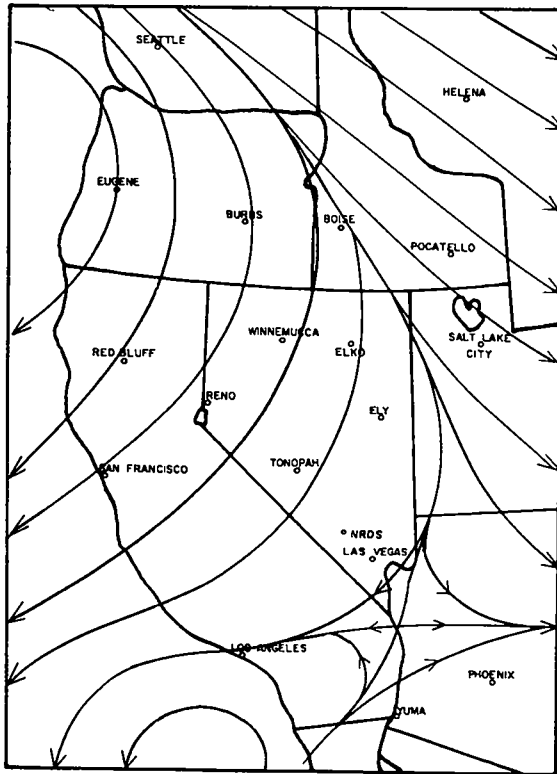
7000 FOOT MSL STREAMLINES

9000 FOOT MSL STREAMLINES

Fig. 2.   Meteorological conditions at 1000 PST, January 12, 1965.
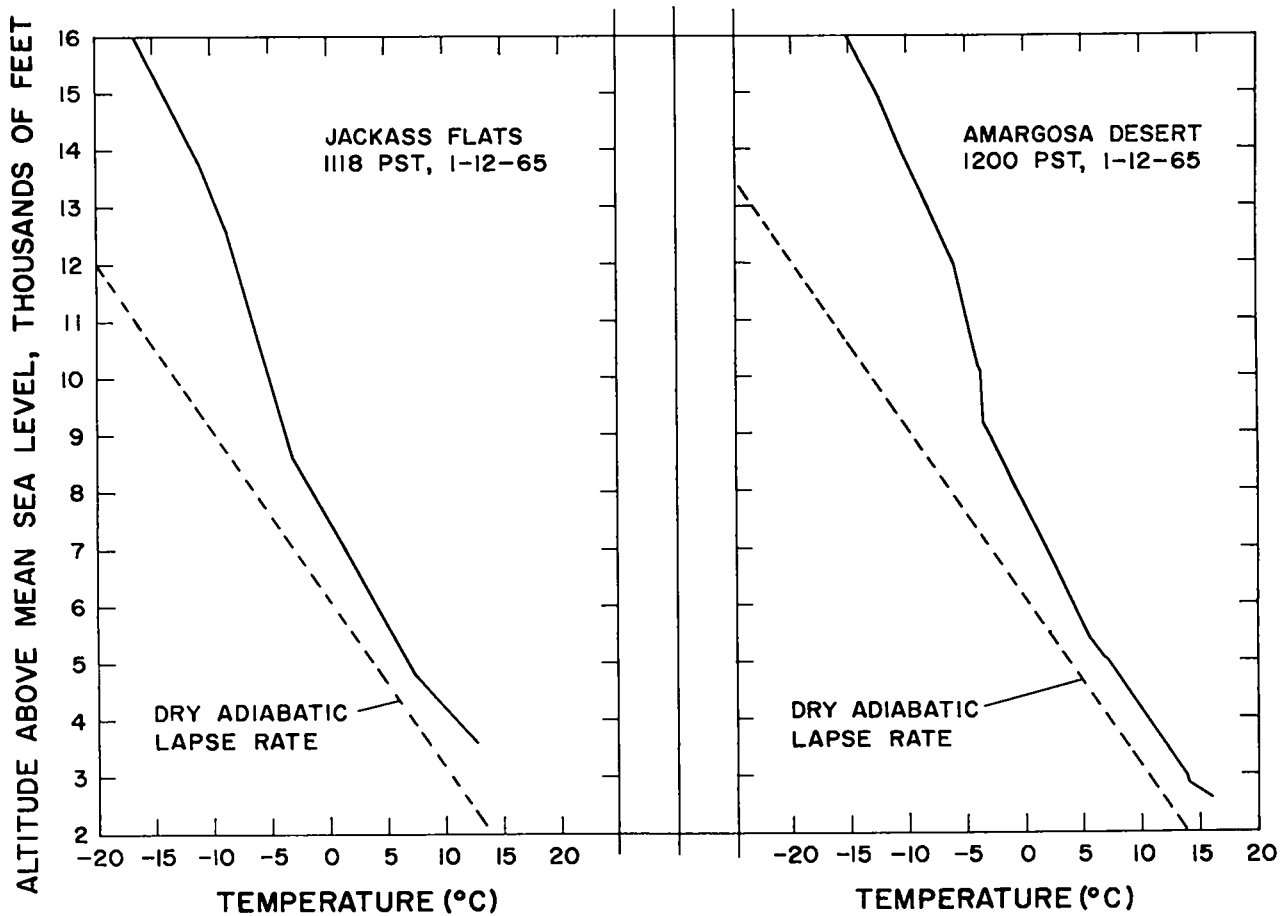
Fig. 3.   Temperature soundings.
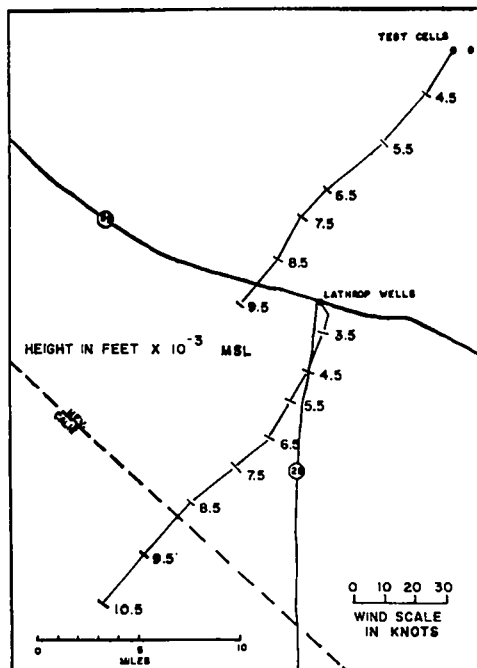
Fig. 4.   1100 PST NRDS and 1115 PST Lathrop Wells hodographs, January 12, 1965.
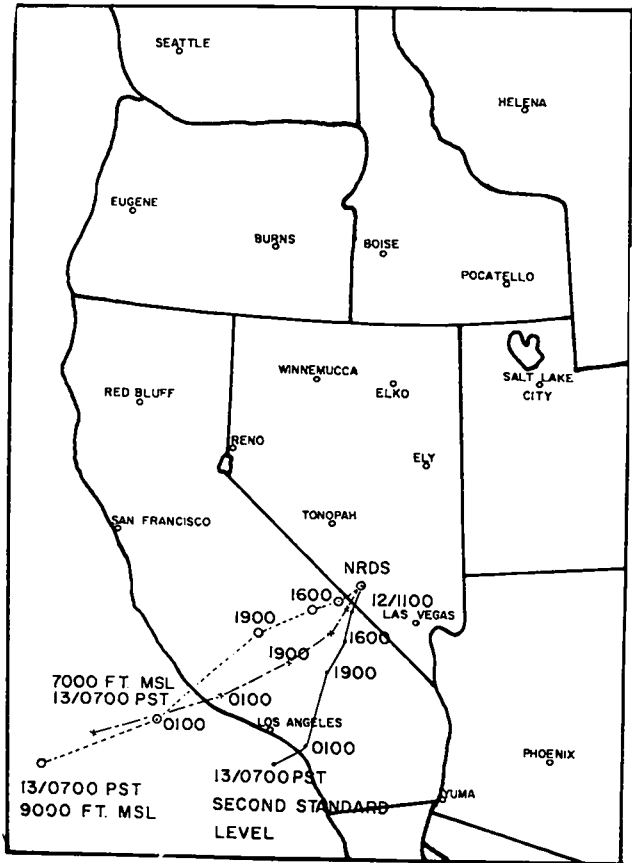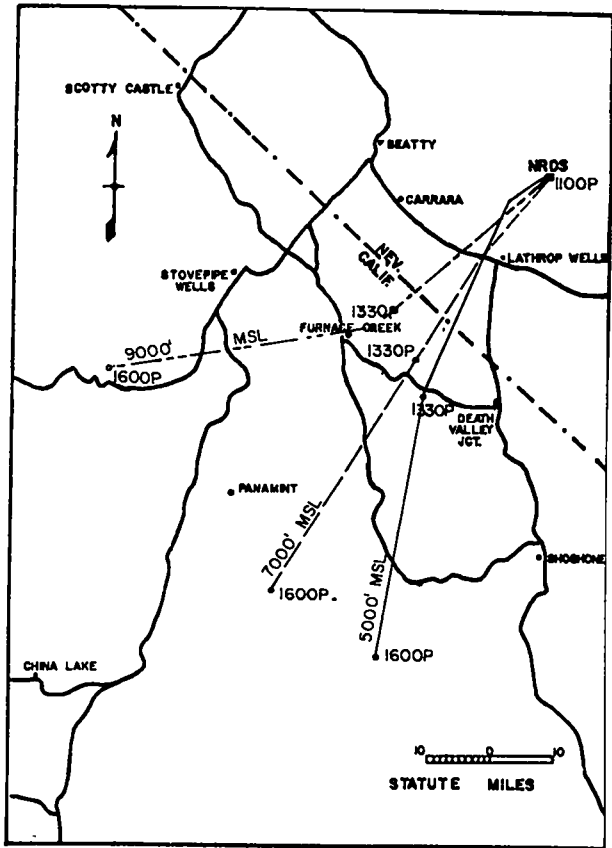
Fig. 5. Air trajectories, January 12, 1965.
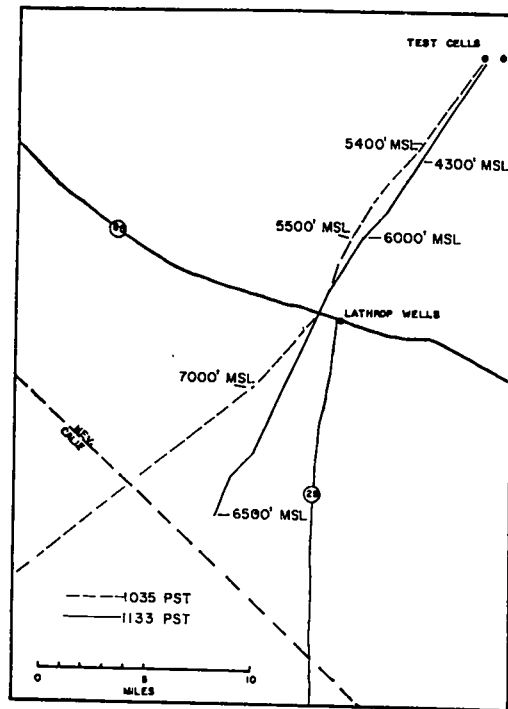
Fig. 6. Tetroon tracks.

TABLE I. UPPER-AIR DATA

Jackass Flats, 1118 PST, 1/12/65

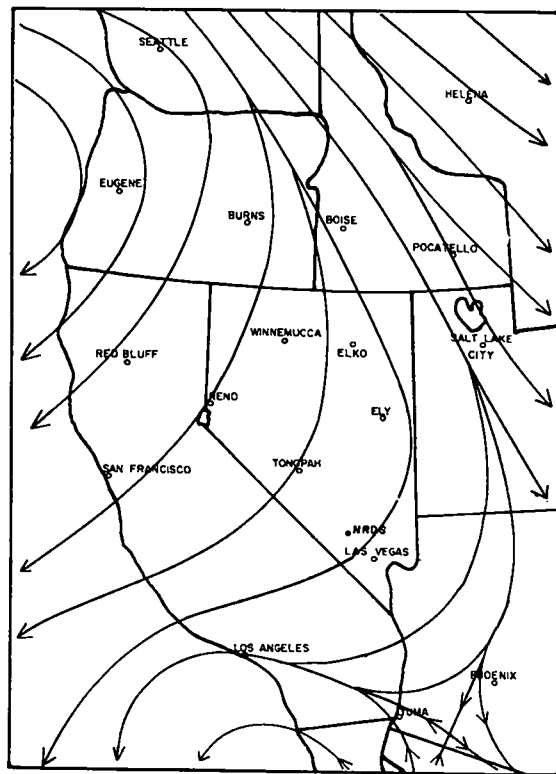| Height (Ft. MSL)	Wind (Deg/Kt)	Pressure (mg)	Temperature (°C)	Dew Point (°C)	Relative Humidity (%)
SFC 3615	020/18	893	12.7	0.0	42
4000	020/19	880	11.0	-1.1	43
4800	030/22	855	7.4	-3.8	45
5000	030/22	850	7.0	-3.5	47
6000	020/18	818	4.1	-4.4	54
7000	020/17	788	1.5	-5.2	61
8000	030/16	759	-1.4	-6.6	68
8630	040/15	740	-3.2	-7.5	72
9000	040/14	730	-3.6	-8.2	70
10000	030/15	704	-5.0	-11.0	63
10085	030/16	700	-5.1	-11.3	62
11000	030/17	676	-6.4	-13.7	56
12000	050/19	648	-7.9	-17.0	48
12650	050/23	632	-8.8	-18.9	44
13000	060/24	624	-9.5	-21.2	38
13780	060/26	606	-11.0	-27.2	25
14000	060/26	600	-11.7	MB	(16)
15000	060/27	576	-14.1	MB	(16)
16000	060/26	553	-16.6	MB	(17)
17000	050/26	531	-19.2	MB	(17)
18000	050/23	511	-21.7	MB	(18)

Amargosa Farm Road, 1200 PST, 1/12/65

Height (Ft. MSL)	Wind (Deg/Kt)	Pressure (mg)	Temperature (°C)	Dew Point (°C)	Relative Humidity (%)
2600	330/20	929	16.0	2.8	41
2830	330/19	919	14.1	0.0	38
3000	330/19	916	13.8	0.2	38
4000	340/17	883	10.5	-1.6	43
5000	350/17	851	7.1	-2.6	50
5030	350/16	850	6.9	-2.6	51
5390	350/15	837	5.6	-3.2	53
6000	360/12	820	4.1	-3.6	57
7000	030/10	789	1.8	-4.5	63
8000	050/12	759	-0.7	-5.7	69
9000	050/17	731	-3.0	-7.3	72
9200	050/17	725	-3.6	-7.5	74
10000	040/21	704	-3.8	-9.3	66
10100	040/21	702	-3.8	-9.6	64
10150	040/21	700	-3.9	-10.0	63
11000	050/23	679	-4.9	-14.0	49
12000	060/25	652	-6.1	-20.5	31
12200	060/26	646	-6.5	-22.4	27
13000	066/28	626	-8.3	MB	(15)
14000	060/29	602	-10.6	MB	(16)
15000	060/27	578	-12.7	MB	(16)
16000	060/27	556	-15.3	MB	(16)
17000	060/27	534	-17.8	MB	(17)

TABLE II. WINDS-ALOFT DATA

Jackass Flats, 1/12/65 (Radar Measurements)

Time of Observation

Height (Ft. MSL)	0800	0815	0830	0845	0900	0915	0930	1010	1030	1045	1100	1130	1145	1200	1230
Surface	350/10	015/09	020/04	020/05	010/09	020/16	030/18	030/22	030/20	030/18	030/17	035/20	030/19	045/17	045/16
4000	010/10	030/15	050/10	030/09	020/15	030/21	040/18	035/22	030/20	040/25	030/20	050/17	030/16	040/20	040/13
5000	010/09	050/18	040/18	030/19	030/19	030/22	040/26	035/21	035/21	050/20	040/21	030/18	040/18	030/14	040/20
6000	050/20	060/24	050/21	040/26	050/23	050/22	060/20	047/16	050/21	050/17	050/23	020/15	040/19	020/19	040/18
7000	050/23	040/20	060/24	060/23	060/10	070/19	060/18	062/21	060/16	050/21	040/13	040/15	050/14	030/19	040/17
8000	040/23	030/17	050/21	050/17	060/21	060/20	050/15	067/17	054/16	030/15	030/15	040/14	050/14	050/11	050/17
9000	040/18	020/18	040/17	040/16	050/21	040/22	030/18	040/15	031/17	020/15	040/19	040/13	050/15	050/13	050/18
10000	030/22	020/18	030/18	040/16	040/21	030/20	030/19	025/16	029/21	020/18	—	040/18	040/17	—	050/20

Lathrop Wells, 1/12/65

Time of Observation and Type of Measurement

Height (ft, MSL)	0800 Radar	0830 Radar	0900 Radar	0930 Radar	1000 Radar	1030 Radar	1100 Pibal	1115 Pibal	1200 Pibal	1230 Pibal	1300 Pibal	1400 Radar
Surface	356/06	360/02	005/06	Calm	Calm	008/05	320/15	344/15	063/10	040/12	046/12	040/10
3000	010/12	003/09	018/08	020/12	004/08	010/05		010/11	050/12	040/11	050/11	050/14
4000	010/14	014/10	026/12	030/13	021/11	010/08		020/12	040/12	030/10	060/10	050/13
5000	030/18	038/15	039/18	040/19	034/15	030/11		030/12	030/12	020/09	050/08	040/10
6000	050/23	046/21	045/23	050/22	041/19	050/12		030/14	040/14	010/08	030/09	030/10
7000	050/19	058/20	058/21	060/23	050/21	050/14		050/15	040/13	010/09	020/12	030/17
8000	060/20	056/18	056/20	060/22	050/19	050/17		050/18	050/12	010/10	030/14	060/18
9000	060/20	048/20	052/18	050/18	056/15	030/20		040/23	050/15	—	050/16	070/17
10000	040/19	038/18	042/21	050/20	—	040/20		040/21	050/19	—	070/17	070/19
11000	030/17	026/22	037/19	050/18	—	040/19		050/16	060/24	—	080/19	080/16
12000	040/21	042/20	046/21	050/19	—	060/20		040/17	060/26	—	070/23	070/21
13000	050/21	048/21	048/22	050/23	—	060/22		020/19	060/29	—	060/28	070/27
14000	050/22	047/22	058/19	060/22	—	060/21		040/22	060/27	—	060/30	060/30
15000	050/25	055/23	057/24	—	—	060/19		—	060/25	—	060/33	070/31

TABLE II. CONTINUED

Amargosa Farm Road, 1/12/65 (Pibal Measurements)

Time of Observation

Height (ft, MSL)	0800	0830	0900	0930	1000	1030	1100	1200	1300	1330	1400
Surface	345/08	330/10	320/16	320/15	310/18	320/10	305/13	330/20	030/08	330/08	325/08
3000	350/09	330/10	330/16	320/15	320/18	320/10	310/13	330/19	030/08	330/15	330/08
4000	350/14	330/13	350/18	340/16	330/19	340/11	330/16	340/17	010/05	340/14	340/06
5000	020/14	010/10	010/15	010/11	350/12	340/13	340/13	350/17	030/05	360/10	350/07
6000	040/12	040/11	020/12	050/10	030/10	010/13	350/11	360/12	050/09	030/08	350/07
7000	060/14	070/13	040/12	060/14	060/17	040/17	030/13	030/12	040/16	050/10	360/06
8000	060/17	060/14	060/14	060/13	070/15	040/17	040/19	050/12	040/17	050/13	070/10
9000	060/20	040/15	050/14	050/14	050/12	040/12	030/15	050/17	040/16	050/21	070/20
10000	050/19	040/16	040/16	040/16	040/12	040/13	030/16	040/21	060/20	060/23	060/23
11000	040/20	040/18	030/19	040/20	040/14	030/15	040/17	050/23	070/22	070/22	060/23
12000	040/19	040/20	040/21	040/24	—	040/22	050/21	060/25	060/22	060/23	070/24
13000	050/21	040/20	050/22	050/26	—	050/24	060/25	060/28	060/23	060/25	060/25
14000	060/26	040/20	050/23	050/25	—	060/30	050/28	060/29	060/25	060/26	060/26
15000	060/26	030/19	040/21	050/23	—	050/31	050/26	060/27	050/28	060/25	060/24
16000	—	—	—	—	—	—	—	060/27	—	—	—
17000	—	—	—	—	—	—	—	060/27	—	—	—

TABLE II. CONTINUED

Death Valley Junction, 1/12/65 (Pibal Measurements)

Height (ft, MSL)	0800	0900	1000	1100	1200	1300	1400	1500
Surface	340/15	345/18	340/20	340/20	345/18	340/15	340/18	—
3000	350/29	360/25	360/25	350/25	360/28	350/20	340/18	—
4000	360/27	010/27	010/25	010/27	010/29	360/20	350/18	—
5000	020/23	020/26	030/24	020/27	030/21	020/18	010/19	—
6000	030/23	040/23	050/24	040/23	050/19	020/22	020/21	—
7000	040/22	050/20	050/21	050/19	060/14	030/24	030/21	—
8000	050/22	060/18	050/20	060/16	070/09	040/19	040/17	—
9000	050/20	050/17	050/17	070/16	090/07	060/12	060/14	—
10000	060/19	050/17	040/16	060/14	090/07	080/09	090/12	—
11000	050/21	050/16	050/18	060/12	070/10	090/08	090/13	—
12000	040/21	050/14	050/20	050/15	070/14	070/11	080/17	—
13000	040/18	040/14	050/20	050/18	060/21	060/20	070/24	—
14000	040/15	040/14	060/20	050/23	—	060/28	060/30	—
15000	030/15	040/13	060/16	050/27	—	060/30	060/31	—

Furnace Creek, 1/12/65 (Pibal Measurements)

Height (ft, MSL)	0800	0900	1000	1100	1200	1300	1400	1500
Surface	166/03	170/05	210/10	114/10	271/04	218/06	348/20	320/22
Sea Level	100/05	360/05	025/10	020/10	030/07	030/08	340/21	330/21
1000	350/10	010/06	035/12	340/10	350/11	340/17	330/21	340/20
2000	350/14	350/11	360/15	340/12	360/12	340/19	330/19	350/22
3000	360/17	350/12	360/13	340/10	350/13	350/19	330/18	350/22
4000	010/17	360/12	360/11	350/11	360/15	360/19	350/15	360/18
5000	030/13	030/13	360/10	010/15	010/17	020/19	360/12	360/18
6000	030/12	050/16	020/12	020/20	020/17	030/13	010/05	010/17
7000	050/14	050/17	030/16	030/17	040/15	040/09	020/18	030/16
8000	050/16	040/18	040/18	040/15	050/12	070/09	050/19	060/16
9000	050/18	030/19	040/18	050/14	050/12	070/12	050/21	080/17
10000	050/19	050/20	050/18	040/14	050/14	030/15	060/19	080/15
11000	050/19	060/21	060/18	050/16	060/18	060/21	070/18	070/17
12000	050/20	060/21	060/18	060/18	060/22	070/24	070/20	070/24
13000	060/20	060/20	060/19	060/22	060/25	070/24	070/23	070/27
14000	050/21	060/17	060/19	060/25	060/24	070/25	070/26	070/27
15000	050/23	060/14	060/19	060/26	060/24	070/26	070/26	070/27

IV. THE REACTOR ERUPTION

The material in this chapter is largely from LA-3351, "Kiwi-TNT Explosion," by Reider.[11]

The Kiwi-TNT reactor was "exploded" in the sense that it was a violent disruption and dispersion of an originally intact object. It blew up in an unusual fashion resembling neither a typical nuclear detonation nor most types of chemical explosions. To give a better understanding of the eruption, its characteristics will be compared to those of more common explosions.

The deflagration accompanying the Kiwi-TNT excursion was the result of rapid vaporization of part of the carbon-uranium-carbide core. The pressure vs. time relationships in the Kiwi-TNT event were unusual, but not unique. They are most nearly approximated by the explosion of black powder, one of the few explosive materials that acts by exothermic chemical reaction of physically mixed reactants rather than by exothermic decomposition of a chemical compound. The Kiwi-TNT energy release was physical in origin rather than chemical, however. The vaporization occurred too fast for the resultant gas to escape through the reactor interstices, pressure quickly built up in the core until it exceeded the yield strength of the pressure vessel (a few thousand psi), and the vessel burst with explosive violence. The time required for this peak pressure to occur is estimated to be about 1 msec. In contrast, the production of gas required to release an equivalent energy during detonation of high explosives such as trinitrotoluene or nitroglycerin is much more rapid, requiring perhaps a twentieth of the time needed to vaporize a part of the Kiwi-TNT core. On the other hand, deflagrations of gas-air mixtures at atmospheric pressure and explosions involving organic dusts are much less violent than the Kiwi-TNT event, demonstrating pressure rises of only a few psi/msec.

From the nature of recovered reactor fragments, one can conclude that the Kiwi-TNT event resembled a deflagrating explosive such as black powder, rather than a detonating or brisant one, such as trinitrotoluene, or a slower reaction such as occurs during explosions of gas-air mixtures. The Kiwi-TNT excursion produced a shower of incandescent sparks rarely seen in anything but a pyrotechnic display. Fragments of various sizes and weights were thrown as far as 2,000 ft, with a distribution similar to that from chemical high explosives. However, unlike missiles from chemical high explosives, which experience an almost instantaneous pressure rise from the detonation

wave, these fragments did not show extensive shredding and stretching. Missiles from dust or atmospheric gas-air mixture explosions would have been larger, with less shredding and stretching than those of the Kiwi-TNT test, and they would not have traveled so far. Boiler explosions usually produce only a few large missiles from components coming apart at their seams. Explosions of combustible gas mixed with oxidant at high pressures, such as high-pressure oxygen contaminated with hydrocarbons, would have missile patterns more nearly like those of Kiwi-TNT.

The thermal release and the extremely high temperatures occurring during the excursion are results associated almost exclusively with nuclear reactions. The charring of wooden poles as far away as 70 ft and the brilliant mass of hot, burning graphite are phenomena not usually seen in explosions. Brightness is a function of temperature and emissivity, and carbon at or above its vaporization temperature of 3,900° K is an efficient emitter, in contrast to other explosive products. High explosives detonate rapidly, but they are poor heat sources and essentially undergo exothermic decomposition without producing high temperatures; they usually go from the solid or liquid to the gaseous phase without much burning and usually without scorching nearby objects. Dust explosions do not have a very high energy density and are not very bright. Gas explosions do not scorch things very much even if the mixture is fuel-rich.

Overpressures and blast effects associated with the Kiwi-TNT event must be compared to those of high-explosive detonations, even though the phenomena differ in many respects, because high-explosive effects are the only ones which have been adequately quantitated for comparison. Two blast gauges 100 ft from the Kiwi-TNT event gave readings of 3 and 5 psi. The lower reading could have come from a surface burst of a 125-lb hemispherical charge of trinitrotoluene, and the higher reading from a 300-lb charge of similar shape. Corrugated metal buildings 600 to 700 ft away, designed to withstand 100-mph winds, showed no sign of damage. None would be expected following the explosion of about 100 lb of trinitrotoluene, but a 300-lb charge might have affected them. The walls of several office trailers 800 to 1,000 ft from the test point had deflected, throwing many wall fixtures to the floor but no permanent deformation was evident. A few, but not all, of the windows, even in the facing walls of the closest trailer, were broken.

These effects are consistent with those of an explosion of approximately 100 lb of trinitrotoluene. An examination of the test point after the experiment showed evidence not typical of a high-explosives accident. Although it was not completely inconsistent with the explosion of about 100 lb of trinitrotoluene, it was certainly inconsistent with one involving significantly more, say 300 to 500 lb. In the latter case, one would expect more sweeping away of the debris beneath the explosion, and possibly even cratering, which did not occur. Therefore, it can be concluded that the Kiwi-TNT blast was roughly equivalent to that from the detonation of 100 to 150 lb of trinitrotoluene.

From the effects discussed above, an estimate of the possible nonradiation hazards to anyone in the vicinity of the excursion is as follows: everyone within 100 ft of a Kiwi-TNT deflagration would be seriously or fatally injured by blast, thermal burns, missiles, physical displacement, or any combination thereof. Thermal burns would probably be the most significant cause of injury.

Overpressure from the blast would not be seriously injurious to a person beyond 50 ft unless it physically displaced him. Between 100 and 250 ft there would be a significant number of bodily injuries, possibly to 1 in 4 persons, but few injuries would be serious or fatal. Probably no more than first-degree burns would occur. Blast damage would be minimal. The most common injuries would be from missiles and physical displacement. At 250 ft the probability of being struck by a small core fragment would be about 1 in 8, but the probability of injury would be less than 1 in 100. No harm would result from blast. Thermal burns would be minimal. The peak overpressure might knock a person over but would not accelerate him enough to do appreciable harm. Beyond 500 ft there would be a chance of no more than 1 in 1,000 of being injured by a missile, although the probability of being struck by a small fragment would be about 1 in 100. No danger would exist from blast or heat. As discussed later, these effects are all overshadowed by the radiation hazards.

V. THE RECOVERED DEBRIS

Much of the material in this chapter is from LA-3337-MS, "Kiwi-TNT Particle Study", compiled by Campbell,[8] and LA-3445-MS, "Kiwi Transient Nuclear Test Fuel Element and Support Element Fragment Study", by Fultyn and Boasso.[9]

One of the secondary objectives of the Kiwi-TNT test was to quantitatively determine the character of the resulting debris. This aspect of the test included various experiments designed to obtain information concerning the size distribution, nature of the radioactivity, and other physical characteristics of the debris. The development of techniques to study the nature of the radioactivity of the smaller debris particles and the findings of the study are fully described in the above reports. This chapter sketches the experimental plans, reports the unclassified results, and relates some conclusions.

In this discussion debris is classified into two categories: particles and fragments. Particles are pieces of the reactor or neighboring material small enough for their trajectories to be influenced by wind and atmospheric eddies. Fragments are larger pieces, ranging upward from a few millimeters long, whose trajectories may be approximately described by ballistic equations.

Since numerous techniques of particle technology were to be compared, a variety of approaches was taken for deployment of particle-collecting devices. Numerous sampling stations were placed at carefully surveyed locations around the test point. These are shown in Fig. 7.

The simplest device was sheets of polyethylene, about 6 ft wide, laid on the ground in continuous strips. Five of these strips were laid in the anticipated upwind and downwind directions. It was hoped that debris falling on the sheets could be photographed to obtain information about its dispersion. These hopes were not realized because strong winds several days before and after the test made it difficult to keep the sheets clean and in place. No debris was seen on the sheets except along the edges where the wind had winnowed some of it. In addition, the plastic became tattered out to beyond 200 ft as hot debris falling on the plastic burned many holes through it. Some useful samples of larger particles and fragments were collected from the winnowings and by searching under the burn holes.

Two types of gummed-tray collectors used to obtain samples for visual and microscopic analysis were called the macrocollection tray and microcollection tray, respectively.
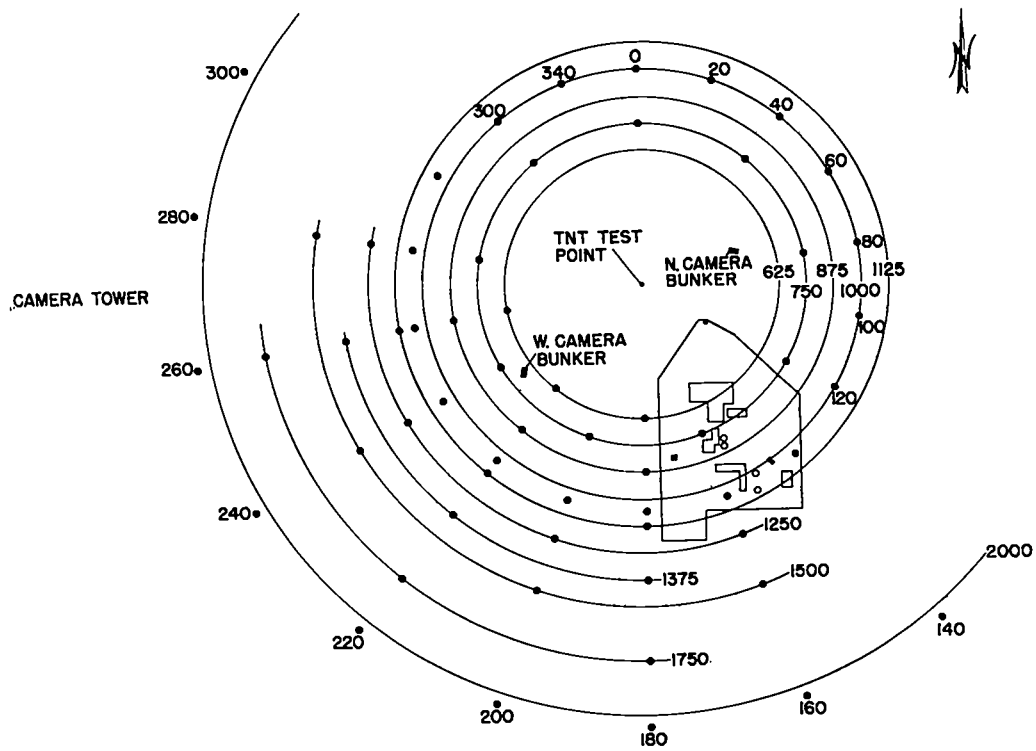
a. Close range.
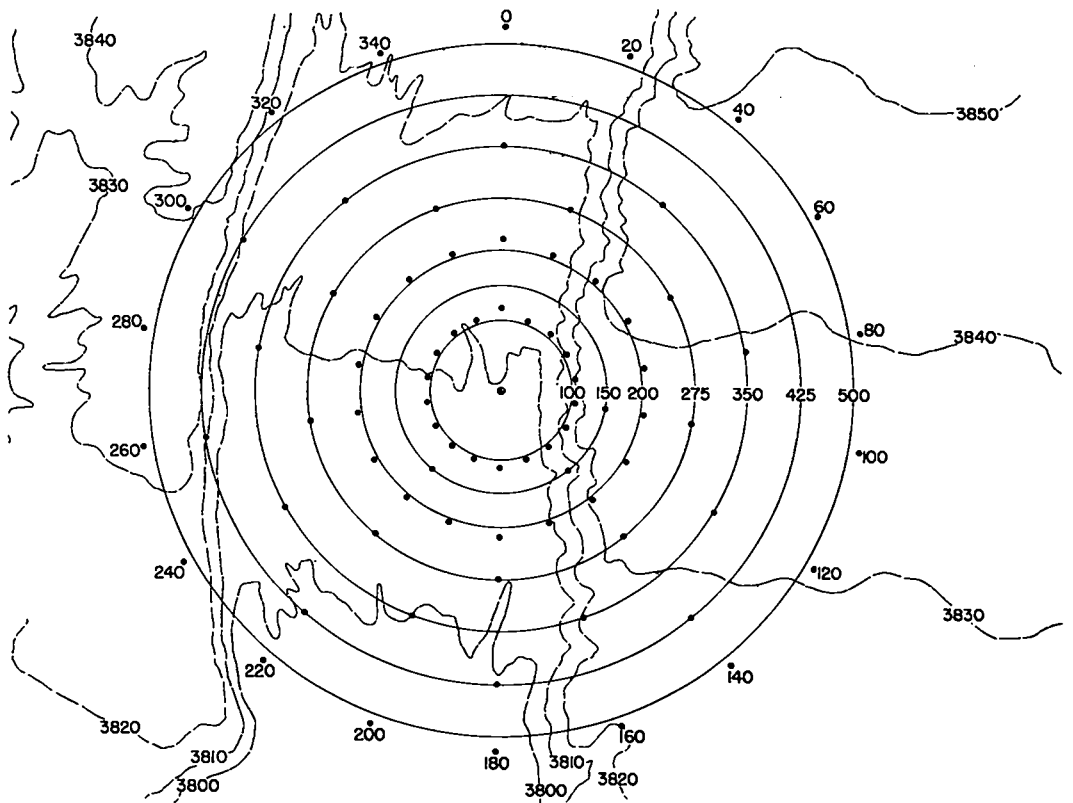
b. Long range.

Fig. 7.   Debris collection stations.

The macrocollection tray or "macrotray" (Fig. 8a) consisted of two open aluminum frames between two 14 × 17-in. hardboard covers. Mylar sheets, 0.003 in. thick, were stretched over facing sides of the aluminum frames. When placed on their special stands in the field, the macrotray "books" lay open with the Mylar sheets facing up. Under one "page" was a 14 × 17-in. sheet packet of type M x-ray film covered with a sheet of aluminum foil, under the other was a 4 × 5-in. sheet packet of ASA 3000 Type 57 Polaroid film. The books were clipped to stands to prevent them from blowing away. The macrotrays were opened in the field a few hours before the test and the Mylar surfaces were sprayed with Dow Corning silicone antifoam to promote adhesion of particles falling on them. When recovered within a few hours after the test, the x-ray films were removed and the macrotray books were closed and clipped shut for transport back to the laboratory where the films were developed. Fresh x-ray films were placed in the books to obtain autoradiographs of the debris on the Mylar, to collect data concerning the activity of the particles, and to assist in locating them during subsequent visual and microscopic analysis.

The microcollection tray or "microtray" (Fig. 8b) consisted of six 1 × 3-in. standard glass microscope slides coated with nonhardening alkyd resin side by side in a plastic holder. The holders were opened a few hours before the test and covered and collected a few hours after. Autoradiographs were made of the slides and the slides were examined microscopically.

Although not originally intended for inclusion in this particular study, the resin-coated trays used to measure radioactivity deposited from the effluent cloud at great distances from the test point were also subjected to some of the techniques used on the other sampling devices. This was done after they had served their purposes in the effluent studies.

To collect debris samples large enough for sieve analysis, 100 hopper-type collectors were placed around the test point. The hopper collector (Fig. 8c), was a square, inverted, pyramidal funnel of sheet metal. The open top measured 4 × 4 ft. A 1-gallon paint can was held in a slide under the funnel against spring tension by a pin. Several hours after the test, the pin was automatically removed by a string attached to the windup key of an alarm clock. The spring then pulled the can from under the funnel to a closed section of the slide until the samples could be recovered. A few hours before the test, the cans

were placed under the funnel openings and the alarm clocks were wound and set for late afternoon. Two days after the test the cans were removed, tightly covered with standard paint can lids, and brought back to the laboratory where the contents were completely transferred to smaller plastic jars. In spite of the closure device employed, the samples contained much material other than reactor debris, contrary to prior hopes. Also, the explosive shock of the test actuated some of the retaining pins at the moment of deflagration, causing the collecting cans to withdraw from under the funnels before much debris reached them.

As an afterthought, eight wet collectors were also placed in the field. These were 16 × 20-in. photographic developing trays containing a few liters of distilled water and weighted by plastic-covered lead bricks to prevent their being blown away. During analysis of the reactor debris, it was concluded that these devices yielded some of the best samples collected.

The collection of material to document the size distribution and geographic locations of the larger reactor fragments was undertaken concurrently with efforts to decontaminate the test site. The test area was divided into sectors bounded by stakes marking the positions of other sampling devices (Fig. 9). Each sector was systematically scanned by radiation detection survey teams holding the probes of survey instruments a few inches above the ground. Any area that produced a meter reading above background was carefully searched; if a reactor fragment was found it was picked up with tongs and placed in a container. The smallest fragments readily found by this method were approximately ¼ in. long. The containers for each
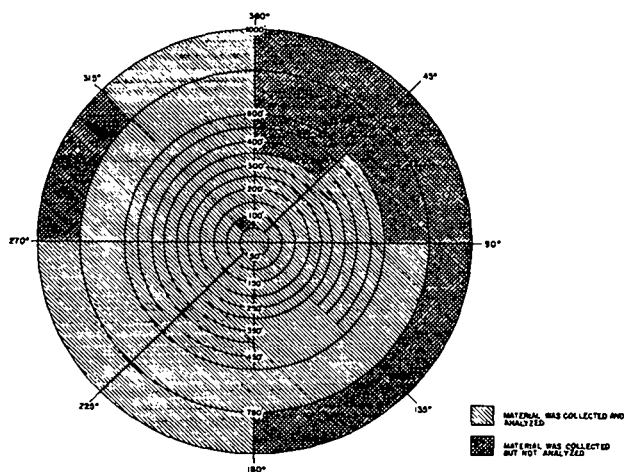

Fig. 9. Fragment collection sectors.

a. Macrotray.

ALUMINUM FRAME 0.125" THICK

17.375"

14.625"

TEMPERED MASONITE 0.125" THICK

17.00"

20.00"

MYLAR 0.005" THICK

ALUMINUM FOIL 0.025" THICK

TYPE 57 POLAROID FILM WRAPPED IN ALUMINUM FOIL 0.025" THICK

CLOTH TAPE

14.00" x 17.00" X-RAY FILM HOLDER

b. Microtray.

c. Hopper.

CLOCK TRIP MECHANISM

SPRING

TRACK

PAINT CAN IN TRIPPED POSITION
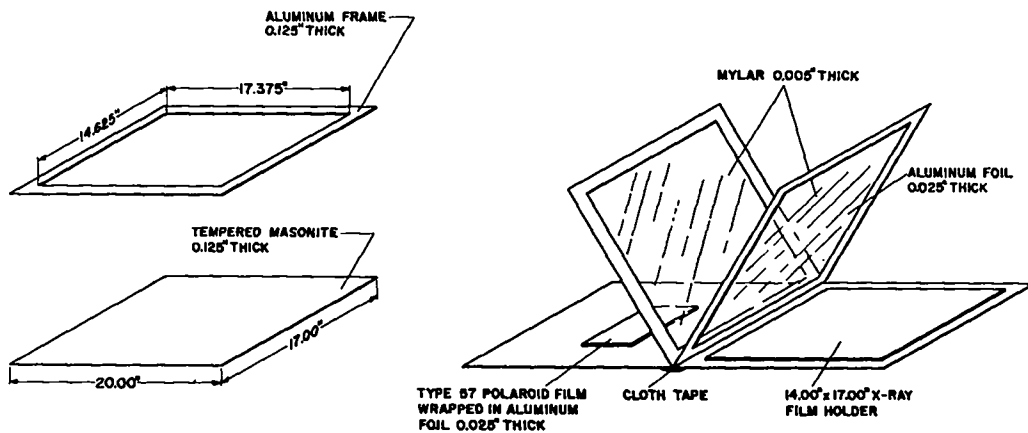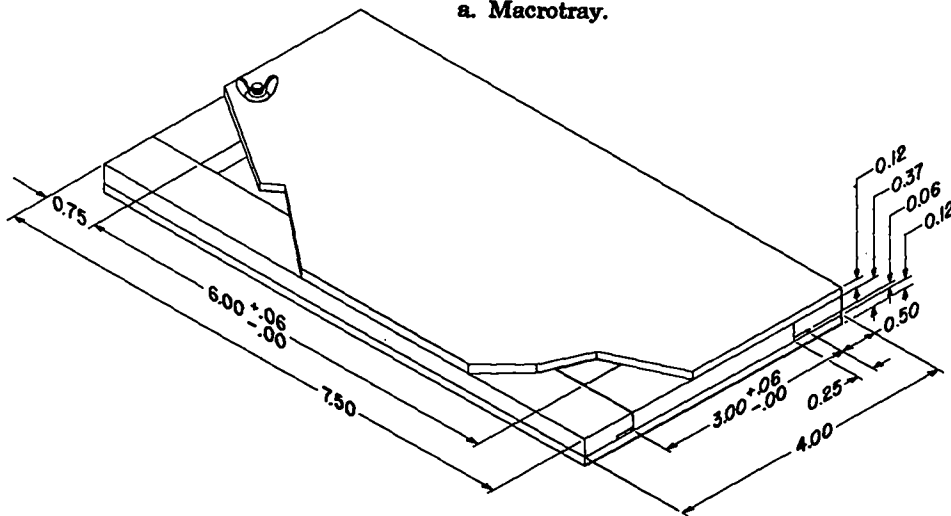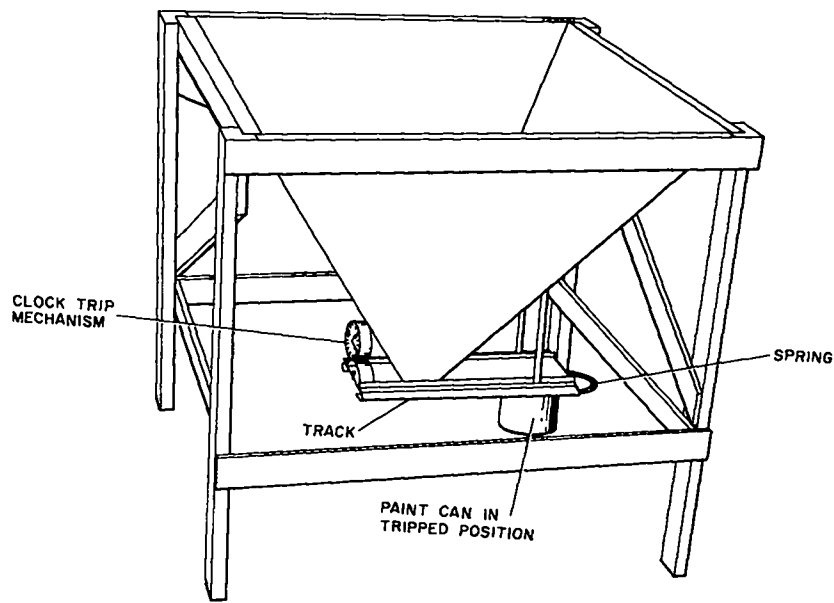
Fig. 8. Particle collection devices.

16
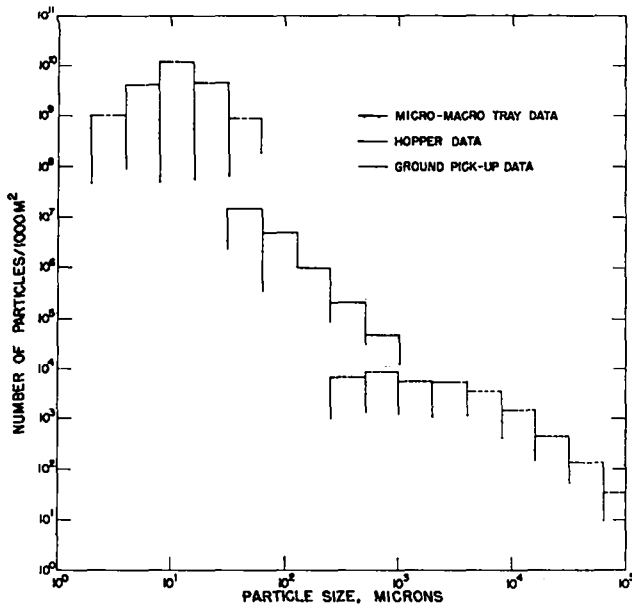
Fig. 10. Particles/1000 m² vs. size class for a typical debris collection station.

Fig. 11. Number of particles in each size class as determined by all sampling methods over entire sampling area.

area segment were marked by location. Unfortunately, the samples from some of the first segments were accidentally combined, resulting in loss of detail. The fragments from each sector were separated according to size and reactor component type: loaded fuel elements containing fissionable material, unloaded core support elements, and other reactor components. Only fragments in the first two of these categories were further classified by size using remote handling equipment in the hot cells* of the Reactor Assembly and Disassembly building at the Nevada Test Site, and at the Chemical and Metallurgical Laboratory at Los Alamos.

Figure 10 shows the number of particles/1000 m² vs. size class for a typical station representing a composite of data obtained from all sampling methods employed. The graph shows deviations from a linear relationship between number of particles vs. particle size on a log-log presentation. The data for approximately half of the sampling stations would have plotted as nearly straight lines in such graphs, while the data from the remaining stations exhibited deviations typified by Fig. 10. Figure 11 is a histogram of the total number of particles in each size classification deposited over the total area covered by the debris sampling array as determined by all particle sampling methods. For the construction of this graph, the test area was divided into sectors, with a sampling station located at the center of each sector. It was assumed that the number of particles per unit area in each size class remained constant over the sampling sector. Figure 12 presents

the same data as those in Fig. 11, but shows the percent of total number of particles less than a given size deposited over the sampling array. Figure 13 is another presentation of these same data as percent of mass of total debris less than a given size deposited over the sampling array, the conversion using representative size and density data. The data in Figs. 10 to 13 represent, insofar as possible, only particles definitely identified as reactor debris. However, for some size classifications it was impossible to separate reactor particles from desert dust that had adsorbed radioactivity. Such particles were included as reactor debris.

Fig. 12. Percent of total number of particles less than stated size.

17

Fig. 13. Percent of mass of particles less than stated size.

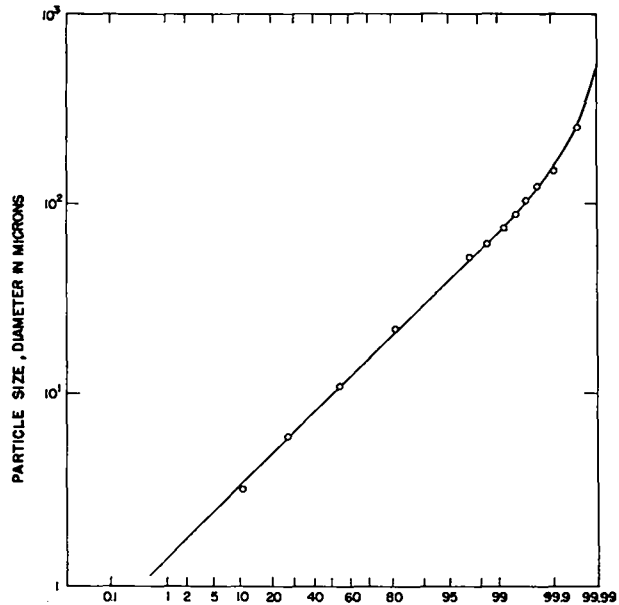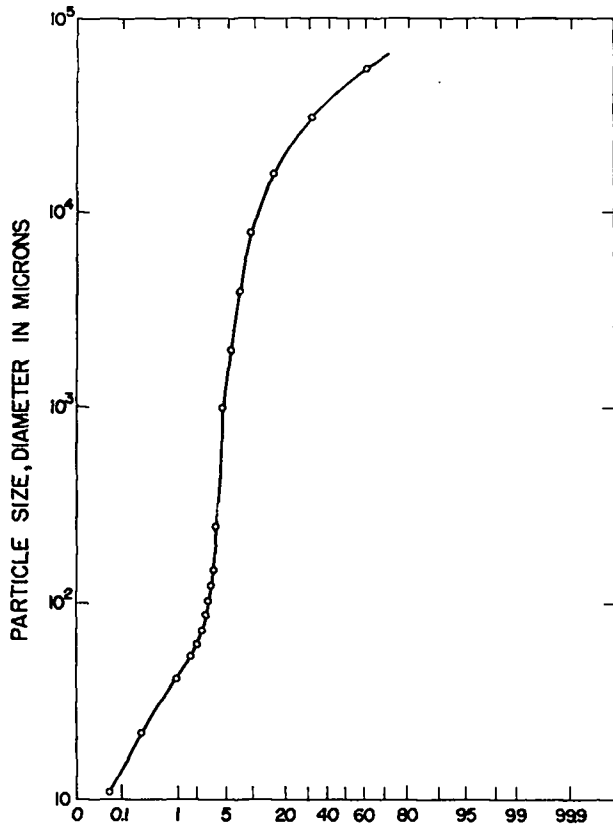Fig. 14. Curies of uranium per particle vs. particle size.
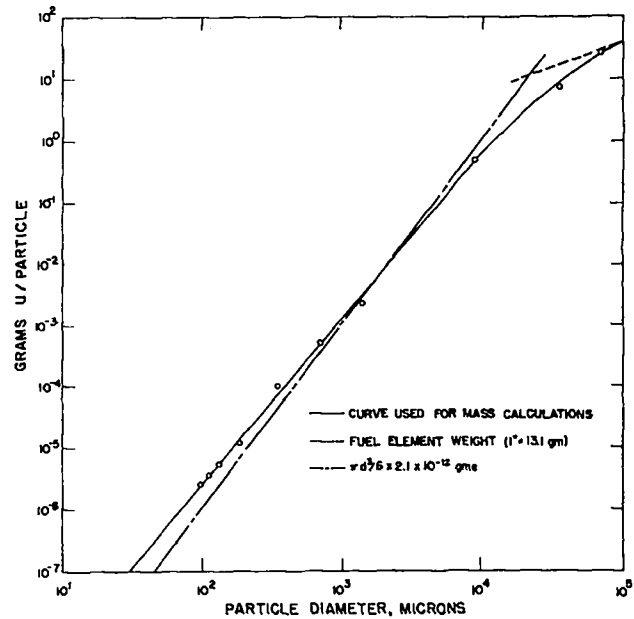
Fig. 15. Weight of uranium per particle vs. particle size.

Figures 14 to 17 illustrate the distribution of uranium in the particles in one sampling sector. These data are confined to graphitic particles less than 5 mm in diameter. The difficulty of performing this type of analysis precluded its use for all samples. The concentration of uranium in particles approximately 100 μ in diameter can be attributed to a detail of reactor design discussed later.

Figure 18 shows the gamma activity per particle vs. particle diameter for a typical sampling sector. Particle activity is directly proportional to the square of the particle diameter, or to the surface area. This strongly suggests that the activity was deposited on the surface of the particles rather than being distributed throughout the particle volume. This behavior was found in all samples so analyzed, and was assumed to apply to all those collected.

The size distribution of the fragments collected during ground pickup is shown in Fig. 19 which gives the fraction less than a given size by count for loaded fuel element fragments, unloaded support element fragments, and the sum of all core elements, respectively. Figure 20 presents the geographic distribution of fragment density (fragments/ft²) around the test point and

shows that the center of fragment distribution was translated downwind.

To interpret these data, one should understand some details of construction of the reactor core. In the simplest terms, the core is composed of bundles of graphite elements loaded with fissionable material and support elments containing no fissionable material. The fissionable material is not mixed homogeneously with the graphite of the

18
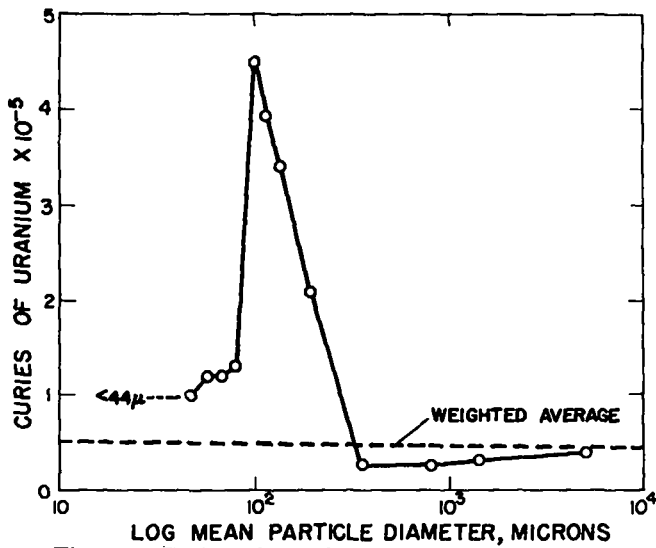
Fig. 16. Curies of uranium per gram of material vs. particle size.
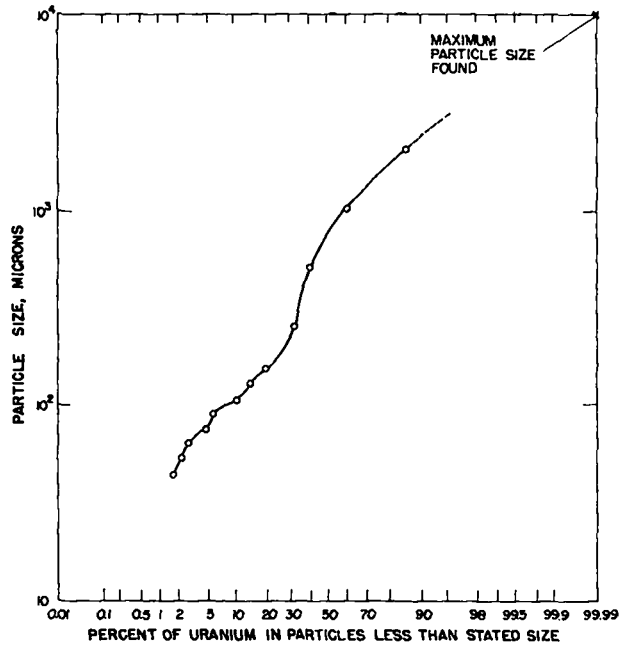
Fig. 17. Weight fraction of recovered uranium contained in particles less than stated size.

Fig. 18. Gamma activity per particle vs. particle size.

fuel elements, but is contained in small, evenly dispersed beads. Thus, fission energy is not produced uniformly throughout the core, but occurs at numerous small discontinuous points and is absent from the support elements.

During normal reactor operation, fission occurs slowly enough to allow the resulting thermal energy to be transferred from the uranium beads through the surrounding graphite to the coolant flowing through the core, so that temperatures high enough to cause mechanical failure of the core materials do not occur.
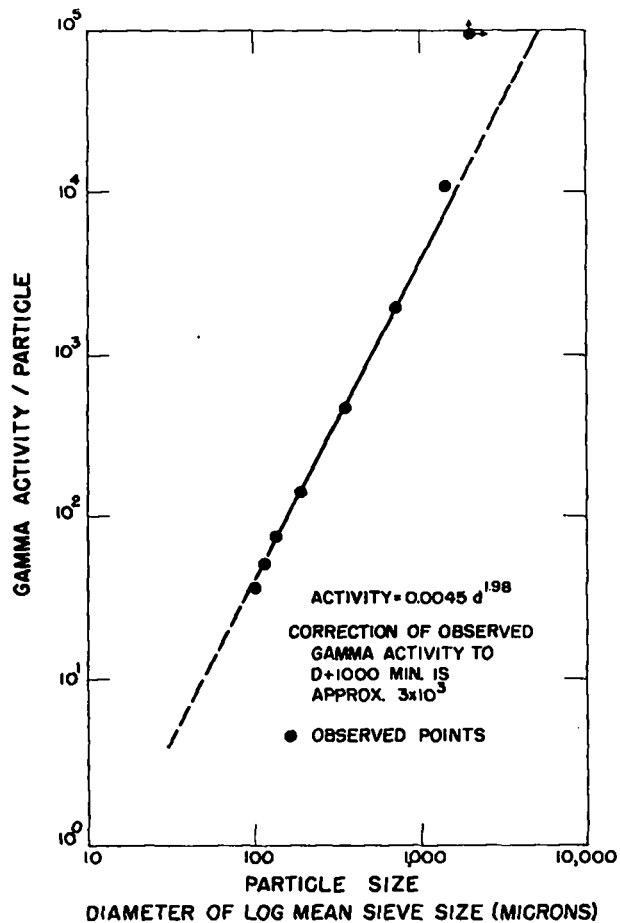
During the Kiwi-TNT excursion, however, the fission rate was deliberately increased so that the resulting heat could not be transferred fast enough to avoid vaporizing significant amounts of the beads and their surrounding graphite. The pressures resulting from this vaporization caused destruction of the reactor. Other experiments have shown that there is a critical fission density rate below which vaporization does not occur, since heat transfer is adequate to prevent it. It is also known that fission density rate is not uniform throughout the reactor core, but is highest at the center and diminishes towards the ends. Furthermore, neutronics calculations showed that some regions of the Kiwi-TNT core experienced fission density rates above, and others below, the critical values.

Thus, it may be hypothesized that, as reactivity was rapidly inserted into the reactor, the fission density rate at the center of the core exceeded the critical value and vapor began to form in and around the fuel beads. The vapor formed too fast to escape through core interstices,

19

SIZE IN INCHES
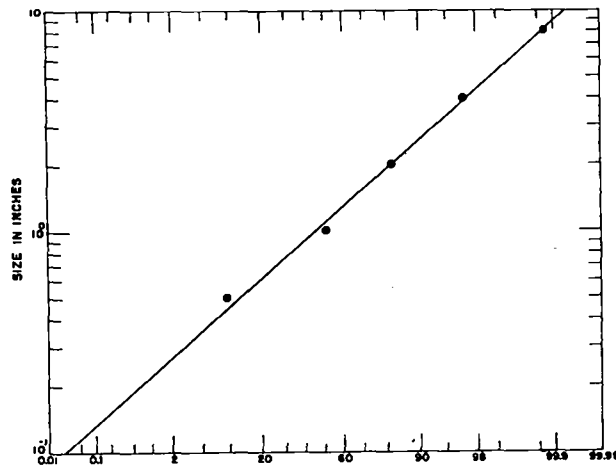
a. Fuel element fragments.

SIZE IN INCHES
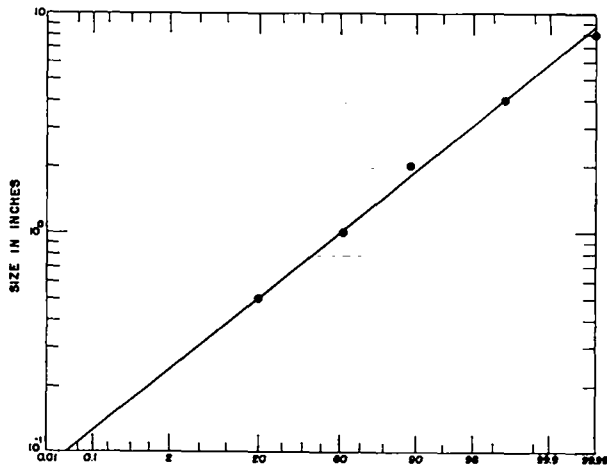
b. Support element fragments.

SIZE IN INCHES
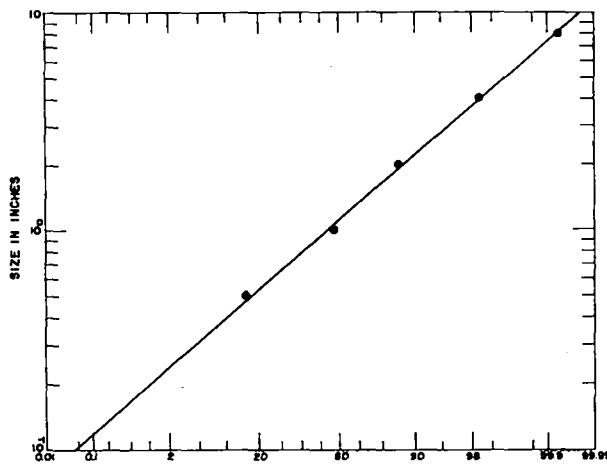
c. Total fragments.

Fig. 19. Percent of recovered fragments less than stated size.

internal pressures quickly rose above the stress limits of the reactor materials, and the reactor was violently disassembled. In those regions where the critical fission density rate was exceeded, sufficient fission energy was released to vaporize 5 to 20%

of the core materials. Where the distances between vapor cells were very small, the fuel element materials that were not vaporized were subjected to very high pressures from all directions and were probably crushed and ground into very small pieces. Other portions of the core such as the support elements did not vaporize, but were surrounded by vaporizing areas and were subjected to a second mechanism of destruction, visualized as crushing and grinding. Still other areas of the core, such as the outer portions, where the fission density rate was below the critical value, were adjacent to vaporized areas and were subjected to destructive forces of a third type, visualized as an unidirectional explosive mechanism. Thus, at least three types of destructive mechanism presumably occurred.

The nuclear excursion was terminated as the reactor became disassociated and the expansion of the incandescent vapor and the inertia of the rapidly moving incandenscent solid pieces produced an explosive spectacle. Since fission products were produced at points most likely to be vaporized, they were probably released to the cloud as vapor rather than as particles. As the cloud cooled, the fission products condensed on graphite or entrained desert dust particles in the cloud, accounting for particle activity as a surface phenomenon. Uranium, on the other hand, could be expected to be found both adsorbed on particles by condensation from vapor and intimately embedded throughout the volume of fragments in the form of unvaporized beads. It does not seem unreasonable that many more-or-less intact beads would be dislodged from the graphite matrix.

The destructive mechanisms just postulated can be supported by the fact that 67% by weight of the support element material in the core was collected, while only 12% of the loaded fuel element material was recovered. Some of the core materials were marked to identify their locations in the reactor, and more parts from the outer sections of the reactor were found than from inner sections. The data presented in Fig. 13 indicate that several destructive mechanisms may have been operable; a typical plot of the percent by weight of a dust sample less than a given size, on log-probability paper, lies on or near a straight line. This is almost always so when the dust was produced by a single mechanical operation, such as blasting, grinding, or crushing, acting on a homogeneous medium. Figure 13 shows several distinct regions where the points lie on a straight line, suggesting that there was probably more than one mechanism of breakage.

CONCENTRATION FOR ANALYZED SECTORS; FRAGMENTS/SQ.FT.

$\geq 2 \times 10^{-1}$ $1 \times 10^{-1} - 5 \times 10^{-2}$ $2 \times 10^{-2} - 1 \times 10^{-2}$ $6 \times 10^{-3} - 1 \times 10^{-3}$

$2 \times 10^{-1} - 1 \times 10^{-1}$ $5 \times 10^{-2} - 2 \times 10^{-2}$ $1 \times 10^{-2} - 6 \times 10^{-3}$
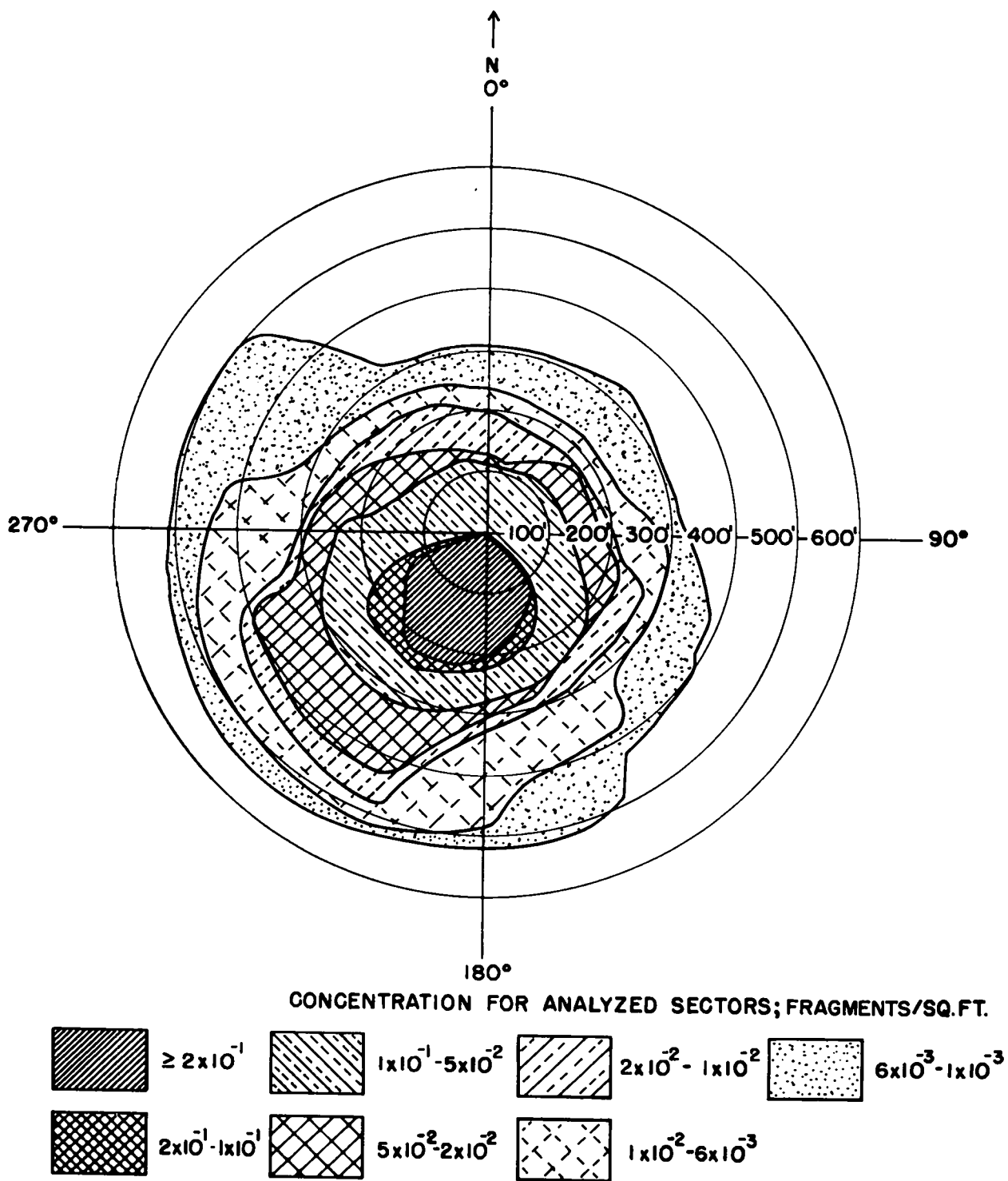
Fig. 20.   Distribution of fragments over recovery area.

VI. PROXIMATE NUCLEAR RADIATION MEASUREMENTS

The material in this chapter is largely from LA-3304, "Integral Gamma and Neutron Measurments on the Kiwi-TNT" by Lee and Worman,[7] and from LA-3446, "Gamma Dose Rate Measurements — Kiwi Transient Nuclear Test", by Sanders.[12]

The devices used by LASL to obtain integral gamma and neutron dosimetric data from the Kiwi-TNT experiment differed little from those used previously in tests of Kiwi and NRX reactors.

Neutron threshold detectors consisted of ^{239}Pu, ^{237}Np, and ^{238}U fission foils supplemented by gold and sulfur activation detectors.[7] The sets of fission foils were encased in cadmium and placed in ^{10}B balls. The neutron threshold energies measured by the boron-surrounded foils are 0.004 MeV for ^{239}Pu, 0.75 MeV for ^{237}Np, and 1.5 MeV for ^{238}U. A ^{32}S(n, p) ^{32}P reaction occurs in the sulfur pellet at neutron energies above 2.5 MeV. Gold is activated by thermal and resonance neutrons. Gold foils encased in cadmium are activated only by neutrons of greater than 0.3-eV energy because of the large absorption cross section of cadmium for neutrons below this energy. Activity differences of paired gold foils, one bare and one cadmium-encased, indicate the thermal neutron flux. The integral neutron flux values (nvt) were converted to neutron doses by factors of

9.3 $\times$ 10^{-10} rad/nvt for neutrons between 0.004 and 0.75 MeV;

2.32 $\times$ 10^{-9} rad/nvt for neutrons between 0.75 and 1.5 MeV;

2.98 $\times$ 10^{-9} rad/nvt for neutrons between 1.5 and 2.5 MeV;

3.63 $\times$ 10^{-9} rad/nvt for neutrons above 2.5 MeV; and

5.50 $\times$ 10^{-11} rad/nvt for thermal neutrons.

A glass gamma-dosimetry system consisting of two types of glass dosimeters was used to measure gamma doses close to the reactor.[7] Gamma doses from 20 to 50,000 rad were measured with small rods of AgPO$_3$ glass. Cobalt borosilicate glass plates were used to measure gamma doses between 1×10^4 and 5×10^6 rads. Both types of glass were placed in ^{6}Li-impregnated lead cans to minimize the effects of thermal neutrons and low energy gamma radiation.

Doses measured by the AgPO$_3$ glass rods were evaluated by use of a specially adapted fluorometer. Fluorescent centers produced in the glass by gamma radiation emit visible light when excited by ultraviolet radiation. The relative intensity of the emitted visible light is a measure of the radiation exposure of the rod. Fluorometer readings were converted into gamma dose values by means of calibration curves obtained by reading rods exposed to known gamma doses. Since no gamma doses greater than the detection range of the AgPO$_3$ rods were measured, no evaluation of the borosilicate glass plates was required.

Twelve holders containing a full complement of neutron threshold detectors and glass dosimeters were positioned on free-line poles on the railroad track along the 270° radial from 50 to 1,400 ft from the test point, to measure the variation of doses with distance. These holders were recovered within an hour after the event. Thirty-six holders containing sulfur and gold neutron threshold detectors and glass dosimeters were attached to wooden stakes at 20° intervals around the test point on arcs at 100 and 200 ft. This array was used to measure the radiation pattern around the reactor.

At 500 ft and beyond, Dupont type 544 film packets were used to measure gamma doses.[7] These packets contained a sensitive film, type 555, for doses from 0.01 to 6 R, and an insensitive film, type 834, for doses from 2 to 10^8 R. A 40-mil lead strip was placed over the packets to distinguish gamma radiation from beta radiation of less than 2.5 MeV. Each film packet was contained in a plastic wrapper to protect against moisture.

Pairs of film packets were located at 5° intervals completely around the test point on the 500-ft arc, and at 5° intervals between 130 and 310° on the 1,000- and 2,000-ft arcs. At 4,000 and 8,000 ft, packets were at 5° intervals between 180 and 270°. Film placement at 3, 6, 12, 24, and 50 miles was at approximately 10° intervals between 180 and 270°, the stations corresponding to air sampler locations. Integrating dosimetric devices were not collected from the field until 24 to 72 hours after the event.

Two remote-reading instrument systems were used to measure gamma dose rates following the excursion.[12] A photomultiplier/photovoltaic cell scintillator system was used at 500 ft and closer, and an ion-chamber system was used beyond 500 ft.

Scintillator stations were at 0, 90, 180, and 270° at 100, 200, and 500 ft. Six ion-chamber instruments were placed on each of five arcs, concentrated in the anticipated downwind direction, as listed in Table III.

TABLE III. LOCATION OF REMOTE READING IONIZATION CHAMBER STATIONS

Distance (ft)	Azimuth (°)					
500	45	120	150	210	240	315
1000	145	180	210	240	270	300
2000	160	190	220	250	280	310
4000	175	195	225	245	265	285
8000	180	200	220	240	260	280

The scintillator system employed fluorescent plastic, light-coupled to either photomultiplier (PM) tubes or to photovoltaic (PV) cells. The PM tubes were powered by high-voltage battery power supplies; the PV cells required no external power. Each scintillator station had one PM unit and one PV unit connected in parallel to a single coaxial signal line. These signal lines were approximately 2 miles long, and terminated in a readout facility in the control point area. The currents of the scintillator units were measured with transistorized galvanometers whose outputs were connected to strip chart recorders. A switching circuit allowed either of the two instruments connected to the signal line-galvanometer system to be read at one time. The PV system produced a constant signal in the transmission lines; the PM system produced a signal only when its power source was energized. The signals from the two systems were of opposite polarity. Although a PV signal automatically diminished a PM signal, because the PM signals were about two orders of magnitude greater, this interference was negligible.

The ionization chamber system was a commercially obtained RAMP 4 system, manufactured by the Jordan Electronics Division of Victoreen Instrument Company. Each remote station consisted of a Nehr-White ionization chamber and battery power supply. The remote stations were connected to the readout system by signal pairs, which were generally more than 2 miles long. The remote station ion chambers had a logarithmic response to radiation, and readout units were provided with two logarithmic range scales: 1 mR/hr to 10^3 mR/hr, and 1 R/hr to 10^3 R/hr.

After the event, numerous surveys were made with portable dose-rate survey instruments. Surveys by the Radiation Services Department of the Pan American World Airways, Inc., were largely confined to populated areas, such as building complexes and roadways, but included some areas around the test site. LASL Group H-1 Monitors conducted surveys to measure the location and extent of contamination around the test site and to accurately determine its variation with azimuth and distance from the test point.[13] Radiation measurements by LASL were made at accurately surveyed locations, and several serial measurements were made to accurately follow the decay of contamination. Readings were taken with pairs of instruments whose calibration was checked prior to each excursion into the field.

The variation of neutron flux with distance, as measured by the free-line stations along the railroad track, is shown in Fig. 21 and Table IV. The variation of neutron flux with azimuth around the test point is shown in Fig. 22 and Table V. Figure 23 shows the variation of neutron and gamma doses with distance along the free line. Figure 24 shows the variation of integral gamma doses with azimuth at 100 to 8,000 ft. Integral gamma doses are listed in Tables IV, V, and VI.

Data obtained from the remote-reading dose-rate systems are shown in Fig. 25. Contamination patterns determined by the monitor surveys are shown in Fig. 26. Typical decay data from the monitor surveys are shown in Fig. 27. These data were processed by electronic computer to obtain dose rate vs. time relationships in the form

$$DR = At^{-B} \qquad (6.1)$$

The values of A and B for representative stations are given in Table VII. The variations of dose rate with distance and azimuth as measured by the monitor surveys are shown in Figs. 28 and 29, respectively. Values for 1-hour data from monitor surveys are extrapolated by use of Eq. 6.1 from data actually taken several hours later. Values for A and B for representative stations are those presented in Table VII.

When these experiments were designed, emphasis was placed on obtaining maximum geographic coverage of the test point area, and on obtaining data from as many locations as possible. Duplication of instrumentation to check on reliability and accuracy of data, therefore, was sacrificed. Some cross checking of results is possible because of coincidental duplication of instrumentation, and further cross checking can be inferred by comparing the data to those obtained from other Kiwi tests.
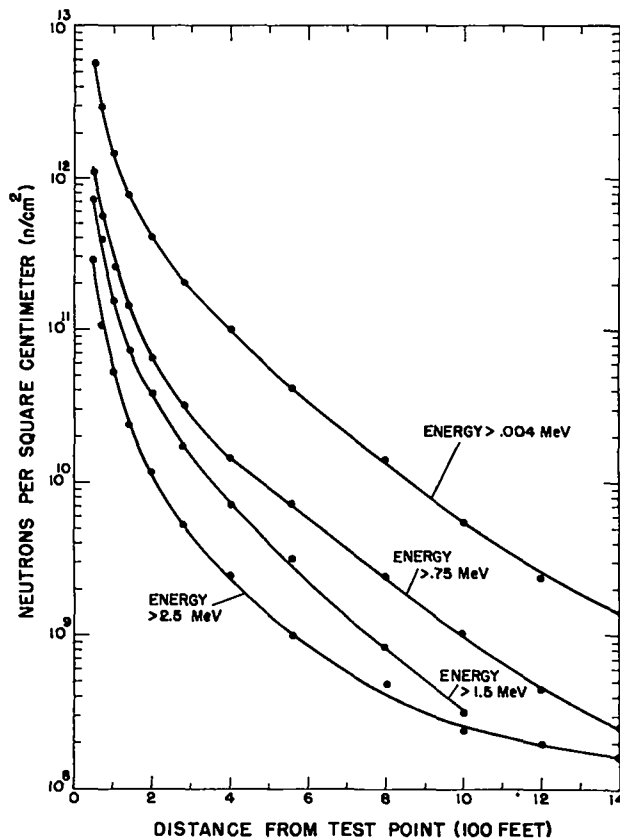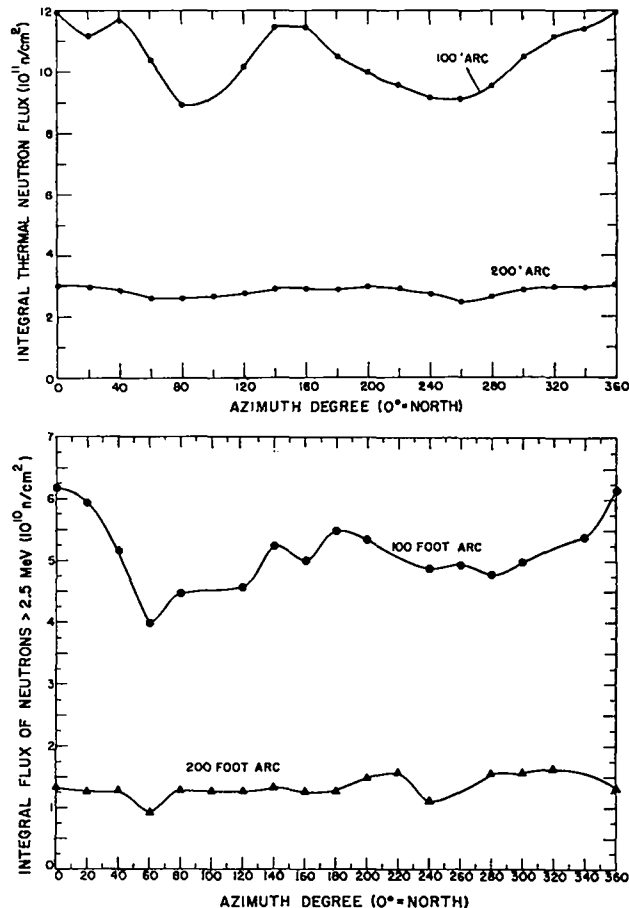
23

Fig. 21. Variation of neutron flux with distance.

Fig. 22. Variation of neutron flux with azimuth.

TABLE IV. INTEGRAL NEUTRON AND GAMMA DATA AT FREE LINE STATIONS

Distance (ft)	Integral Neutron Flux (n/cm²)					Rad Doses		
	φ Thermal	φ Pu[a]	φ Np[b]	φ U[c]	φ S[d]	n_f Rads	n_t Rads	γ Rads
50	2.88×10^{12}	5.74×10^{12}	1.15×10^{12}	7.27×10^{11}	2.91×10^{11}	8.61×10^{3}	1.59×10^{2}	1.05×10^{4}
70	1.70×10^{12}	2.95×10^{12}	5.58×10^{11}	3.99×10^{11}	1.03×10^{11}	3.86×10^{3}	9.4×10^{1}	1.06×10^{4}
100	8.73×10^{11}	1.47×10^{12}	2.61×10^{11}	1.53×10^{11}	5.33×10^{10}	1.87×10^{3}	4.8×10^{1}	5.70×10^{3}
140	4.96×10^{11}	7.87×10^{11}	1.42×10^{11}	7.41×10^{10}	2.47×10^{10}	9.96×10^{2}	2.7×10^{1}	1.89×10^{3}
200	2.47×10^{11}	4.13×10^{11}	6.57×10^{10}	3.78×10^{10}	1.17×10^{10}	5.09×10^{2}	1.4×10^{1}	1.36×10^{3}
280	1.21×10^{11}	2.04×10^{11}	3.16×10^{11}	1.76×10^{10}	5.35×10^{9}	2.49×10^{2}	6.7	7.33×10^{2}
400	5.51×10^{10}	9.97×10^{10}	1.46×10^{10}	7.08×10^{9}	2.43×10^{9}	1.19×10^{2}	3	2.82×10^{2}
560	2.22×10^{10}	4.05×10^{10}	7.32×10^{9}	3.33×10^{9}	9.90×10^{8}	5.07×10^{1}	1.2	1.30×10^{2}
800	8.35×10^{9}	1.33×10^{10}	2.42×10^{9}	8.24×10^{8}	4.81×10^{8}	1.67×10^{1}	4.6×10^{-1}	6.30×10^{1}
1000	3.49×10^{9}	5.55×10^{9}	1.00×10^{9}	3.15×10^{8}	2.44×10^{8}	6.93	1.9×10^{-1}	4.69×10^{1}
1200	1.63×10^{9}	2.38×10^{9}	4.30×10^{8}	Low	1.91×10^{8}	4.00	9.0×10^{-2}	5.10×10^{1}
1400	9.84×10^{8}	1.41×10^{9}	2.55×10^{8}	Low	1.60×10^{8}	3.00	5.4×10^{-2}	1.00×10^{1}

(a) φPu = Integral neutron fluxes at energies >0.004 MeV

(b) φNp = Integral neutron fluxes at energies >0.75 MeV

(c) φU = Integral neutron fluxes at energies >1.50 MeV

(d) φS = Integral neutron fluxes at energies >2.50 MeV

TABLE V. INTEGRAL GAMMA AND NEUTRON DATA AT 100 AND 200 FEET

Distance[a] (ft)	Bearing (°)	γ rads	S flux[b] (n/cm²)	n_{th} flux[c] (n/cm²)	n_{th} rads	Cd ratio
100	0	3.64×10^8	6.16×10^{10}	1.19×10^{12}	6.57×10^1	2.64
100	20	3.68×10^8	5.94×10^{10}	1.11×10^{12}	6.12×10^1	2.54
100	40	3.51×10^8	5.16×10^{10}	1.16×10^{12}	6.42×10^1	2.64
100	60	3.16×10^8	3.98×10^{10}	1.03×10^{12}	5.69×10^1	2.56
100	80	3.18×10^8	4.48×10^{10}	8.91×10^{11}	4.90×10^1	2.42
100	100	1.53×10^8	7.27×10^9	6.28×10^{11}	3.45×10^1	2.69
100	120	3.34×10^8	4.56×10^{10}	1.01×10^{12}	5.58×10^1	2.66
100	140	4.24×10^8	5.23×10^{10}	1.14×10^{12}	6.28×10^1	2.56
100	160	4.43×10^8	5.00×10^{10}	1.14×10^{12}	6.28×10^1	2.67
100	180	4.93×10^8	5.49×10^{10}	1.04×10^{12}	5.76×10^1	2.58
100	200	4.97×10^8	5.35×10^{10}	9.99×10^{11}	5.49×10^1	2.55
100	220	4.91×10^8	—	9.56×10^{11}	5.26×10^1	2.51
100	240	3.97×10^8	4.87×10^{10}	9.14×10^{11}	5.03×10^1	2.56
100	260	3.62×10^8	4.95×10^{10}	9.13×10^{11}	5.02×10^1	2.53
100	280	3.32×10^8	4.78×10^{10}	9.57×10^{11}	5.26×10^1	2.59
100	300	3.12×10^8	5.00×10^{10}	1.04×10^{12}	5.75×10^1	2.62
100	320	4.02×10^8	—	1.11×10^{12}	6.12×10^1	2.54
100	340	3.94×10^8	5.38×10^{10}	1.13×10^{12}	6.24×10^1	2.58
200	0	1.05×10^8	1.32×10^{10}	3.04×10^{11}	1.67×10^1	2.40
200	20	1.09×10^8	1.25×10^{10}	2.97×10^{11}	1.63×10^1	2.39
200	40	1.02×10^8	1.26×10^{10}	2.85×10^{11}	1.57×10^1	2.31
200	60	8.40×10^2	9.19×10^9	2.59×10^{11}	1.42×10^1	2.31
200	80	8.93×10^2	1.28×10^{10}	2.59×10^{11}	1.42×10^1	2.29
200	100	1.01×10^3	1.26×10^{10}	2.68×10^{11}	1.47×10^1	2.40
200	120	1.11×10^3	1.25×10^{10}	2.78×10^{11}	1.53×10^1	2.33
200	140	1.35×10^3	1.32×10^{10}	2.78×10^{11}	1.60×10^1	2.47
200	160	1.56×10^3	1.22×10^{10}	2.89×10^{11}	1.59×10^1	2.38
200	180	2.09×10^3	1.26×10^{10}	2.88×10^{11}	1.58×10^1	2.38
200	200	2.71×10^3	1.44×10^{10}	2.97×10^{11}	1.63×10^1	2.47
200	220	2.23×10^3	1.57×10^{10}	2.88×10^{11}	1.58×10^1	2.46
200	240	1.48×10^3	1.10×10^{10}	2.73×10^{11}	1.50×10^1	2.39
200	260	1.55×10^3	—	2.45×10^{11}	1.34×10^1	2.37
200	280	1.00×10^3	1.55×10^{10}	2.67×10^{11}	1.47×10^1	2.46
200	300	1.08×10^3	1.56×10^{10}	2.87×10^{11}	1.58×10^1	2.40
200	320	1.15×10^3	1.62×10^{10}	2.95×10^{11}	1.62×10^1	2.36
200	340	1.09×10^3	3.80×10^{10}	2.96×10^{11}	1.62×10^1	2.34

(a) Distances are measured from a verticle line through the core center of the reactor.

(b) Integral neutron fluxes at energies >2.50 MeV.

(c) Integral neutron fluxes at energies <0.3 eV.

TABLE VI.   GAMMA DOSES OBTAINED BY DOSIMETRY FILMS

Station Distance (10^8 ft)	Azimuth (°)	Dose (mR)	Station Distance (10^8 ft)	Azimuth (°)	Dose (mR)
0.5	00	1.18×10^5	0.5	260	1.30×10^5
0.5	05	7.20×10^4	0.5	265	1.27×10^5
0.5	10	5.00×10^4	0.5	270	1.40×10^5
0.5	15	4.15×10^4	0.5	275	1.23×10^5
0.5	20	1.20×10^5	0.5	280	1.12×10^5
0.5	25	8.35×10^4	0.5	285	1.69×10^5
0.5	30	1.10×10^5	0.5	290	1.09×10^5
0.5	35	1.05×10^5	0.5	295	1.07×10^5
0.5	40	8.40×10^4	0.5	300	1.17×10^5
0.5	45	8.95×10^4	0.5	305	1.19×10^5
0.5	50	7.10×10^4	0.5	310	1.33×10^5
0.5	55	8.60×10^4	0.5	315	1.30×10^5
0.5	60	7.75×10^4	0.5	320	1.45×10^5
0.5	65	8.45×10^4	0.5	325	1.29×10^5
0.5	70	5.75×10^4	0.5	330	8.40×10^4
0.5	75	1.03×10^5	0.5	335	1.13×10^5
0.5	80	1.30×10^5	0.5	340	1.04×10^5
0.5	85	1.06×10^5	0.5	345	1.07×10^5
0.5	90	1.09×10^5	0.5	350	1.08×10^5
0.5	95	1.55×10^5	0.5	355	1.04×10^5
0.5	100	5.30×10^4	1	130	1.33×10^4
0.5	105	8.70×10^4	1	135	1.25×10^4
0.5	110	7.75×10^4	1	140	Lost
0.5	115	1.14×10^5	1	145	1.10×10^4
0.5	120	1.10×10^5	1	150	1.00×10^4
0.5	125	1.21×10^5	1	155	1.35×10^4
0.5	130	1.03×10^5	1	160	1.33×10^4
0.5	135	8.40×10^4	1	165	1.80×10^4
0.5	140	9.70×10^4	1	170	1.85×10^4
0.5	145	1.13×10^5	1	175	2.20×10^4
0.5	150	1.27×10^5	1	180	2.60×10^4
0.5	155	1.21×10^5	1	185	2.58×10^4
0.5	160	1.30×10^5	1	190	2.63×10^4
0.5	165	1.32×10^5	1	195	3.03×10^4
0.5	170	1.72×10^5	1	200	3.78×10^4
0.5	175	2.75×10^5	1	205	1.26×10^5
0.5	180	1.65×10^5	1	210	5.60×10^4
4	185	2.00×10^1	1	215	3.60×10^4
0.5	190	1.53×10^5	1	220	2.63×10^4
0.5	195	1.60×10^5	1	225	2.55×10^4
0.5	200	2.90×10^5	1	230	2.20×10^4
0.5	205	4.00×10^5	1	235	2.20×10^4
0.5	210	2.80×10^5	1	240	1.53×10^4
0.5	215	2.43×10^5	1	245	1.55×10^4
0.5	220	2.83×10^5	1	250	5.55×10^4
0.5	225	2.25×10^5	1	255	5.15×10^4
0.5	230	2.25×10^5	1	260	4.95×10^4
0.5	235	2.20×10^5	1	265	5.15×10^4
0.5	240	2.15×10^5	1	270	4.85×10^4
0.5	245	1.50×10^5	1	275	4.60×10^4
0.5	250	1.36×10^5	1	280	1.63×10^4
0.5	255	1.32×10^5	1	285	1.53×10^4

TABLE VI. CONTINUED

Station			Station		
Distance (10³ ft)	Azimuth (°)	Dose (mR)	Distance (10³ ft)	Azimuth (°)	Dose (mR)
1	290	1.63×10^4	4	250	1.30×10^2
1	295	1.58×10^4	4	255	4.00×10^1
1	300	8.35×10^3	4	260	3.00×10^1
1	305	1.50×10^4	4	265	1.00×10^1
1	310	1.50×10^4	4	270	<10
2	130	1.65×10^3	8	180	<10
2	135	1.60×10^3	8	185	<10
2	140	1.58×10^3	8	190	<10
2	145	1.45×10^3	8	195	<10
2	150	1.65×10^3	8	200	1.00×10^1
2	155	1.70×10^3	8	205	3.00×10^1
2	160	1.85×10^3	8	210	1.50×10^2
2	165	1.99×10^3	8	215	2.45×10^2
2	170	2.08×10^3	8	220	1.35×10^2
2	175	2.55×10^3	8	225	5.00×10^1
2	180	3.00×10^3	8	230	1.00×10^1
2	185	3.38×10^3	8	235	<10
2	190	3.87×10^3	8	240	3.00×10^1
2	195	6.30×10^3	8	245	<10
2	200	4.05×10^4	8	250	<10
2	205	1.68×10^4	8	255	<10
2	210	5.55×10^3	8	260	<10
2	215	4.55×10^3	8	270	<10
2	220	4.05×10^3	16	180	<10
2	225	3.45×10^3	16	190	<10
2	230	2.99×10^3	16	200	<10
2	235	2.63×10^3	16	210	3.35×10^2
2	240	2.80×10^3	16	220	<10
2	245	3.00×10^3	16	230	<10
2	250	2.08×10^3	16	240	<10
2	255	2.03×10^3	16	252	<10
2	260	1.93×10^3	16	261	<10
2	265	2.08×10^3	16	270	<10
2	270	1.55×10^3	32	194	<10
2	275	1.30×10^3	32	206	<10
2	280	1.30×10^3	32	219	1.50×10^2
2	285	1.60×10^3	32	228	<10
2	290	1.63×10^3	32	245	<10
2	295	1.25×10^3	32	250	<10
2	300	1.15×10^3	64	172	<10
2	305	9.50×10^2	64	188	<10
2	310	5.95×10^2	64	203	<10
4	180	2.50×10^1	64	211	<10
4	185	2.00×10^1	64	215	<10
4	190	6.50×10^1	64	221	1.00×10^1
4	195	1.15×10^2	64	230	<10
4	200	1.50×10^2	64	241	<10
4	205	1.90×10^2	64	251	<10
4	210	3.30×10^2	64	268	<10
4	215	2.08×10^3	128	180	
4	220	3.95×10^2	to		<10
4	225	2.25×10^2	128	280	
4	230	2.10×10^2	256	183	
4	235	1.45×10^2	to		<10
4	240	7.00×10^1	264	253	
4	245	6.00×10^1			

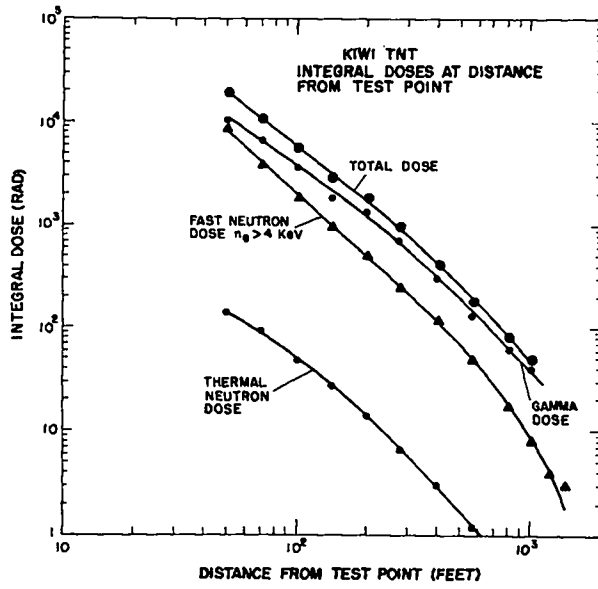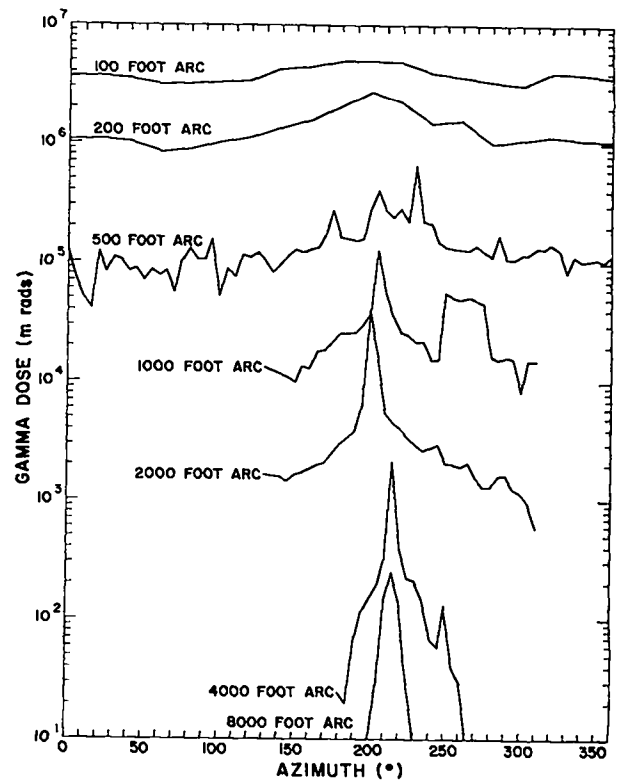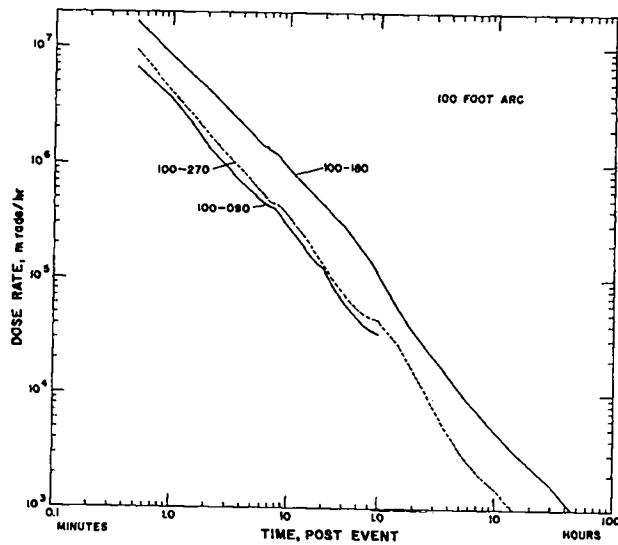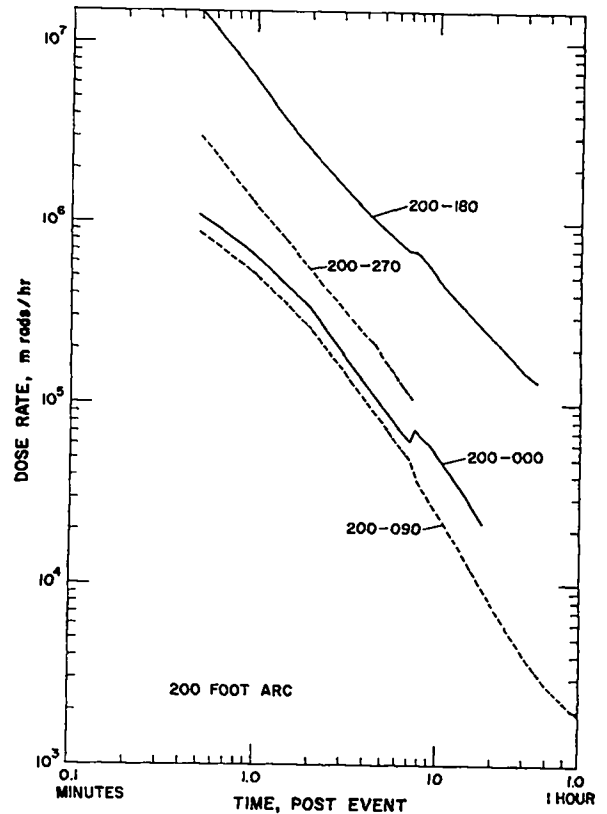Fig. 23. Variation of neutron and gamma doses with distance.

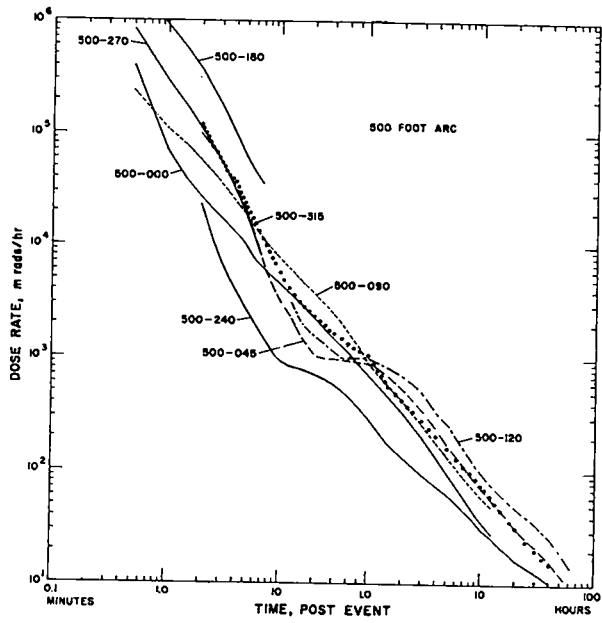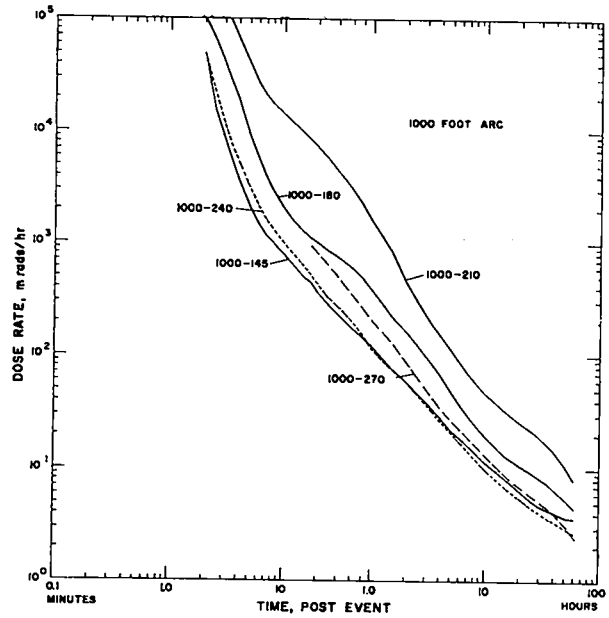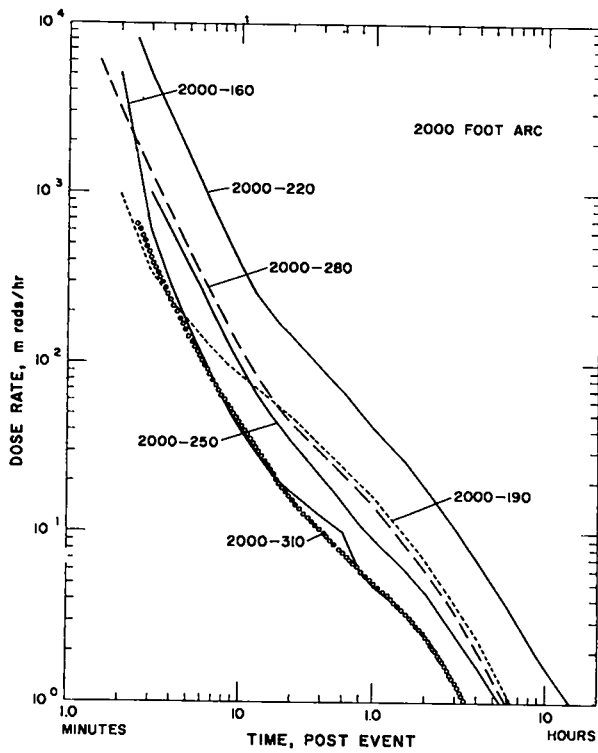Fig. 24. Variation of integral gamma doses with azimuth, as measured by film badges.

a.

b.

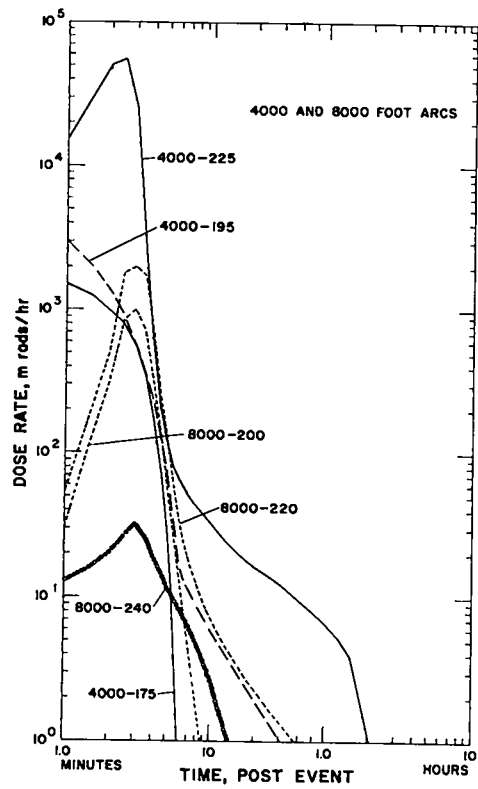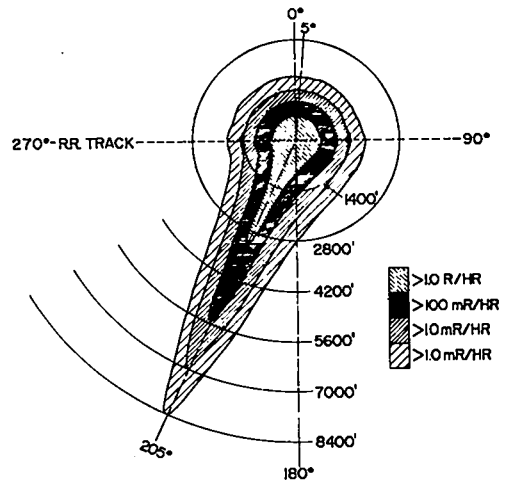Fig. 25. Data obtained from remote reading dose-rate instruments.

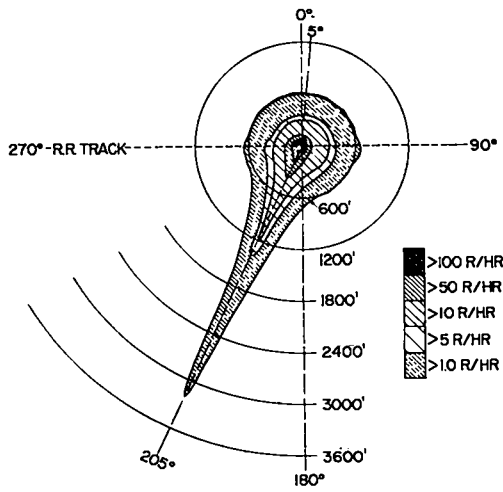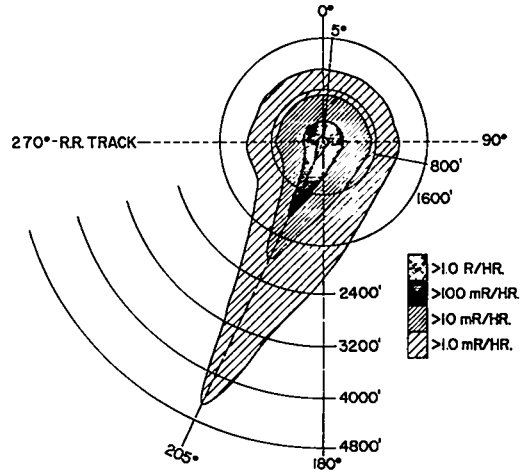Fig. 25. Continued.

29

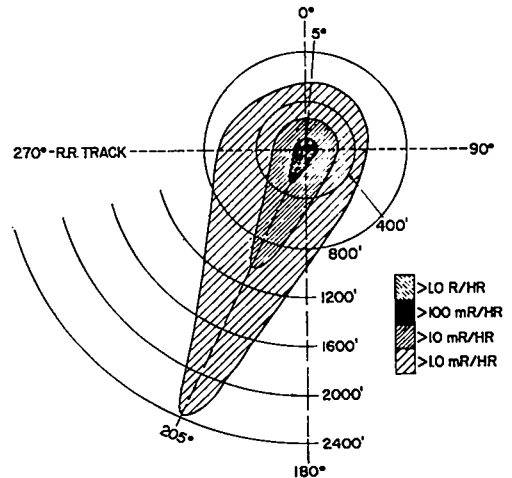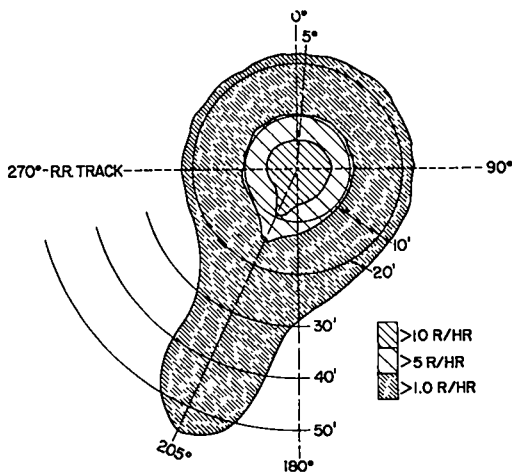**a.**

One Hour

b.

c.

One Day

d.

e.

One Week

f.
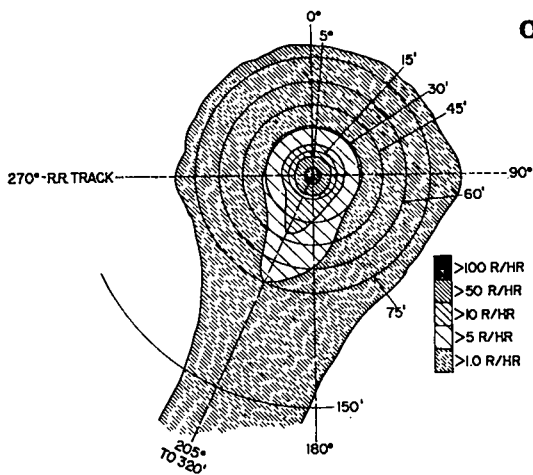
Fig. 26. Contamination patterns determined by monitor surveys.

30

TABLE VII. COMPARISONS OF DOSIMETRIC DATA

| Station | Monitor Survey Decay Constants Dose Rate = At^{-B} | | $\int At^{-B}$ | | Integral of Dose-Rate Recording (mR) | Integral Dosimeter Dose (mR) |
	A (mR/hr)	B	1 min to 48 hr (mR)	2 min to 48 hr (mR)		
100-000	5.12×10^4	1.28	5.50×10^5	4.13×10^5	6.20×10^5	3.64×10^6
100-080	1.65×10^4	1.14	1.40×10^5	1.21×10^5		3.18×10^6
100-090					4.49×10^5	
100-100	2.56×10^4	1.28	2.58×10^5	2.07×10^5		
100-180	2.16×10^5	1.45	2.97×10^6	2.15×10^6	1.45×10^6	4.39×10^6
100-260	9.00×10^3	0.93	7.21×10^4	6.73×10^4		3.62×10^6
100-270					6.20×10^5	
100-280	2.24×10^4	1.18	1.97×10^5	1.67×10^5		3.32×10^6
200-000	2.16×10^4	1.39	2.63×10^5	1.97×10^5	2.78×10^5	1.05×10^6
200-080	2.17×10^4	1.46	3.00×10^5	2.16×10^5		8.93×10^5
200-090	2.24×10^4	1.54	3.76×10^5	2.57×10^5	1.62×10^5	
200-100	1.25×10^4	1.33	1.35×10^5	1.05×10^5		1.01×10^6
200-180	4.53×10^4	1.18	3.98×10^5	3.38×10^5	8.99×10^5	2.09×10^6
200-260	3.39×10^4	1.40	4.18×10^5	3.12×10^5		1.55×10^6
200-270	9.69×10^3	1.18	8.53×10^4	7.23×10^4	3.66×10^5	
200-280	2.85×10^4	1.41	3.60×10^5	2.70×10^5		1.00×10^6
500-000	2.78×10^3	1.46	3.90×10^4	2.80×10^4	2.18×10^5	1.18×10^5
500-040	2.60×10^3	1.54	4.37×10^4	2.98×10^4		8.40×10^4
500-045					7.36×10^3	8.95×10^4
500-050	2.61×10^3	1.55	4.41×10^4	3.00×10^4		7.10×10^4
500-090	2.59×10^3	1.47	3.72×10^4	2.65×10^4	1.89×10^4	1.09×10^5
500-120	1.66×10^3	1.3	1.71×10^4	1.36×10^4	5.75×10^3	1.10×10^5
500-180	5.70×10^3	1.26	5.57×10^4	4.51×10^4	1.46×10^5	1.65×10^5
500-240	7.54×10^3	1.34	8.37×10^4	6.48×10^4	2.28×10^3	2.15×10^5
500-270	4.62×10^3	1.36	5.26×10^4	4.03×10^4	9.20×10^4	1.40×10^5
500-310	3.30×10^3	1.34	3.67×10^4	2.84×10^4		1.33×10^5
500-315					8.11×10^3	1.30×10^5
500-320	2.55×10^3	1.16	2.21×10^4	1.89×10^4		1.45×10^5
1000-140	1.78×10^2	1.3	1.84×10^3	1.46×10^3		
1000-145					1.33×10^3	1.10×10^4
1000-150	1.43×10^2	1.3	1.48×10^3	1.17×10^3		1.00×10^4
1000-180	5.39×10^2	1.3	5.57×10^3	4.42×10^3	3.86×10^3	2.60×10^4
1000-210	3.90×10^3	1.3	4.03×10^4	3.20×10^4	1.54×10^4	5.60×10^4
1000-240	2.42×10^2	1.3	2.50×10^3	1.98×10^3	1.48×10^3	1.53×10^4
1000-270	2.08×10^2	1.3	2.15×10^3	1.71×10^3	9.37×10^2	4.85×10^4
1000-300	1.70×10^2	1.3	1.76×10^3	1.39×10^3		8.35×10^3
2000-160					6.54×10^1	1.85×10^3
2000-190	5.52	1.3	5.71×10^1	4.53×10^1	7.79×10^1	3.87×10^3
2000-220	1.19×10^3	1.3	1.23×10^4	9.74×10^3	3.74×10^2	4.05×10^3
2000-250	4.58×10^1	1.3	4.74×10^2	3.76×10^2	7.02×10^1	2.08×10^3
2000-270	2.81×10^1	1.3	2.91×10^2	2.31×10^2		1.55×10^3
2000-280					1.62×10^2	1.30×10^3
2000-310					3.48×10^1	5.95×10^2
4000-175					4.16×10^1	
4000-195					6.02×10^1	1.15×10^2
4000-220	9.59	1.3	9.92×10^1	7.87×10^1		3.95×10^2
4000-225					1.46×10^3	2.25×10^2
4000-230	2.71	1.3	2.80×10^1	2.22×10^1		2.10×10^2
8000-200	3.39×10^{-1}	1.3	3.50	2.78	2.95×10^1	1×10^1
8000-220	1.72	1.3	1.78×10^1	1.41×10^1	6.20×10^1	1.35×10^2
8000-240	3.69×10^{-1}	1.3	3.82	3.03	1.97	3×10^1
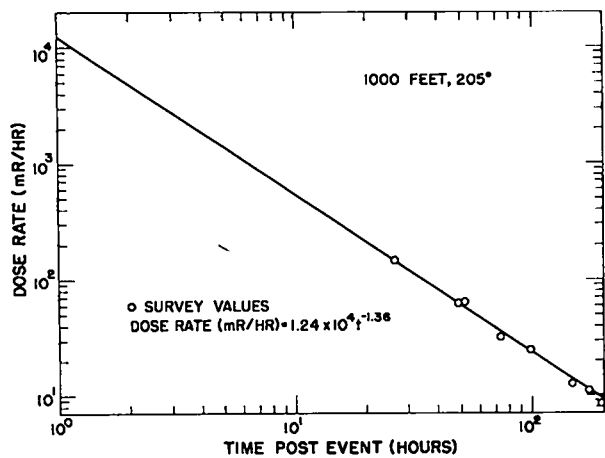
Fig. 27. Typical monitor survey dose-rate decay data.
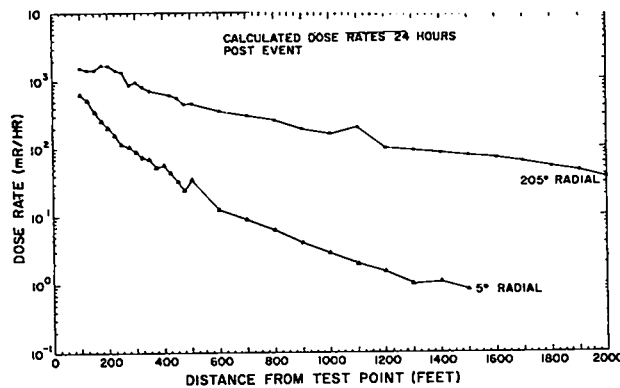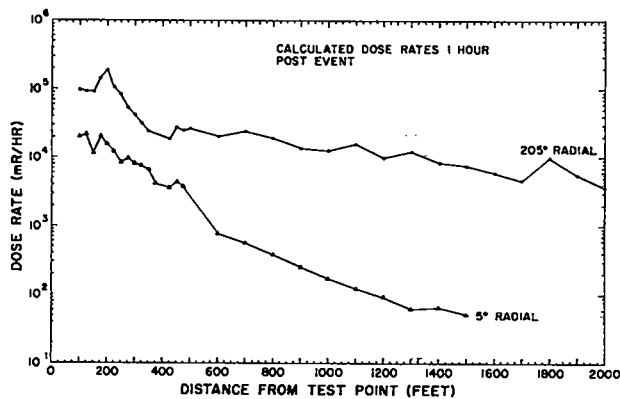
Fig. 28. Variations of dose rate with distance.

Fig. 29. Variations of dose rate with azimuth.

these ratios are somewhat lower and within the range found in normally operated Kiwi reactors.

Table VIII lists ratios of neutron doses from Kiwi-TNT to those from Kiwi-B4D-202 and Kiwi-B4E-301 at selected distances. All data used to compute the values in Table VIII were normalized to rads/MW-sec of reactor energy and it was assumed that 3.1×10^{20} fissions occurred during the Kiwi-TNT excursion. If 3.4×10^{20} fissions are assumed (the value at the upper limit of error of the radiochemical determination of total fissions),

TABLE VIII. KIWI-TNT RADIATION MEAS-UREMENTS COMPARED TO KIWI-B4D AND -B4E DATA

| Distance from Reactor (ft) | Ratios of Dose/MW-sec of Reactor Energy Neutron Doses | |
	TNT/B4D	TNT/B4E
50	1.14	1.11
70	1.00	1.24
100	1.01	1.17
140	1.12	1.26
200	1.23	1.34
280	1.28	1.32
400	1.35	1.37
560	1.31	1.28
800	1.11	1.07
1000	0.89	0.94

Fig. 30. Normalized integral gamma doses from several reactor tests.

Figure 30 compares normalized integral gamma doses from the free line with normalized doses from previous reactor tests. The Kiwi-TNT values are higher than those encountered with normal reactors except for the very close stations. This can perhaps be explained as follows: Free-line doses from a normal reactor contain a contribution from prompt gammas (those released simultaneously with the fission reaction) and a contribution from delayed, fission-product decay gammas for about 10 to 15 minutes after a run. Normally, both contributions are reduced from their theoretical maximum value by the shielding provided by the reactor reflector and pressure vessel materials, and by self-absorption within the core. This reduction is about a factor of 5.

Delayed gamma energy in the first minute after fission is about 30% of the prompt gamma energy, and in the first 10 minutes it is about 40% of prompt gamma energy. In the Kiwi-TNT experiment, the dosimetric devices were exposed to the prompt gamma energy shielded by the essentially intact reactor components (as in a normal test), and were also exposed to the largely unshielded delayed gammas (emanating from the cloud of reactor debris) for about 1 minute. Ap-

proximate calculations show that doses/MW-sec of reactor energy from a Kiwi-TNT type of situation will be about twice those from a normal reactor. The geometry of the test also shows that the dosimeters further from the test point will have a more constant, or more slowly changing, source-to-detector distance (when the moving radioactive cloud is the source) than those close to the test point. Because of the strong wind during this test, the influence of the fission-product cloud on the close-in stations diminished rapidly, but its influence on more remote stations changed little during the first minute or so. Therefore, the farther-out stations could be expected to registe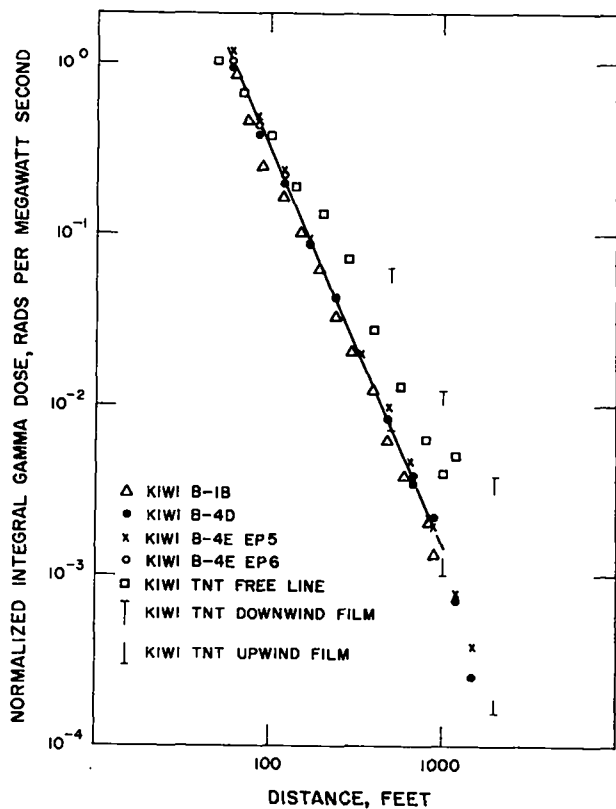r proportionately higher integral doses than those at closer range. Since the free-line dosimeters were recovered from the field within an hour after the event (all but the innermost few within 15 minutes), they were not unduly influenced by radioactive contamination.

Dosimeters other than those on the free line remained in the field, under the influence of radiation from contamination, for 24 to 72 hours. To determine the fraction of total dose due to radiation from contamination, Eq. 6.1 was integrated with respect to time over the interval from 1 or 2 minutes to 48 hours, for which time a dosimeter remained at each station. Table VIII compares doses measured by glass rods and film badges with integrations of Eq. 6.1. Included for comparison are numerical integrals of the dose-rate records presented in Fig. 25. With a few exceptions, the doses measured by the integrating devices are substantially greater than the integrals of dose rates. This is to be expected since the integrating devices readily responded to the prompt radiation, whereas the dose-rate recorders, because of their response times, could be used only to measure delayed radiation. Because of saturation problems, most of the ion chambers did not provide any information until 2 minutes after the event, by which time the cloud was nearly 4,000 ft from the test point. Therefore, except for the 4,000- and 8,000-ft data, ion-chamber data are considered to be solely a measure of radiation from ground contamination.

Scintillator system data are considered to be reasonably reliable after about half a minute, but values for earlier times are merely extrapolations. Numerical integrations of the scintillator data are presented for times beyond ½ minute, and are also considered to represent only radiation from ground contamination, although there may still have been a small influence from the cloud at very early times. The severe fluctuations of dose with azimuth

33

as measured by film badge are considered to be due largely to radiation from ground contamination. Correlation between film badge doses and integrations of dose rates is poor, even allowing for the discrepancy due to prompt and cloud radiation; this is attributed to the fact that doses and dose rates were measured at slightly different locations at the same station. Since ground contamination included discrete fragments with high specific activity, the dose rate at some stations was found to vary considerably for two points separated by only a few yards.

That film badge doses were perturbed by ground contamination or other causes is indicated in Fig. 24. The peak doses registered along the deposition pattern center line at 200 to 215° could not have been caused by radiation from the cloud alone, unless the cloud behaved as a point source traveling at ground level, which photographic evidence contradicts. A calculation of radiation dose from an elevated source of reasonable geometry (e.g., sphere, point, line, sausage, or ameoba) yields doses much more uniform with respect to azimuth than those measured.

The accuracy of data collected by the dose-rate systems is also subject to question. The plots of dose rate versus time on the log-log scales used in Fig. 25 should have yielded nearly straight lines as is the case when activities of theoretical fission product mixtures are plotted in this fashion. Some variations are expected, but the deviations in some of the lines in Fig. 25c are strongly suspected of being due to meter error, especially since they occur around a scale-shift point. Also, the plot for the recorder at Station 500-240 represents the lowest dose rates measured at that distance although that station was more coincident with the cloud path than any other at that distance.

It is also recognized that values extrapolated to 1 hour from data actually obtained a day or more after the test, as is the case for the monitor survey data, must be used with reservation. This was, however, information collected during the test and should be used only for what it is worth in checking the accuracy of other data.

Although much criticism has been leveled herein at the instrumentation systems used, it must be recognized that they are representative of carefully calibrated instrumentation used in nuclear radiation measurements, and they are little worse, and probably better, than most. In addition, although individual data points are questionable, the aggregate is highly useful in determining the exposures and hazards to be encountered in an excursion such as the Kiwi-TNT.

To determine the contribution of each individual source of radiation (i.e., prompt, neutron, cloud, or contamination) to the total personnel exposure at given distances in the vicinity of an accidental excursion similar to the Kiwi-TNT, the following exercise was performed. Reference to Table IX will aid in following this discussion. The dose measured by the integral dosimeter at each station was recorded. From this was subtracted a contribution attributable to prompt gamma radiation derived from previous tests of Kiwi reactors (Fig. 30). The value of rads/MW-sec was 70% of the total rads/MW-sec measured on previous tests. The difference between the total dose and the prompt gamma dose is then due to doses from the debris cloud and ground contamination. The numerical integral of the dose-rate data (beyond ½ minute for scintillator stations, beyond 2 minutes for other stations) was taken as the contribution from ground contamination. Some loss of precision is involved in this step, since the intervals of integration varied and did not correspond to the times the integrating dosimeters were actually in the field. However, these integrals are largely representative of the dose from ground contamination, since the major fraction was received during the earliest minutes. Subtracting the dose rate integral from the cloud and deposition dose yields the cloud dose. The values obtained are given in Table IX. Plots of these individual exposures for the downwind and upwind directions are given in Fig. 31, where the prompt gamma dose is that obtained, as explained, from previous Kiwi reactor tests. The neutron dose is that actually measured during this test, since it is relatively free of the influence of such factors as weather, cloud, and deflagration. The cloud dose is largely either the maximum or minimum value derived in Table IX. Sometimes this value was modified to make it consistent with all doses measured at a given distance or other geometrical factor. The deposition dose given in Fig. 30 is derived by taking the numerical integral of the dose rate at the various stations from time of arrival of the cloud until 5 minutes after the excursion. This value was considered representative of the exposure one would receive from deposited activity if he were caught in an accidental excursion and had to evacuate the area.

Personnel hazards are summarized as follows: Out to approximately 300 ft, almost all radiation exposures would be fatal, being in excess of 1,000 rads. Between approximately 300 and 600 ft, varying degrees of radiation injury including some fatalities, would occur as exposures would be between 200 and 1,000 rads. Between approximately 600 and 750 ft, exposures would be between 100 and 200 rad, producing slight illness. From 750 to

TABLE IX. CALCULATIONS OF COMPONENTS OF TOTAL EXPOSURE

| Station	Integral Dosimeter Dose (mR)	Prompt Dose (from Fig. 6.10) (mR)	Cloud + Deposition (mR)	Integral of Dose Rate Record (Deposition) (mR)	Cloud Dose (mR)	5 min Deposition Dose (mR)
100-090	3.2×10^6	2.3×10^6	9×10^5	1.2×10^5	7.8×10^5	1.2×10^5
100-180	4.9×10^6	2.3×10^6	2.6×10^6	9.1×10^5	1.7×10^6	3.3×10^5
100-270	3.5×10^6	2.3×10^6	1.2×10^6	3.5×10^5	7.7×10^5	1.5×10^5
200-000	1.0×10^6	4.5×10^5	6×10^5	3.4×10^4	5.7×10^5	2.4×10^4
200-090	9.4×10^5	4.5×10^5	4.9×10^5	2.5×10^4	4.7×10^5	2.0×10^4
200-180	2.1×10^6	4.5×10^5	1.6×10^6	3.8×10^5	1.2×10^6	2.2×10^5
200-270	1.3×10^6	4.5×10^5	8.3×10^5	5.0×10^4	7.8×10^5	4.6×10^4
500-000	1.2×10^5	5.2×10^4	6.8×10^4	6.2×10^3	6.2×10^4	3.0×10^3
500-090	1.1×10^5	5.2×10^4	5.7×10^4	6.7×10^3	5.0×10^4	4.3×10^3
500-180	1.6×10^5	5.2×10^4	1.1×10^5	3.2×10^4	8.0×10^4	3.0×10^4
500-270	1.4×10^5	5.2×10^4	8.8×10^4	9.9×10^3	7.8×10^4	9.5×10^3
500-045	8.9×10^4	5.2×10^4	3.7×10^4	7.4×10^3	3.0×10^4	2.4×10^3
500-120	1.1×10^5	5.2×10^4	5.8×10^4	5.8×10^3	5.2×10^4	—
500-240	2.1×10^5	5.2×10^4	1.6×10^5	2.3×10^3	1.6×10^5	3.5×10^2
500-315	1.3×10^5	5.2×10^4	7.8×10^4	8.1×10^3	7.0×10^4	2.5×10^3
1000-145	1.1×10^4	1.0×10^4	1.0×10^3	1.3×10^3	—	4.8×10^2
1000-180	2.6×10^4	1.0×10^4	1.6×10^4	3.9×10^3	1.2×10^4	1.8×10^3
1000-210	5.6×10^4	1.0×10^4	4.6×10^4	1.5×10^4	3.1×10^4	6.7×10^3
1000-240	1.5×10^4	1.0×10^4	5.0×10^3	1.5×10^3	3.5×10^3	6.2×10^2
1000-270	4.8×10^4	1.0×10^4	3.8×10^3	9.4×10^2	2.9×10^3	—
1000-300	8.4×10^3	1.0×10^4	—	1.3×10^3	—	4.8×10^2
2000-160	1.8×10^3	7.0×10^2	1.1×10^3	6.5×10^1	1.1×10^3	4.3×10^1
2000-190	3.9×10^3	7.0×10^2	3.2×10^3	7.8×10^1	3.1×10^3	1.8×10^1
2000-220	4.0×10^3	7.0×10^2	3.3×10^3	3.8×10^2	2.9×10^3	1.5×10^2
2000-250	2.1×10^3	7.0×10^2	1.4×10^3	7.0×10^1	1.3×10^3	2.1×10^1
2000-280	1.3×10^3	7.0×10^2	6.0×10^2	1.6×10^2	4.4×10^2	9.5×10^1
2000-310	6.0×10^2	7.0×10^2	—	3.5×10^1	—	1.2×10^1
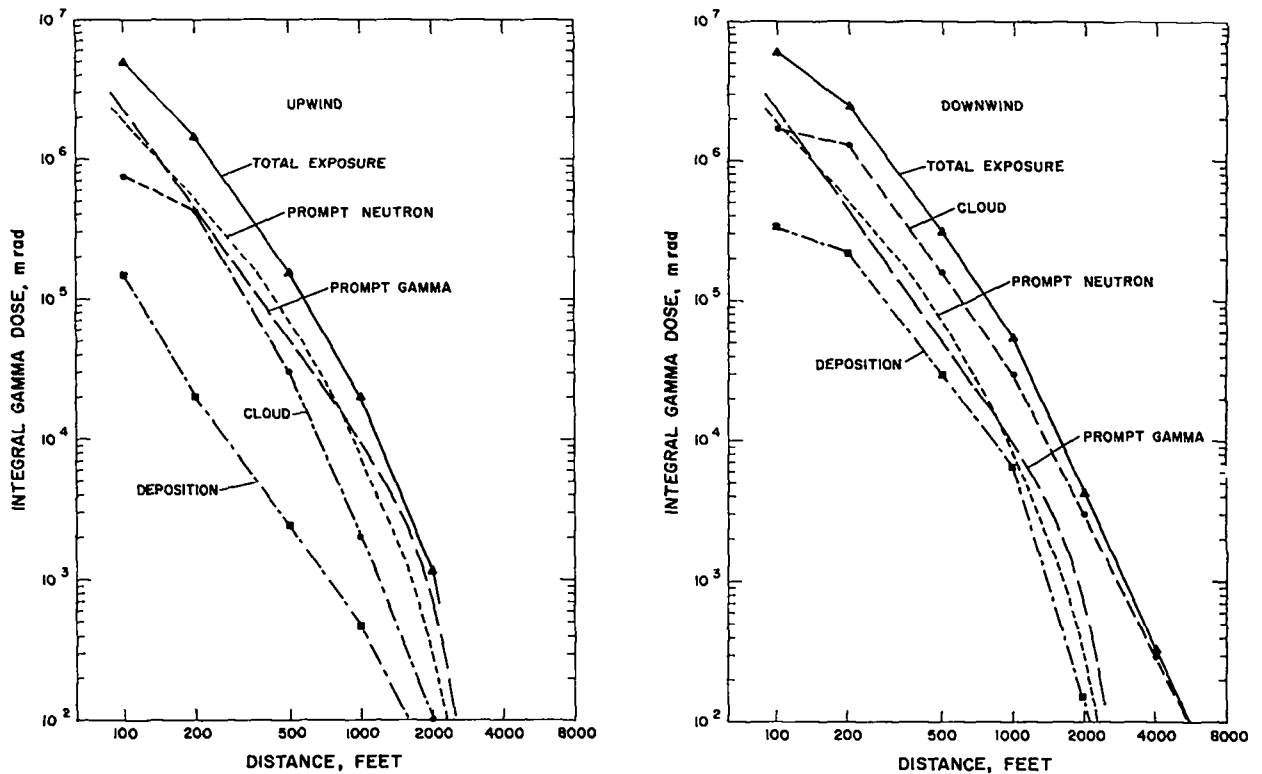
Fig. 31. Components of radiation exposure vs. distance.

1,200 ft, exposures would range from 25 to 100 rad, producing some very slight hemotological change, but no illness. Beyond 1,200 ft, out to approximately 2,000 ft, there would be little, if any, injury or clinical effects, but exposures would exceed approximately 3 rads and would require administrative investigation and reporting. Beyond 2,000 ft, there would be no hazard.

VII. THE CLOUD GROWTH AND ASCENT

Effluent clouds from instantaneous reactor disasters have been a subject of some speculation because their behavior is an important factor in reactor siting and hazard evaluations. Cloud behavior is not well understood and, since Kiwi-TNT afforded an opportunity to observe an effluent cloud from a simulated uncontained reactor disaster, efforts were made to document it to the fullest practicable extent. This chapter discusses the visually recorded behavior of the effluent cloud; radiological effects are discussed later.

Continuous photographic sequences of the cloud were taken from five locations around the test point from the instant of the excursion until the cloud was out of photographic view, approximately 10 minutes later. The Appendix contains the tabulated data obtained from these photographs and discusses the methods of analysis. This material is available in no other publication.

Figure 32 shows the cloud rise, plotted linearly as mean altitude vs. distance. Figure 33 shows logarithmic plots of cloud mean altitude and top altitude vs. time. Figure 34 logarithmically depicts cloud vertical and horizontal diameter.

Figures 32 and 33 indicate that the cloud rose rapidly for about 3 minutes to a mean altitude of about 2,500 ft, presumably under the influence of the thermal disequilibrium between it and the surrounding atmosphere. It then apparently stabilized; the mean and top altitudes continued to increase, although much more slowly, while the bottom altitude remained essentially constant. The continued increase in cloud size after stabilization can be attributed to atmospheric dispersion, but the slow increase in altitude after stabilization is difficult to explain.

The continued increase in the top altitude led

36
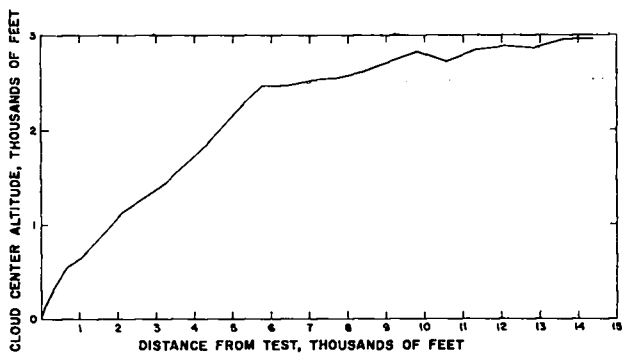
Fig. 32. Cloud center altitude vs. distance. —
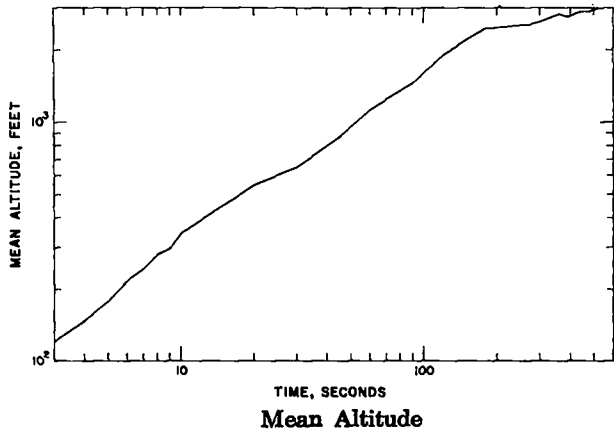
Mean Altitude
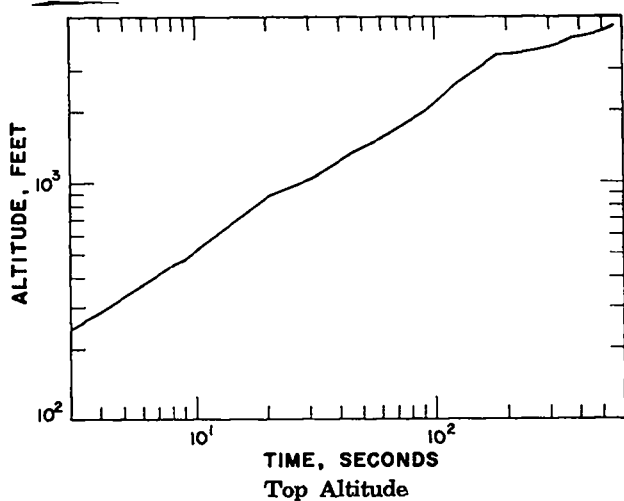
Top Altitude

Fig. 33. Cloud altitude vs. time (logarithmic plot).

to the belief, on an earlier, less thorough, examination of the data, that the cloud did not stabilize until about 10 minutes after the event. However, Figs. 32 through 34 indicate a clear change in motion very close to 3 minutes after the event, leading to the conclusion that the cloud stabilized at that time. All further discussion will assume cloud stabilization 180 seconds after the excursion.
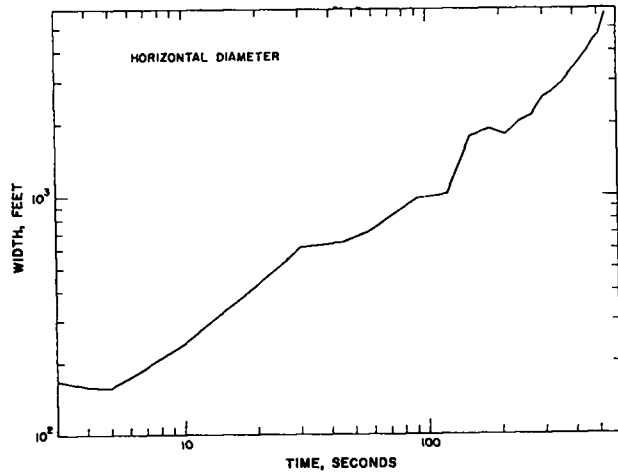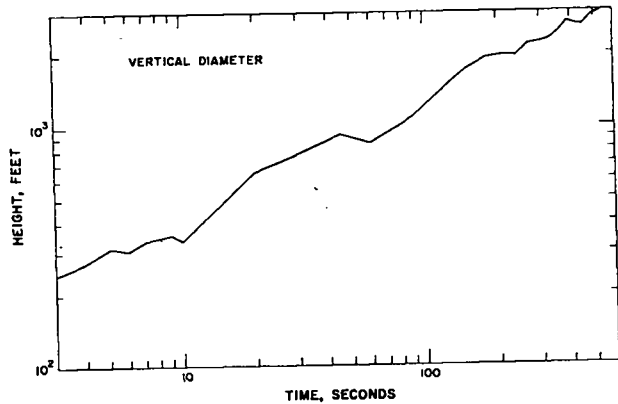
Fig. 34. Cloud diameter vs. time.

Straight lines were fitted by means of least-squares techniques to the data plotted in Figs. 33 and 34, yielding the following relationships:

For cloud mean altitude before stabilization,
$$A_m = 58.0 \; t^{0.724}. \tag{7.1}$$

For cloud mean altitude after stabilization,
$$A_m = 925 \; t^{0.186}. \tag{7.2}$$

For cloud top altitude before stabilization,
$$A_t = 118 \; t^{0.648}. \tag{7.3}$$

For cloud top altitude after stabilization,
$$A_t = 863 \; t^{0.260}. \tag{7.4}$$

For cloud vertical diameter,
$$H = 162 \; t^{0.456} \tag{7.5}$$

For cloud horizontal diameter before stabilization,
$$W = 61.6 \; t^{0.631}. \tag{7.6}$$

For cloud horizontal diameter after stabilization,
$$W = 8.94 \; t. \tag{7.7}$$

37

In these relationships, length is in feet and time is in seconds. Another relation between cloud altitude and time that can be observed from these data is

$$A = A_t (1 - e^{pt}).\qquad(7.8)$$

This relation has an advantage for some computational purposes in that it and all its derivatives are continuous, whereas there are discontinuities in the derivatives of the first set of relations. Values of A_t and p were found using least-squares curve fitting techniques, and yield the following equations,

$$A_m = 2880 (1 - e^{-0.490\ T}) + 70\qquad(7.9)$$

$$A_t = 4218 (1 - e^{-0.416\ T}) + 194\qquad(7.10)$$

where A_m and A_t are mean altitude and top altitude in feet, as before, but T is now expressed in minutes. The fit of the data to Eqs. 7.9 and 7.10 is shown in Fig. 35.

One particularly interesting aspect of cloud behavior was the correlation between the actual height of stabilization and heights of stabilization predicted by the few available models using known or assumed meteorological conditions. The first reported comparison, made without detailed examination of the actual weather parameters, but rather with assumed "usual" or "typical" values, gave a value lower than the actual cloud top altitude at 10 minutes, but very near to its mean altitude at 3 minutes. This particular example used

the Sutton model for cloud rise as discussed in "Meteorology and Atomic Energy."[14]

A more careful consideration of the three models for cloud height prediction discussed in Reference 14 reveals that all three involve the use of an actual or implied gradient of potential temperature and, if there is no gradient of potential temperature, no rise can be defined by these models. The temperature profile actually measured near the test point a few minutes after the Kiwi-TNT excursion showed a lapse rate nearly equal to the dry adiabatic lapse rate in most of the atmosphere through which the cloud rose; therefore, the potential temperature gradient in this atmosphere was very nearly zero, and calculations of cloud rise using these models were not very meaningful. (As a matter of interest, a temperature profile nearly equal to the dry adiabatic lapse rate has been frequently measured when nuclear rocket reactors have been tested.) Another difficulty would have arisen with these models even had the potential temperature gradient not been zero, in that some of the other parameters are difficult or impossible to measure, even with the extensive equipment utilized for the Kiwi-TNT experiment, and resort must be made to assumed typical values for these parameters.

Finally, these models also require a knowledge of the thermal energy contained in, and the temperature of, the embryo cloud. Both these quantities can be only crudely estimated for this experiment. An instant after the excursion, an incandescent ball appeared where the reactor
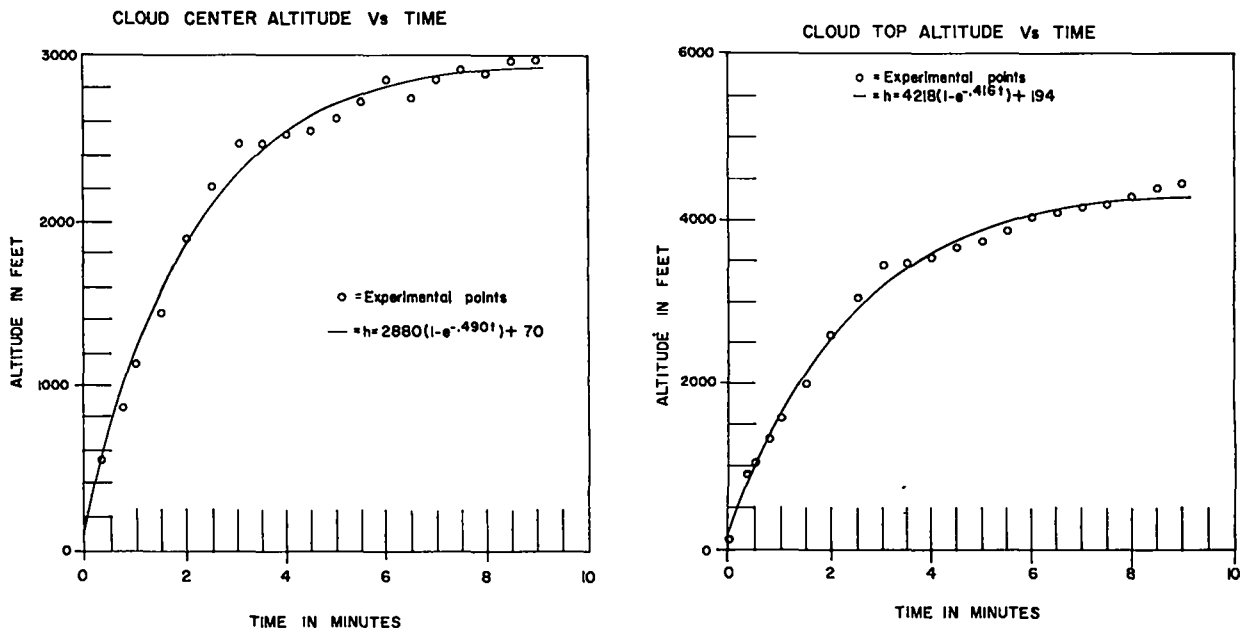

Fig. 35. Cloud altitude vs. time (least-squares plot).

stood, which rapidly cooled and developed into the cloud. The rate of heat transfer from this ball by radiation was sufficient to cool it from white incandescence, through dull red, to a black cloud, in approximately 1 second. It therefore seems appropriate to assign an initial temperature to the cloud of perhaps a few hundred degrees centigrade, since incipient red heat occurs at approximately 500 to 550°C. What constitutes a "few" in this case is subject to guesswork. The amount of energy liberated during the excursion is relatively well known, being approximately 10^4 MW-sec, 10^{10} J, 2.5×10^9 g-cal, or 10^7 Btu. Only about 1% of this was lost as kinetic energy, an inconsequential amount for purposes of this discussion. The amount of energy lost by radiation can be approximated if it is assumed that the specific heat of the incandescent ball remained essentially constant from 3,000 to 800°K, in which case approximately 70% of the energy would be lost by radiation, leaving about 3×10^9 J, 7×10^8 g-cal, or 3×10^6 Btu. Corrections could be entered for nonconstant specific heat, but, as will become apparent, other difficulties and uncertainties make such a refinement extraneous to this discussion. An additional complication is that samples of the cloud for radiochemical analysis collected a few minutes after the event by aircraft contained very little graphite.[15] This can be explained by assuming that the hot, highly fragmented graphite originally in the reactor core was oxidized during cloud development. Radiochemical analyses of

cloud samples indicate that at least half of the core was present in the cloud. (Approximately half of the unfissioned uranium, and two-thirds of the resultant fission products were calculated to have been released to the cloud.) The reactor core contained approximately 1,000 kg of graphite. This amount of graphite, if oxidized to carbon dioxide, would liberate approximately 3×10^{10} J, 7×10^9 g-cal, or 3×10^7 Btu. It is apparent that the amount of heat energy that could be liberated by oxidation of core graphite during cloud rise is appreciable — of the same magnitude as the nuclear energy released during the excursion. An estimate of the actual thermal energy, and its rate of release, is therefore very difficult to make, as is a meaningful comparison of the actual cloud rise during this experiment with predictions of rise made using any of several available models.

A rule of thumb is that the height of a reactor disaster effluent cloud may be estimated by assuming that it will rise 300 to 500 meters above the average base of fair weather cumulus clouds when a dry adiabatic lapse rate exists. This altitude would be at the base of an upper stable layer, such as occurred at approximately 9,000 feet MSL on the day of the Kiwi-TNT event. By this rule, the cloud should have risen to 6,500 to 7,000 ft above terrain. Its altitude at stabilization was substantially below this, in fact it stopped rising a few thousand feet below the base of the stable layer.

VIII. THE CLOUD WAKE

Information used in this chapter is taken from "Nevada Aerial Tracking System, Very Preliminary Report of Kiwi-TNT Event," EG&G, Inc., Santa Barbara, California,[6] and from LA-3395-MS, "Radiation Measurements of the Effluent from the Kiwi-TNT Experiment," by Henderson and Fultyn.[16]

Because the Kiwi-TNT was a unique, controlled simulation of a phenomenon frequently called a maximum credible reactor accident, there was great interest in the radiological characteristics and effects of the effluent many miles from the test point. The interest of LASL was to measure the levels of airborne radioactivity and ground deposition, to try to determine its isotopic concentration, and to relate this information to current atmospheric dispersion models to test their validity. The USPHS documented the effects of the long-range effluent cloud on the people and agriculture downwind.[5] The results of the LASL

investigation are given in this and the next chapter. The USPHS results are in Chapter X.

A general understanding of the cloud path was obtained by aerial tracking. The Nevada Aerial Tracking System (NATS) aircraft manned by personnel from EG&G observed the radioactive cloud shortly after it reached California and again as it reached the Pacific Ocean.[6]

The LASL effluent cloud sampling stations blanketed a quadrant downwind from 4,000 ft to 50 miles from the test point.[16] Portable trailer-mounted sampling equipment was used as described in Chapter II. Figure 36 shows the location of LASL sampling stations for this event. Because of the proximity of the Kiwi-TNT test point to Reactor Test Cell C at Jackass Flats, station placement was on arcs previously established for the normal reactor test point at the test cell. All results presented here use the station designations
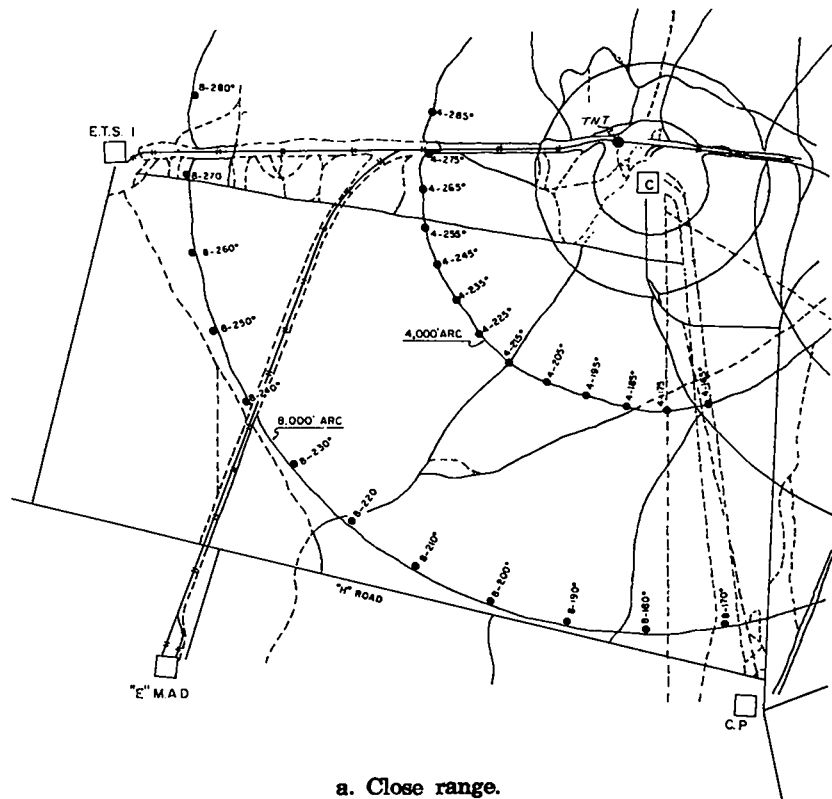
a. Close range.
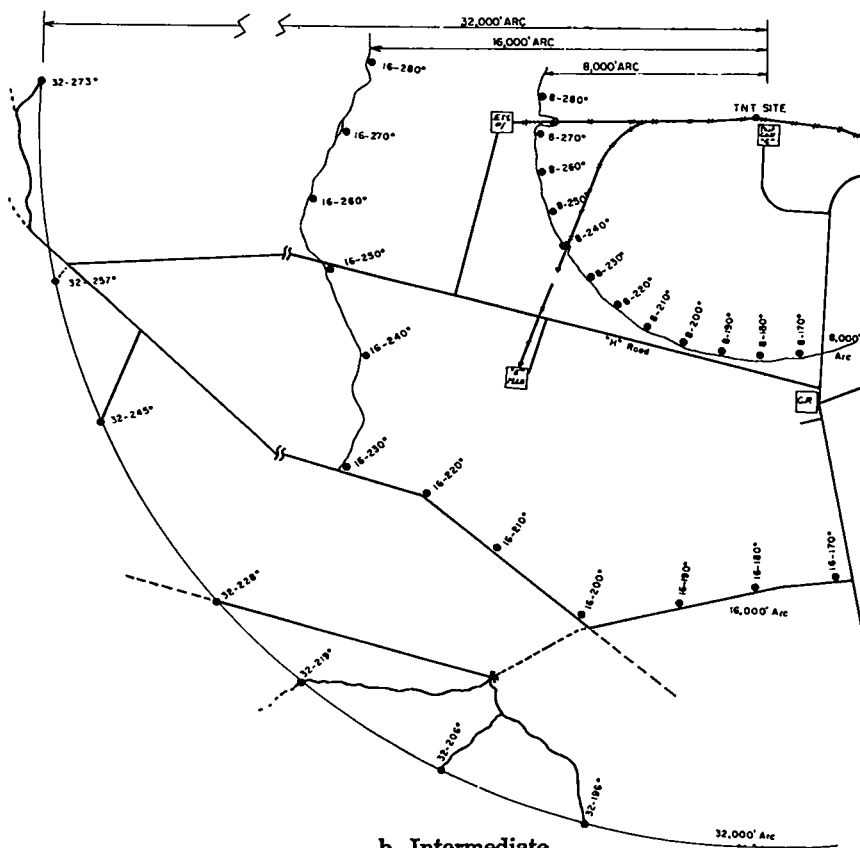
b. Intermediate.

Fig. 36. Air sampling stations.

BEATTY
128-280°
128-266°
64-268°
128-263°
64-251°
64-241°
64-230°
128-250°
64-221°
64-215°
64-203°
64-186°
128-236°
(U S 90)
LATHROP
WELLS
12 Mile
Arc
T.N.T. SITE
264-253°
264-246°
128-225°
NEVADA
CALIFORNIA
264-236°
128-211°
128-200°
128-190°
24 Mile
Arc
FURNACE
CREEK
D E A T H   V A L L E Y
264-240°
264-225°
DEATH VALLEY
JUNCTION
264-210° A
264-217°
DANTE'S
VIEW
264-200°
264-190°
50 Mile
Arc
264-210° B
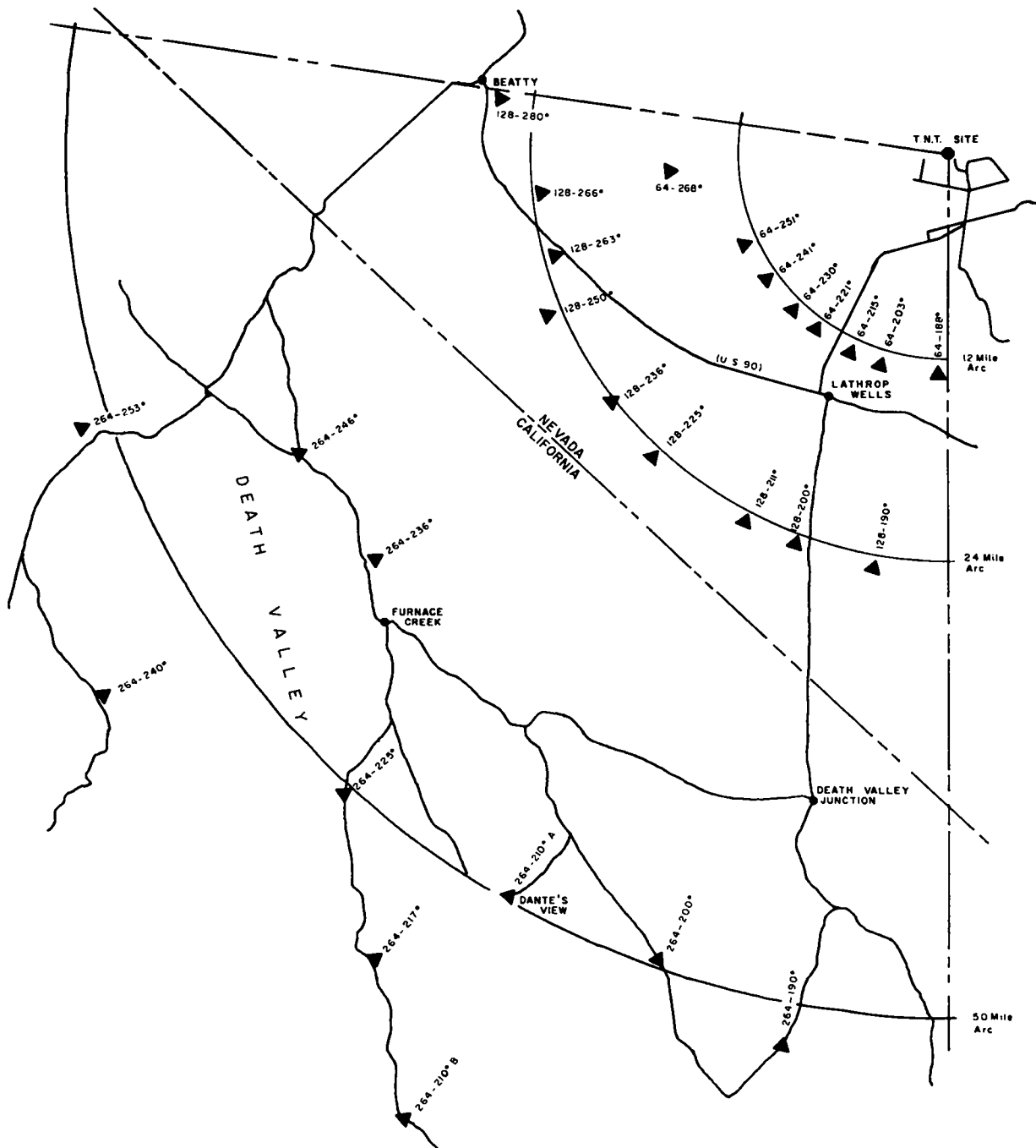
c. Long range.

Fig. 36. Continued.

of these areas. Because these previously established arcs were not exactly concentric with the Kiwi-TNT test point, Table X is provided to show the true azimuth and distance from the test point for each station on the 4,000-, 8,000-, and 16,000-ft arcs.

The Staplex* high-volume air samplers were

each fitted with a transition piece to accommodate a 6 × 9-in. Whatman No. 41 filter paper. This particulate filter was backed up by a parallel pair of organic vapor type respirator cartridges packed with activated charcoal, which allowed for the gross separation of the airborne material into two distinct fractions. The material collected on the

*The Staplex Co., New York, N. Y.

41

TABLE X. SAMPLER LOCATIONS*

Test Cell C Location	TNT Location Distance (ft)	Azimuth[a] (°)	Test Cell C Location	TNT Location Distance (ft)	Azimuth[a] (°)
4,000-ft arc			**8,000-ft arc (continued)**		
4-180	4,540	176	8-205	8,370	202
4-185	4,520	181	8-210	8,330	207
4-190	4,490	186	8-215	8,290	212
4-195	4,460	190	8-220	8,240	216
4-200	4,420	194	8-225	8,200	222
4-205	4,390	199	8-230	8,150	226
4-210	4,350	203	8-235	8,100	231
4-215	4,310	208	8-240	8,040	236
4-220	4,260	212	8-245	7,980	241
4-225	4,220	217	8-250	7,940	246
4-230	4,170	222	8-255	7,890	251
4-235	4,120	226	8-260	7,840	256
4-240	4,060	231	8-265	7,790	261
4-245	4,010	236	8-270	7,740	266
4-250	3,960	241			
4-255	3,910	246	**16,000-ft arc**		
4-260	3,860	251	16-180	16,500	179
4-265	3,800	256	16-190	17,800	188
4-270	3,760	262	16-200	18,800	198
			16-210	18,000	209
8,000-ft arc			16-220	17,700	219
8-180	8,530	178	16-230	19,100	228
8-185	8,510	183	16-240	16,000	237
8-190	8,480	188	16-252	15,900	249
8-195	8,450	192	16-261	16,800	258
8-200	8,410	198	16-270	14,400	267

(a) North = 0.

*The Kiwi-TNT test point was N 28° W at 600 ft from Test Cell C. The locations of the stations at 32,000 ft and beyond are not known precisely enough to make calculations of exact position in relation to the test point worthwhile.

filter was assumed to be entirely particulate, and that on the charcoal was assumed to be entirely gaseous at the time of collection. (These assumptions, as well as the assumption that noble gases would not be collected on either medium, are not entirely true, but departures from them are mostly small, although at times troublesome and not entirely resolvable.) The nominal sampling rate of this system is 1 meter^3 of air per minute.

The cascade impactors were of the Unico* design, selected on the basis of previous field experience with several designs. Nondrying resin-coated plastic slides were used for the four impaction stages and a membrane filter was placed after the fourth stage as a fifth and final collector. The units were used to measure the radioactivity associated with particles of sizes characterized by their effective aerodynamic diameters.

The sequential samplers consisted of eight Staplex sampler heads, each fitted with a 4-in.-diameter Whatman No. 41 filter paper. The sampling sequence was initiated by radio command, but was manually preset to sample during the total estimated time of cloud passage. Running times per sampler varied from 5 minutes on the close-range arcs to 30 minutes on the distant arcs. Although the samplers were intended to collect information regarding cloud arrival time and longitudinal concentration profile with respect to time, the sequencing mechanisms did not all function properly and meaningful samples were not collected. Because analysis of the data revealed them to be clearly absurd (several stations indicated that the cloud passed before the excursion), they are not presented here.

Samples of deposited activity were collected on paired 7 × 10-$\frac{1}{2}$-in. Lucite trays coated with a clear, nondrying alkyd resin. The trays were placed horizontally, face up, on stakes approximately 30 in. above grade at all trailer locations. Acrylic plastic trays were used to avoid the trouble previously encountered with neutron activation of metallic trays and to permit microscopic examination of the collected material.

Film packets of the type described in Chapter VI were also placed at each trailer location on the stake supporting the resin-coated trays. The methods employed and results obtained from this placement are given in Chapter VI.

The radioactivity associated with each high-volume air sample and resin-coated tray was de-

termined using simultaneous beta-gamma detectors housed in a common shield. Beta counting was done using one of several 7 × 10-$\frac{1}{2}$-in. methane gas flow proportional counters, each located at the top of its iron counting shield. The gamma counting probes consisted of a 10-in. diameter by 5-in.-thick plastic phosphor coupled to five photomultiplier tubes. The gamma probe output was fed into a standard single-channel analyzer operated in the integral mode with the threshold set at approximately 100 keV. The mechanical arrangement of the components allows for variation of counting geometries inside the shield. Specially designed beta proportional counters were used to count the cascade impactor stages and sequential samples. Quantitative isotopic information about selected samples was derived by use of multichannel gamma pulse height analysis, discussed in the next chapter.

Table XI shows the total dosages (μCi-sec/m^3) and deposition concentrations (μCi/m^2) with the activity corrected to estimated time of cloud passage. Airborne particle dosages were calculated from data generated by the analysis of filter papers, and the airborne gaseous dosages from analysis of the charcoal cartridges. The deposited activity per unit area was determined by assuming that the ground deposition was the same in composition and magnitude as that collected on the resin-coated trays. Extrapolations of radioactivity with respect to time were performed using the isotopic compositions of samples presented in the next chapter.

Table XII shows measured deposition velocities at the stations where there was significant sample activity. Values for airborne particulate material were obtained by dividing the deposition concentration measured by the resin-coated tray (Ci/m^2) by the airborne particle dosage measured by the filter paper only (Ci-sec/m^3). Values for total airborne material were obtained by dividing tray activity by total airborne dosage (filter plus cartridge dosage). These values are questionable because the isotopic composition of the deposited activity is different from that of the airborne activity. The large variations in deposition velocity from station to station are not unusual, however, as this phenomenon is also noted in data for all the normal reactor runs. This suggests that the concept of a constant deposition velocity is grossly in error, and that the "constant" should be replaced by a statistically varying quantity.

Table XIII shows the results of the analysis of samples collected by the cascade impactors. These results were derived using the activity on

TABLE XI. MEASURED DOSAGES AND DEPOSITION CONCENTRATIONS

Station	Dosage (μCi-sec/m^3) Airborne Particulate	Dosage (μCi-sec/m^3) Airborne Gaseous	Total	Ground Deposition (μCi/m^2)
		4,000-ft arc		
4-180	1.4×10^{-1}	Bkgd	1.4×10^{-1}	2.3×10^{-2}
4-185	1.6×10^{0}	1.1×10^{0}	2.7×10^{0}	1.5×10^{-2}
4-190	1.6×10^{1}	8.2×10^{0}	2.4×10^{1}	1.6×10^{-2}
4-195	7.1×10^{1}	1.1×10^{1}	8.1×10^{1}	4.9×10^{-2}
4-200	3.2×10^{2}	3.2×10^{1}	3.5×10^{2}	2.5×10^{-1}
4-205	1.0×10^{1}	1.1×10^{0}	1.1×10^{1}	1.8×10^{0}
4-210	6.0×10^{3}	4.3×10^{2}	6.4×10^{3}	7.8×10^{0}
4-215	3.1×10^{4}	1.4×10^{3}	3.2×10^{4}	6.6×10^{2}
4-220	1.2×10^{3}	3.1×10^{1}	1.2×10^{3}	3.4×10^{1}
4-225	2.2×10^{4}	2.0×10^{3}	2.4×10^{4}	9.3×10^{0}
4-230	1.4×10^{4}	1.6×10^{3}	1.6×10^{4}	2.8×10^{0}
4-235	8.3×10^{3}	1.1×10^{3}	9.4×10^{3}	5.2×10^{0}
4-240	4.8×10^{3}	5.0×10^{2}	5.3×10^{3}	4.4×10^{0}
4-245	4.6×10^{3}	4.6×10^{2}	5.0×10^{3}	1.3×10^{0}
4-250	1.9×10^{2}	7.8×10^{0}	2.0×10^{2}	5.6×10^{-1}
4-255	6.8×10^{1}	4.4×10^{0}	7.2×10^{1}	1.6×10^{-1}
4-260	7.1×10^{1}	2.8×10^{-1}	7.1×10^{1}	4.8×10^{-2}
4-265	8.7×10^{0}	1.1×10^{0}	9.8×10^{0}	1.1×10^{-2}
4-270	1.0×10^{1}	3.7×10^{0}	1.4×10^{1}	7.2×10^{-3}
		8,000-ft arc		
8-180	2.6×10^{-1}	5.3×10^{0}	5.5×10^{0}	Bkgd
8-185	3.6×10^{-1}	8.1×10^{-1}	1.2×10^{0}	Bkgd
8-190	1.6×10^{0}	9.0×10^{-1}	2.5×10^{0}	Bkgd
8-195	1.1×10^{1}	1.8×10^{1}	2.9×10^{1}	1.0×10^{-2}
8-200	1.6×10^{1}	2.7×10^{1}	4.3×10^{1}	1.9×10^{-2}
8-205	2.0×10^{2}	5.2×10^{1}	2.5×10^{2}	1.0×10^{-1}
8-210	4.5×10^{3}	5.3×10^{2}	5.1×10^{3}	2.0×10^{0}
8-215	1.5×10^{4}	1.7×10^{3}	1.7×10^{4}	2.1×10^{1}
8-220	9.3×10^{3}	2.1×10^{3}	1.1×10^{4}	3.1×10^{0}
8-225	4.2×10^{3}	7.2×10^{2}	4.9×10^{3}	8.7×10^{-1}
8-230	1.6×10^{1}	4.5×10^{0}	2.0×10^{1}	8.2×10^{-1}
8-235	2.3×10^{1}	5.2×10^{0}	2.8×10^{1}	1.4×10^{0}
8-240	5.6×10^{2}	1.4×10^{2}	7.0×10^{2}	2.2×10^{-1}
8-245	1.8×10^{1}	7.4×10^{0}	2.6×10^{1}	9.6×10^{-3}
8-250	4.2×10^{0}	1.8×10^{-2}	4.2×10^{0}	9.7×10^{-3}
8-255	6.7×10^{1}	9.1×10^{0}	7.6×10^{1}	Bkgd
8-260	1.7×10^{-1}	7.1×10^{-1}	8.8×10^{-1}	Bkgd
8-265	3.9×10^{-1}	4.6×10^{-1}	8.5×10^{-1}	1.0×10^{-3}
8-270	3.8×10^{0}	1.4×10^{-1}	3.9×10^{0}	7.9×10^{-3}
		16,000-ft arc		
16-180	3.0×10^{-1}	2.1×10^{0}	2.4×10^{0}	9.6×10^{-4}
16-190	1.8×10^{-1}	8.5×10^{-2}	2.7×10^{-1}	6.9×10^{-3}
16-200	2.1×10^{0}	1.6×10^{0}	3.7×10^{0}	8.5×10^{-3}
16-210	6.7×10^{3}	2.0×10^{2}	6.9×10^{3}	4.6×10^{2}
16-220	1.6×10^{3}	1.9×10^{2}	1.8×10^{3}	4.7×10^{-1}
16-230	8.3×10^{2}	1.6×10^{2}	9.8×10^{2}	2.0×10^{-1}

TABLE XI. CONTINUED

Station	Dosage (μCi-sec/m^3) Airborne Particulate	Airborne Gaseous	Total	Ground Deposition (μCi/m^2)
16-240	2.9×10^2	7.6×10^1	3.6×10^2	6.2×10^{-2}
16-252	4.8×10^{-1}	2.7×10^0	3.1×10^0	5.0×10^{-2}
16-261	2.2×10^{-1}	1.5×10^{-1}	3.7×10^{-1}	4.3×10^{-5}
16-270	7.4×10^{-1}	5.5×10^{-1}	1.3×10^0	1.1×10^{-2}

32,000-ft arc

Station	Airborne Particulate	Airborne Gaseous	Total	Ground Deposition
32-194	1.8×10^0	8.4×10^{-1}	2.7×10^0	1.3×10^{-1}
32-206	1.1×10^0	9.0×10^{-1}	2.0×10^0	6.9×10^0
32-219	1.8×10^4	6.9×10^2	1.9×10^4	2.8×10^1
32-228	5.5×10^2	7.2×10^1	6.2×10^2	2.5×10^{-1}
32-245	2.2×10^1	6.6×10^0	2.8×10^1	2.0×10^{-1}
32-258	2.8×10^{-1}	Bkgd	2.8×10^{-1}	3.5×10^{-2}
32-273	2.0×10^0	8.1×10^{-1}	2.8×10^0	1.2×10^{-2}

64,000-ft arc

Station	Airborne Particulate	Airborne Gaseous	Total	Ground Deposition
64-172	Bkgd	7.3×10^{-2}	7.3×10^{-2}	Bkgd
64-188	Bkgd	1.5×10^{-1}	1.5×10^{-1}	Bkgd
64-203	Bkgd	6.4×10^{-1}	6.4×10^{-1}	2.3×10^{-2}
64-211	8.7×10^2	2.7×10^1	9.0×10^2	Bkgd
64-215	6.2×10^3	2.5×10^2	6.4×10^3	3.7×10^0
64-221	1.1×10^2	3.7×10^0	1.2×10^2	1.9×10^1
64-230	1.1×10^{-1}	3.1×10^{-1}	4.2×10^{-1}	6.5×10^{-3}
64-241	Bkgd	1.0×10^0	1.0×10^0	1.1×10^{-1}
64-251	Bkgd	1.6×10^0	1.6×10^0	Bkgd

128,000-ft arc

Station	Airborne Particulate	Airborne Gaseous	Total	Ground Deposition
128-180	2.1×10^{-1}	3.3×10^{-1}	5.3×10^{-1}	Bkgd
128-190	7.4×10^{-2}	1.5×10^{-1}	2.3×10^{-1}	4.0×10^{-3}
128-200	2.4×10^1	1.4×10^0	2.5×10^1	4.8×10^{-1}
128-211	1.7×10^3	5.2×10^1	1.7×10^3	2.4×10^0
128-225	1.0×10^2	2.5×10^0	1.1×10^2	3.7×10^{-2}
128-236	4.6×10^{-1}	2.3×10^{-2}	4.8×10^{-1}	Bkgd
128-250	5.6×10^{-1}	1.5×10^{-1}	7.1×10^{-1}	4.2×10^{-1}
128-263	2.1×10^{-1}	2.2×10^{-1}	4.3×10^{-1}	Bkgd
128-266	1.5×10^{-1}	2.4×10^{-1}	4.0×10^{-1}	Bkgd
128-280	2.0×10^{-1}	2.1×10^{-1}	4.1×10^{-1}	Bkgd

256,000-ft arc

Station	Airborne Particulate	Airborne Gaseous	Total	Ground Deposition
256-183	Bkgd	Bkgd	Bkgd	4.3×10^{-3}
256-190	4.8×10^2	1.6×10^1	4.9×10^2	5.1×10^{-1}
256-200	7.4×10^2	2.4×10^1	7.6×10^2	3.8×10^{-1}
256-210	1.7×10^2	6.7×10^0	1.8×10^2	Bkgd
256-217	1.8×10^{-1}	9.9×10^{-2}	2.8×10^{-1}	5.2×10^{-4}
256-225	1.2×10^{-1}	Bkgd	1.2×10^{-1}	Bkgd
256-236	2.3×10^{-1}	Bkgd	2.3×10^{-1}	Bkgd
256-240	2.2×10^{-1}	Bkgd	2.2×10^{-1}	Bkgd

TABLE XII. DEPOSITION VELOCITIES IN CENTIMETERS PER SECOND

Station	Total Airborne Material (gaseous + particulate)	Particulate Material	Station	Total Airborne Material (gaseous + particulate)	Particulate Material
	4,000-ft arc			**16,000-ft arc**	
4-180	16.	16	16-180	0.040	0.32
4-185	0.56	0.94	16-190	2.6	3.8
4-190	0.067	0.10	16-200	0.23	0.40
4-195	0.060	0.069	16-210	6.7	6.9
4-200	0.071	0.078	16-220	0.026	0.029
4-205	16.	18.	16-230	0.020	0.024
4-210	0.12	0.13	16-240	0.017	0.021
4-215	2.1	2.1	16-252	1.6	10.
4-220	2.8	2.8	16-261	0.012	0.020
4-225	0.039	0.042	16-270	0.85	1.5
4-230	0.018	0.020			
4-235	0.055	0.063		**32,000-ft arc**	
4-240	0.083	0.092			
4-245	0.026	0.028	32-194	4.8	7.2
4-250	0.28	0.29	32-206	350.	630.
4-255	0.22	0.24	32-219	0.15	0.16
4-260	0.068	0.068	32-228	0.040	0.045
4-265	0.11	0.13	32-245	0.71	0.91
4-270	0.051	0.072	32-258	13.	13.
			32-273	0.43	0.60
	8,000-ft arc				
				64,000-ft arc	
8-195	0.034	0.091			
8-200	0.044	0.12	64-203	3.6	—
8-205	0.040	0.050	64-211	—	—
8-210	0.039	0.044	64-215	0.058	0.060
8-215	0.12	0.14	64-221	16.	17.
8-220	0.028	0.033	64-230	1.5	5.9
8-225	0.018	0.021	64-241	11.	—
8-230	4.1	5.1			
8-235	5.0	6.1		**128,000-ft arc**	
8-240	0.031	0.039			
8-245	0.037	0.053	128-190	1.7	5.4
8-250	0.23	0.23	128-200	1.9	2.0
8-255	—	—	128-211	0.14	0.14
8-260	—	—	128-225	0.034	0.037
8-265	0.12	0.26	128-236	—	—
8-270	0.20	0.21	128-250	59.	75.
				256,000-ft arc	
			256-190	0.10	0.11
			256-200	0.05	0.051
			256-210	—	—
			256-217	0.19	0.29

TABLE XIII. AIRBORNE PARTICLE SIZE DATA, ACTIVITY ON UNICO IMPACTOR STAGES AT COUNT TIME (PICOCURIES)

Station	Stage 1	Stage 2	Stage 3	Stage 4	Stage 5	Median Diameter (μ)	Geometric Standard Deviation	Comments
				4,000-ft arc				
4-210	568	695	125	530	23,307			92% <1μ
4-215	134,172	200,034	14,537	114,340	126,641	3.8	5.4	
4-220	11,941	6,281	246	5,366	263			66% >5μ
4-225	1,286	2,851	329	2,972	47,641			86% <1μ
4-230	32,555	994	2,479	713	33,433			
4-235	6,424	3,051	1,577	6,040	85,704			84% <1μ
4-240	1,731	783	392	1,222	18,880			82% <1μ
4-245	1,585	226	299	2,649	24,069			88% <1μ
4-250	1,647	141	77	2,084	437	2.6	6.6	
				8,000-ft arc				
8-210	3,270	1,253	220	1,471	22,984			80% <1μ
8-215	17,437	2,595	797	4,988	131,182			83% <1μ
8-220	3,173	2,153	275	4,965	4,726	1.6	7.2	
8-225	3,028	568	332	1,102	37,703			88% <1μ
				16,000-ft arc				
16-210	27,978	1,306	193	9,988	0			95% >5μ
16-220	114	13	15	23	6			72% >5μ
16-230	107	48	37	145	2,417			89% <1μ
16-240	125	21	34	169	1,900			87% <1μ
				32,000-ft arc				
32-219	161,930	8,230	53,915	23,940	23,892			62% >5μ
				64,000-ft arc				
64-211	119	16	148	120	2,236			81% <1μ
64-215	353	7,730	694	1,515	31,910			69% <1μ
64-221	8,018	765	316	914	11			84% >5μ
				128,000-ft arc				
128-211	81	262	64	219	7,515			91% <1μ
				256,000-ft arc				
256-190	886	6,277	16	262	1,650	4.8	3.6	55% <1μ
256-200	1,897	536	271	1,413	4,191	4.8	3.6	55% <1μ

the impactor stages at the time the samples were counted, and a calibration of a typical impactor for particles with a specific gravity of 2.6. The stages of a single unit were counted sequentially within 10 minutes of each other; corrections for decay within this period were negligible. These data allow one to approximate the aerodynamic size characteristics of the airborne particulate material. In general, the isotopic composition of the material on the early stages (when sufficient activity was available to analyze) was similar to that found on the resin-coated trays, while the composition of the activity on the final stages approximated that collected on the high-volume filter papers.

Table XIV shows the results of calculations based on the analysis of the air samples collected during the experiment. It gives for each sample station the hypothetical whole-body gamma dose from the radioactive cloud. This dose is calculated assuming that the station was immersed in a hemispherical cloud of infinite extent and of uniform concentration equal to that measured at the station and extrapolated to time of cloud passage. It is also assumed that, on the average, one photon was emitted per nuclear disintegration, with average photon energy of 0.7 MeV. It is recognized that the validity of the assumption of an infinite hemispherical cloud is poor for stations within a few miles of the test point; validity should improve as the distance increases but the assumption is still dubious even at long distances. However, in spite of its shortcomings, this assumption is frequently made in deriving doses from radioactive clouds for hazards evaluations and other arguments. Although sufficiently sensitive dosimetric equipment for accurate measurement of cloud dose was not available at any of the trailer locations, these calculations give some estimate of the hazard that might have been encountered. For the few locations where direct comparison of these hypothetical doses with measured doses can be made, discrepancies must be attributed to the dubious validity of the premises of the calculation, or dosimetric errors, or both.

Table XIV also lists a hypothetical adult thyroid dose due to iodine inhalation at each sampling station. These data arise from the actual iodine isotope dosages measured at each station by the air sampling equipment. The factors at the right for exposure to 1 Ci-sec/m³ of a particular iodine isotope were used to calculate the thyroid dose. These dose factors have been derived using National Council for Radiation Protection criteria for organ size, breathing rate, and fraction of isotope retained.

Table XV presents some hypothetical results of calculations based on the analysis of the resin-coated trays. The hypothetical ground deposition dose rate was calculated by assuming that the station was located above an infinite plane with uniform deposition of material of the same concentration as that measured on the resin-coated tray extrapolated to the time of cloud passage; that, on the average, one photon was emitted per nuclear disintegration; and that the average photon energy was 0.7 MeV. The 1-year integrated deposition dose was calculated assuming a clean area before the arrival of the cloud and no subsequent contamination. The integration was performed using only the decay of the isotopes identified as being present. One year was selected for the integration to attempt to account for leaching and other removal processes.

Figures 37 through 39 show isodosage and isoconcentration contours plotted from the measurements discussed above. Figures 40 through 46 show crosswind (azimuthal) profiles of exposure dosage, ground deposition, and deposition velocities. Figure 47 shows the cloud centerline (maximum) dosage, deposition concentrations, and deposition velocities measured on each arc vs. distance. Figures 48 through 50 show cloud centerline calculations of whole-body dose, adult thyroid inhalation dose, and deposition dose rate, from Tables XIV and XV.

The "notch," or relative minimum, at 16,000 ft in the plot of cloud centerline dosage vs. distance (Fig. 47) is typical of concentration data from normal, nondestructive reactor runs. Several speculations as to its cause are available, but it has not been soundly explained. One of the first things that comes to mind is that the concentrations at long distances (6 miles and beyond) are due to the material in the elevated cloud, while the concentrations at close range are due to material in the stem, which behaved as a theoretical ground-level release. Figure 47 implies that the stem contained about 10% as much activity as the elevated source, if both are considered to be point sources.

Isotope	Thyroid Dose in Rads Due to 1 Ci-sec/m³ of Isotope
¹³¹I	329
¹³²I	12.4
¹³³I	92.3
¹³⁴I	5.6
¹³⁵I	25.3

48

TABLE XIV. CLOUD PASSAGE EFFECTS

Station	Whole-Body Dose due to Cloud Passage (rads)	Adult Inhalation Thyroid Dose (rads)
4,000-ft arc		
4-180	3.16×10^{-8}	4.03×10^{-8}
4-185	5.68×10^{-7}	1.89×10^{-5}
4-190	4.90×10^{-6}	1.36×10^{-4}
4-195	1.71×10^{-5}	1.89×10^{-4}
4-200	7.77×10^{-5}	5.99×10^{-4}
4-205	2.02×10^{-6}	2.06×10^{-5}
4-210	1.22×10^{-3}	8.41×10^{-3}
4-215	8.25×10^{-3}	3.31×10^{-2}
4-220	2.26×10^{-4}	7.78×10^{-4}
4-225	5.42×10^{-3}	3.89×10^{-2}
4-230	3.26×10^{-3}	2.88×10^{-2}
4-235	1.91×10^{-3}	1.92×10^{-2}
4-240	1.09×10^{-3}	9.26×10^{-3}
4-245	9.13×10^{-4}	8.43×10^{-3}
4-250	4.33×10^{-5}	1.78×10^{-4}
4-255	1.66×10^{-5}	9.10×10^{-5}
4-260	1.53×10^{-5}	2.39×10^{-5}
4-265	2.16×10^{-6}	2.07×10^{-5}
4-270	2.86×10^{-6}	6.16×10^{-5}
8,000-ft arc		
8-180	9.96×10^{-7}	5.49×10^{-5}
8-185	2.29×10^{-7}	8.57×10^{-6}
8-190	5.14×10^{-7}	9.82×10^{-6}
8-195	5.50×10^{-6}	1.88×10^{-4}
8-200	8.28×10^{-6}	2.90×10^{-4}
8-205	4.89×10^{-5}	6.02×10^{-4}
8-210	9.51×10^{-4}	6.88×10^{-3}
8-215	3.44×10^{-3}	2.17×10^{-2}
8-220	2.30×10^{-3}	2.50×10^{-2}
8-225	9.15×10^{-4}	8.61×10^{-3}
8-230	4.26×10^{-6}	5.22×10^{-5}
8-235	5.73×10^{-6}	6.08×10^{-5}
8-240	1.36×10^{-4}	1.62×10^{-3}
8-245	5.63×10^{-6}	8.34×10^{-5}
8-250	8.93×10^{-7}	1.45×10^{-6}
8-255	1.70×10^{-5}	1.16×10^{-4}
8-260	1.64×10^{-7}	7.42×10^{-6}
8-265	1.74×10^{-7}	4.95×10^{-6}
8-270	8.74×10^{-7}	2.70×10^{-6}
16,000-ft arc		
16-180	4.40×10^{-7}	2.57×10^{-5}
16-190	5.73×10^{-8}	1.11×10^{-6}
16-200	7.64×10^{-7}	2.01×10^{-5}
16-210	1.27×10^{-3}	4.55×10^{-3}
16-220	3.26×10^{-4}	2.78×10^{-3}
16,000-ft arc (continued)		
16-230	1.70×10^{-4}	2.14×10^{-3}
16-240	7.93×10^{-5}	1.04×10^{-3}
16-252	5.79×10^{-7}	3.26×10^{-5}
16-261	7.84×10^{-8}	1.91×10^{-6}
16-270	2.63×10^{-7}	6.95×10^{-6}
32,000-ft arc		
32-194	4.80×10^{-7}	1.13×10^{-5}
32-206	3.59×10^{-7}	1.17×10^{-5}
32-219	3.79×10^{-3}	1.72×10^{-2}
32-228	1.06×10^{-4}	1.12×10^{-3}
32-245	5.07×10^{-6}	9.11×10^{-5}
32-258	4.96×10^{-8}	1.14×10^{-7}
32-273	4.93×10^{-7}	1.09×10^{-5}
64,000-ft arc		
64-172	1.29×10^{-8}	9.85×10^{-7}
64-188	2.63×10^{-8}	2.01×10^{-6}
64-203	1.14×10^{-7}	8.70×10^{-6}
64-211	1.34×10^{-4}	8.47×10^{-4}
64-215	1.11×10^{-3}	7.24×10^{-3}
64-221	1.82×10^{-5}	1.14×10^{-4}
64-230	7.24×10^{-8}	4.25×10^{-6}
64-241	1.81×10^{-7}	1.39×10^{-5}
64-251	2.92×10^{-7}	2.23×10^{-5}
128,000-ft arc		
128-180	8.58×10^{-8}	5.24×10^{-6}
128-190	3.70×10^{-8}	2.43×10^{-6}
128-200	3.55×10^{-6}	4.48×10^{-5}
128-211	2.39×10^{-4}	2.38×10^{-3}
128-225	1.45×10^{-5}	1.36×10^{-4}
128-236	6.68×10^{-8}	7.93×10^{-7}
128-250	1.03×10^{-7}	2.81×10^{-6}
128-263	6.79×10^{-8}	3.63×10^{-6}
128-266	6.38×10^{-8}	3.92×10^{-6}
128-280	6.48×10^{-8}	3.50×10^{-6}
256,000-ft arc		
256-190	6.08×10^{-5}	1.19×10^{-3}
256-200	9.40×10^{-5}	1.84×10^{-3}
256-210	2.20×10^{-5}	4.47×10^{-4}
256-217	3.96×10^{-8}	2.32×10^{-6}
256-225	1.51×10^{-8}	2.27×10^{-7}
256-236	2.86×10^{-8}	4.32×10^{-7}
256-240	2.63×10^{-8}	3.97×10^{-7}

TABLE XV. HYPOTHETICAL GROUND DEPOSITION EFFECTS

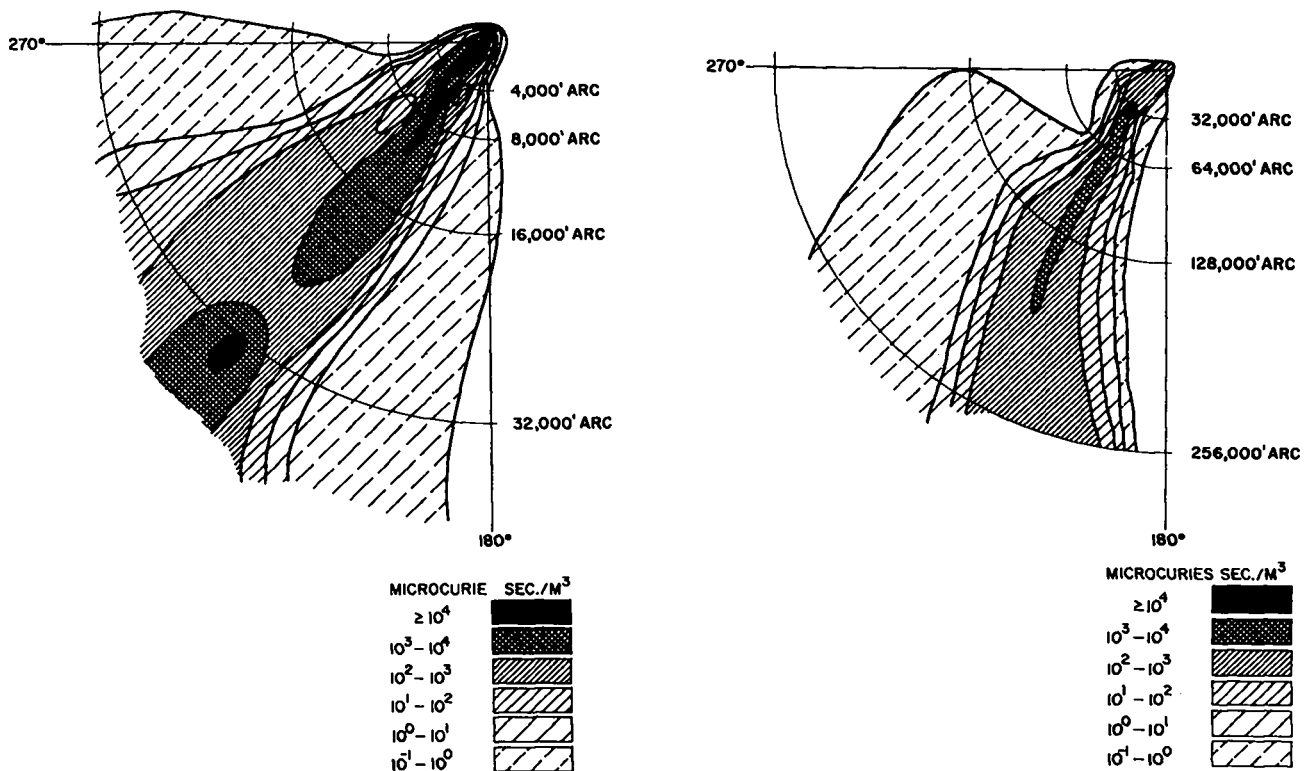| Station	Deposition Dose Rate (rads)	1-Year Integrated Deposition Dose (rads)	Station	Deposition Dose Rate (rads)	1-Year Integrated Deposition Dose (rads)
	4,000-ft arc			**16,000-ft arc (continued)**	
4-180	2.85×10^{-7}	6.96×10^{-6}	16-210	5.71×10^{-3}	1.40×10^{-1}
4-185	1.91×10^{-7}	4.66×10^{-6}	16-220	8.85×10^{-6}	1.43×10^{-4}
4-190	2.03×10^{-7}	4.95×10^{-6}	16-230	2.49×10^{-6}	6.10×10^{-5}
4-195	6.07×10^{-7}	1.48×10^{-5}	16-240	7.79×10^{-7}	1.90×10^{-5}
4-200	3.10×10^{-6}	7.56×10^{-5}	16-252	6.22×10^{-7}	1.52×10^{-5}
4-205	2.23×10^{-5}	5.44×10^{-4}	16-261	5.36×10^{-10}	1.31×10^{-8}
4-210	9.79×10^{-5}	2.39×10^{-3}	16-270	1.38×10^{-7}	3.38×10^{-6}
4-215	8.15×10^{-3}	1.99×10^{-1}			
4-220	4.26×10^{-4}	1.04×10^{-2}		**32,000-ft arc**	
4-225	1.16×10^{-4}	2.84×10^{-3}	32-194	1.68×10^{-6}	4.14×10^{-5}
4-230	3.53×10^{-5}	8.61×10^{-4}	32-206	8.56×10^{-5}	2.10×10^{-3}
4-235	6.48×10^{-5}	1.58×10^{-3}	32-219	3.55×10^{-4}	8.71×10^{-3}
4-240	5.45×10^{-5}	1.33×10^{-3}	32-228	3.08×10^{-6}	7.56×10^{-5}
4-245	1.63×10^{-5}	3.97×10^{-4}	32-245	2.52×10^{-6}	6.19×10^{-5}
4-250	6.96×10^{-6}	1.70×10^{-4}	32-258	4.35×10^{-7}	1.07×10^{-5}
4-255	2.00×10^{-6}	4.86×10^{-5}	32-273	1.54×10^{-7}	3.79×10^{-6}
4-260	5.95×10^{-7}	1.45×10^{-5}			
4-265	1.40×10^{-7}	3.42×10^{-6}		**64,000-ft arc**	
4-270	9.01×10^{-8}	2.20×10^{-6}	64-203	2.87×10^{-7}	7.12×10^{-6}
			64-211	—	—
	8,000-ft arc		64-215	4.64×10^{-5}	1.15×10^{-3}
8-195	1.28×10^{-7}	3.13×10^{-6}	64-221	2.33×10^{-4}	5.77×10^{-3}
8-200	2.42×10^{-7}	5.91×10^{-6}	64-230	8.07×10^{-8}	2.00×10^{-6}
8-205	1.27×10^{-6}	3.10×10^{-5}	64-241	1.33×10^{-6}	3.28×10^{-5}
8-210	2.57×10^{-5}	6.26×10^{-4}	64-251	—	—
8-215	2.63×10^{-4}	6.42×10^{-3}			
8-220	3.94×10^{-5}	9.61×10^{-4}		**128,000-ft arc**	
8-225	1.09×10^{-5}	2.65×10^{-4}	128-190	5.01×10^{-8}	1.26×10^{-6}
8-230	1.03×10^{-5}	2.51×10^{-4}	128-200	5.97×10^{-6}	1.50×10^{-4}
8-235	1.75×10^{-5}	4.27×10^{-4}	128-211	4.58×10^{-7}	1.15×10^{-5}
8-240	2.79×10^{-6}	6.82×10^{-5}	128-225	4.58×10^{-7}	1.15×10^{-5}
8-245	1.21×10^{-7}	2.94×10^{-6}	128-236	—	—
8-250	1.21×10^{-7}	2.95×10^{-6}	128-250	5.26×10^{-1}	1.33×10^{1}
8-255	—	—			
8-260	—	—		**256,000-ft arc**	
8-265	1.26×10^{-8}	3.06×10^{-7}	256-183	5.36×10^{-8}	1.40×10^{-6}
8-270	9.92×10^{-8}	2.42×10^{-6}	256-190	6.32×10^{-6}	1.65×10^{-4}
			256-200	4.79×10^{-6}	1.25×10^{-4}
	16,000-ft arc		256-210	—	—
16-180	1.19×10^{-8}	2.92×10^{-7}	256-217	6.50×10^{-9}	1.69×10^{-7}
16-190	8.69×10^{-8}	2.12×10^{-6}			
16-200	1.06×10^{-7}	2.59×10^{-6}			

Fig. 37. Dosage from airborne particulate activity. Beta activity corrected to estimated time of cloud passage.
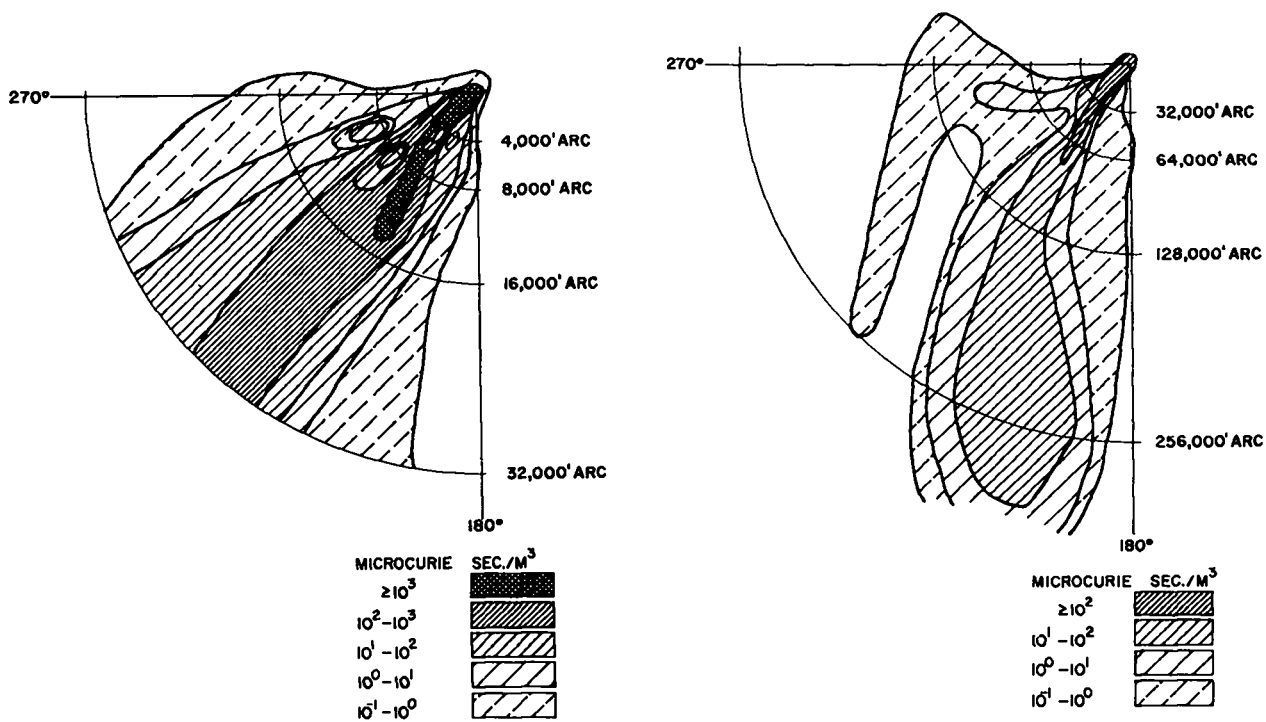

Fig. 38. Dosage from airborne gaseous activity. Gamma activity corrected to estimated time of cloud passage.
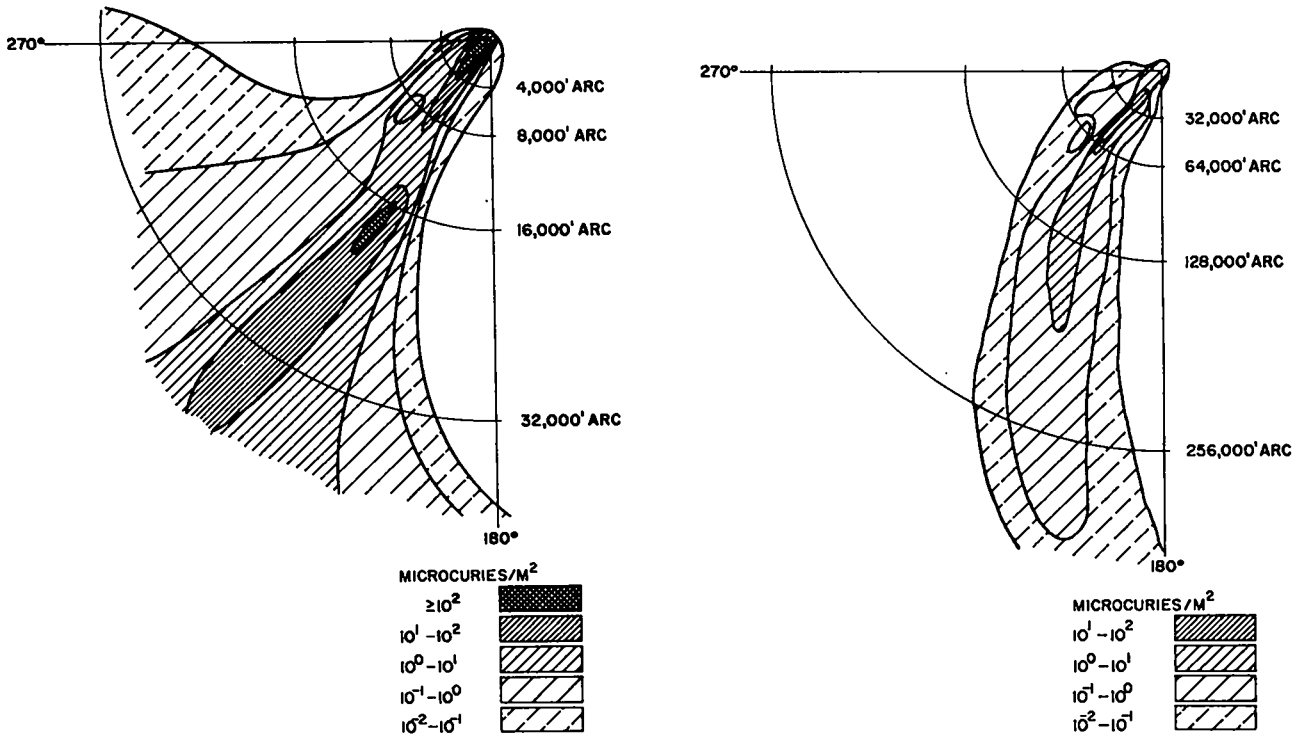
51

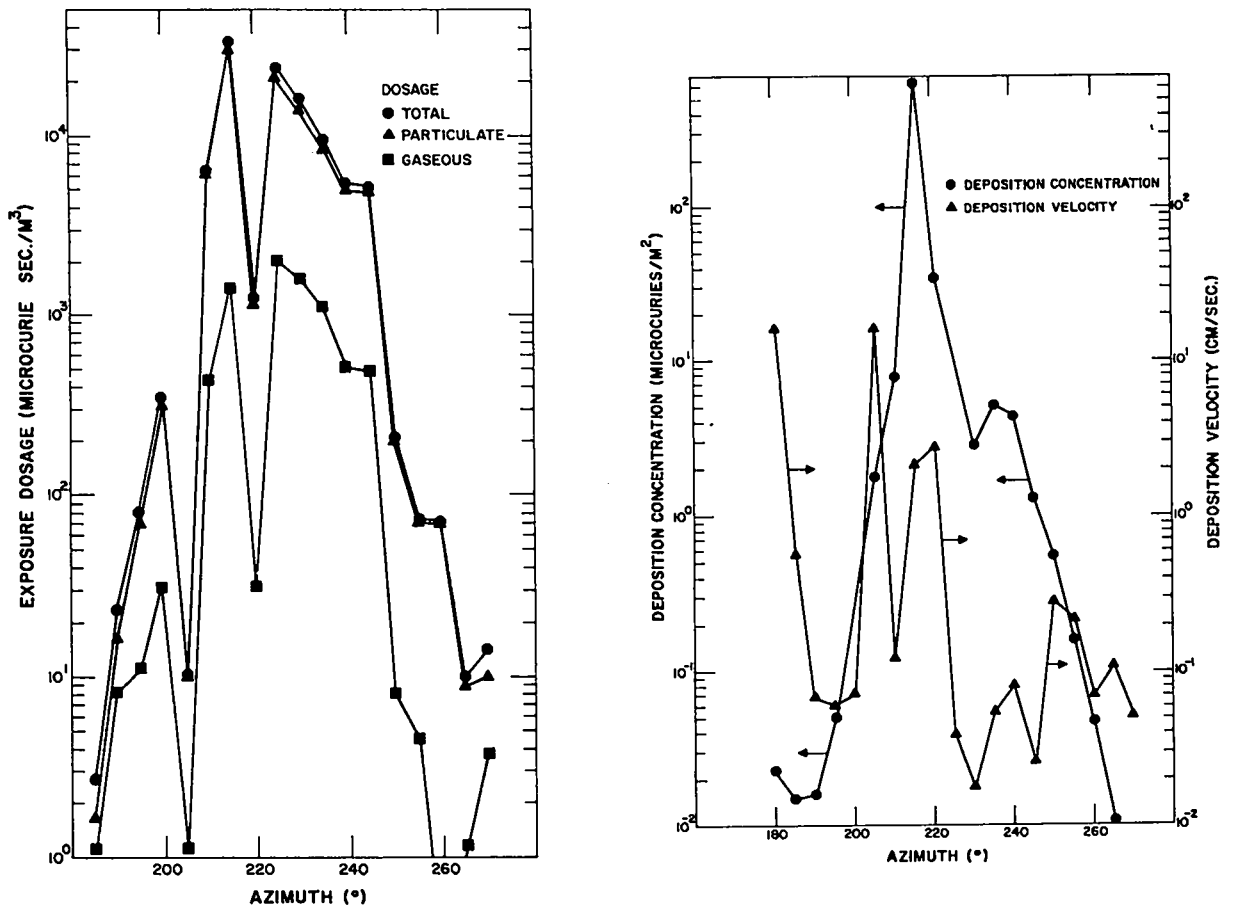Fig. 39. Activity on resin-coated trays. Beta activity corrected to estimated time of cloud passage.

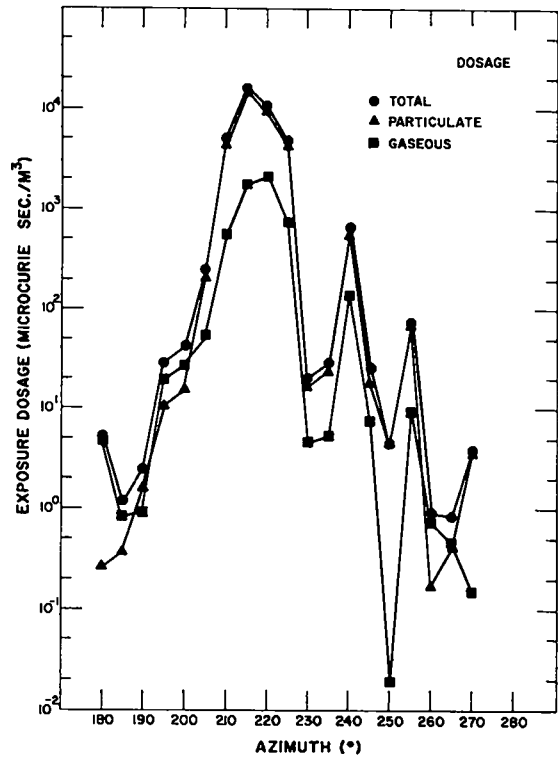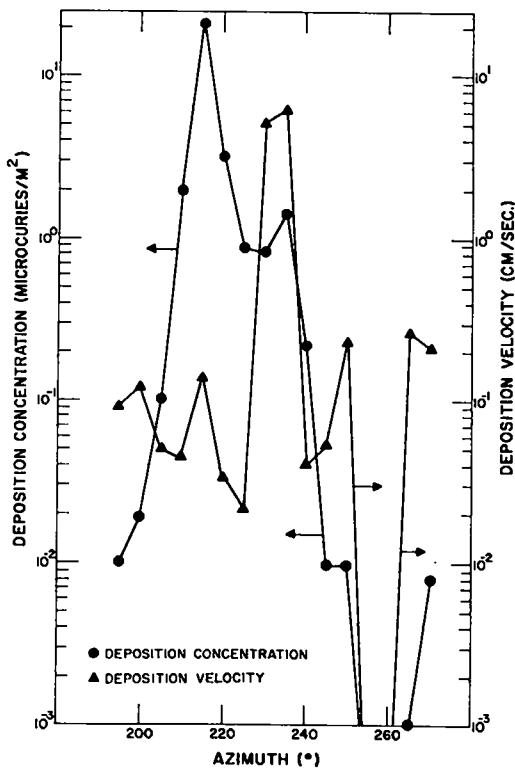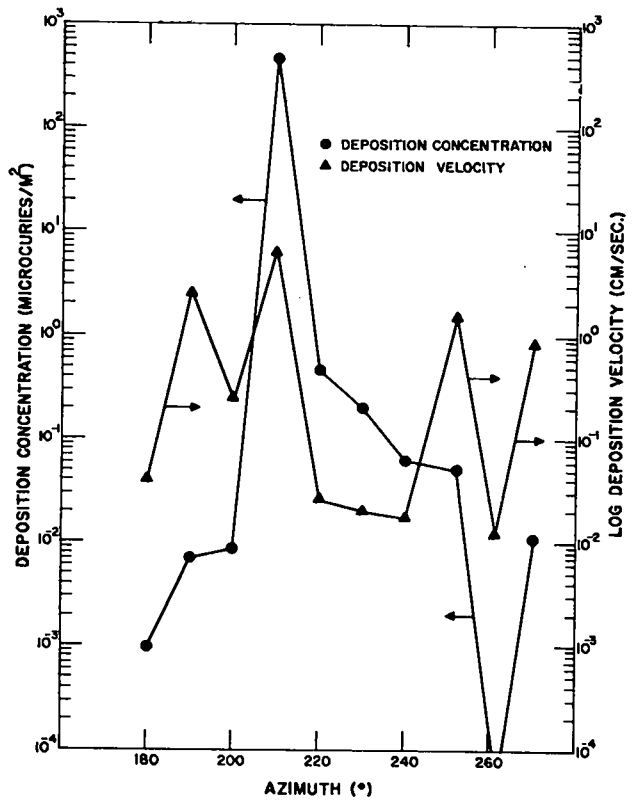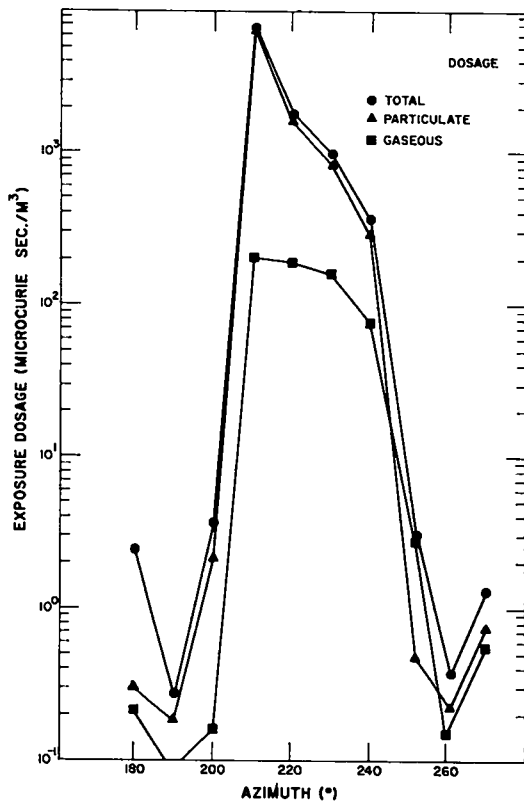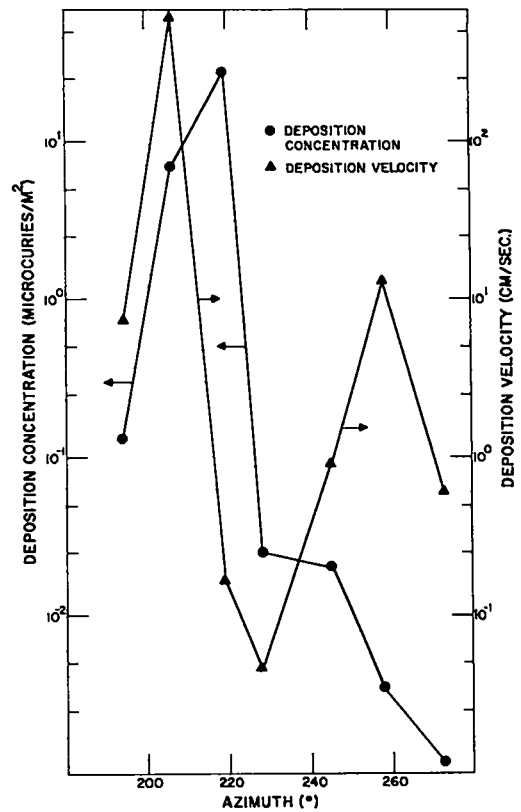Fig. 40. Crosswind dosage, deposition, and deposition velocities — 4,000-ft arc.

Fig. 41. Crosswind dosage, deposition, and deposition velocities — 8,000-ft arc.

Fig. 42. Crosswind dosage, deposition, and deposition velocities — 16,000-ft arc.
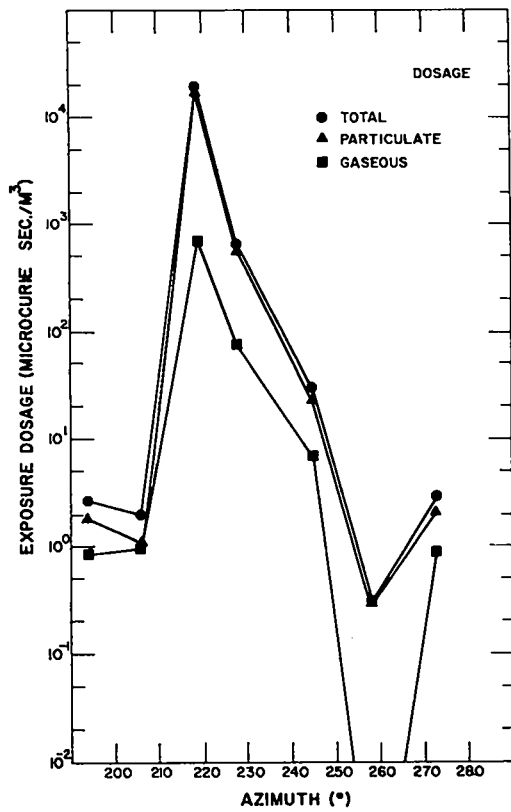
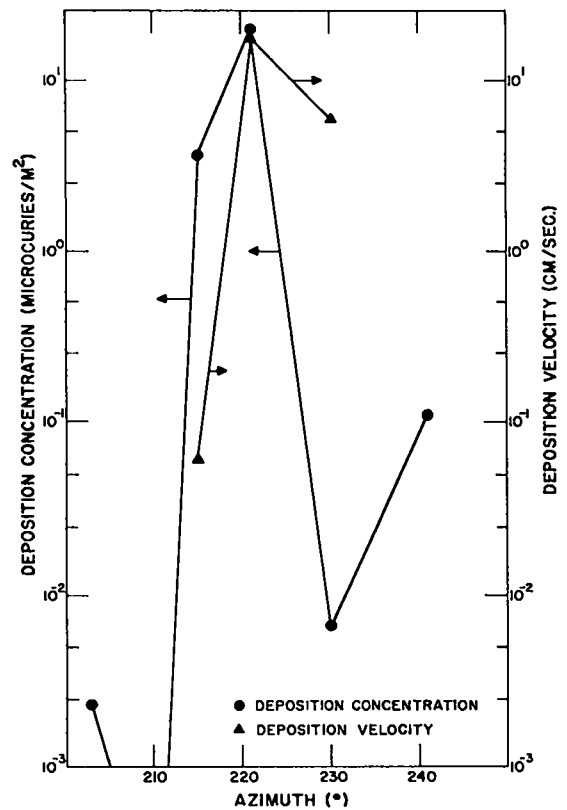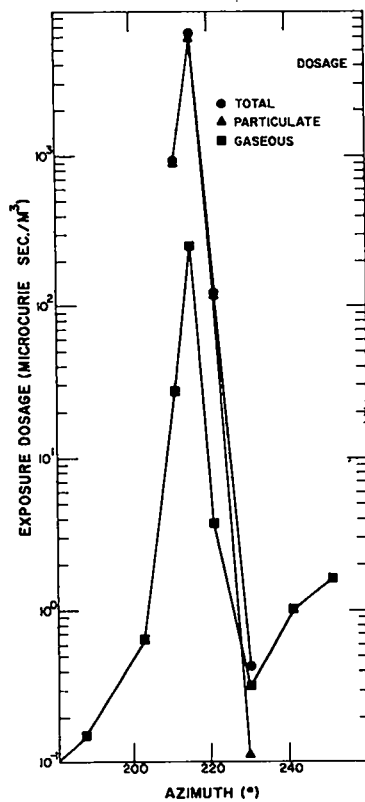Fig. 43.   Crosswind dosage, deposition, and deposition velocities — 32,000-ft arc.

Fig. 44.   Crosswind dosage, deposition, and deposition velocities — 64,000-ft arc.
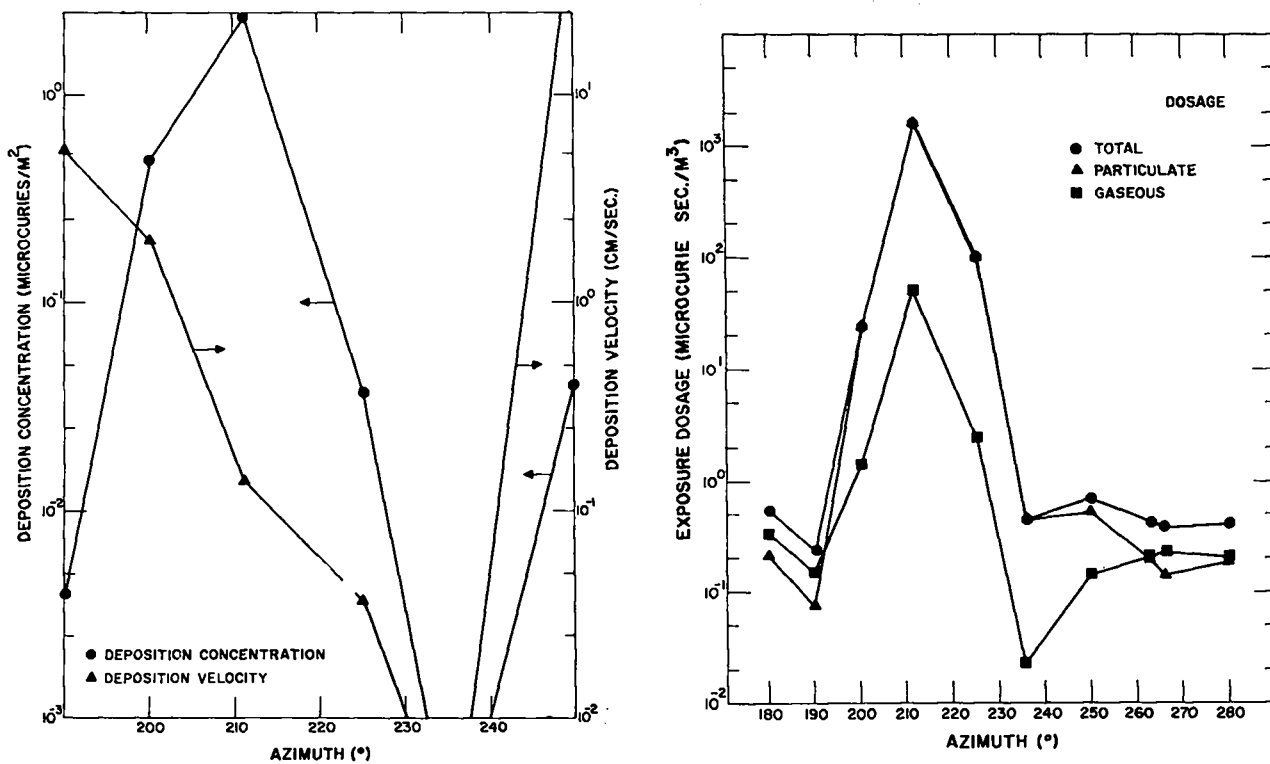
54

Fig. 45.   Crosswind dosage, deposition, and deposition velocities — 128,000-ft arc.
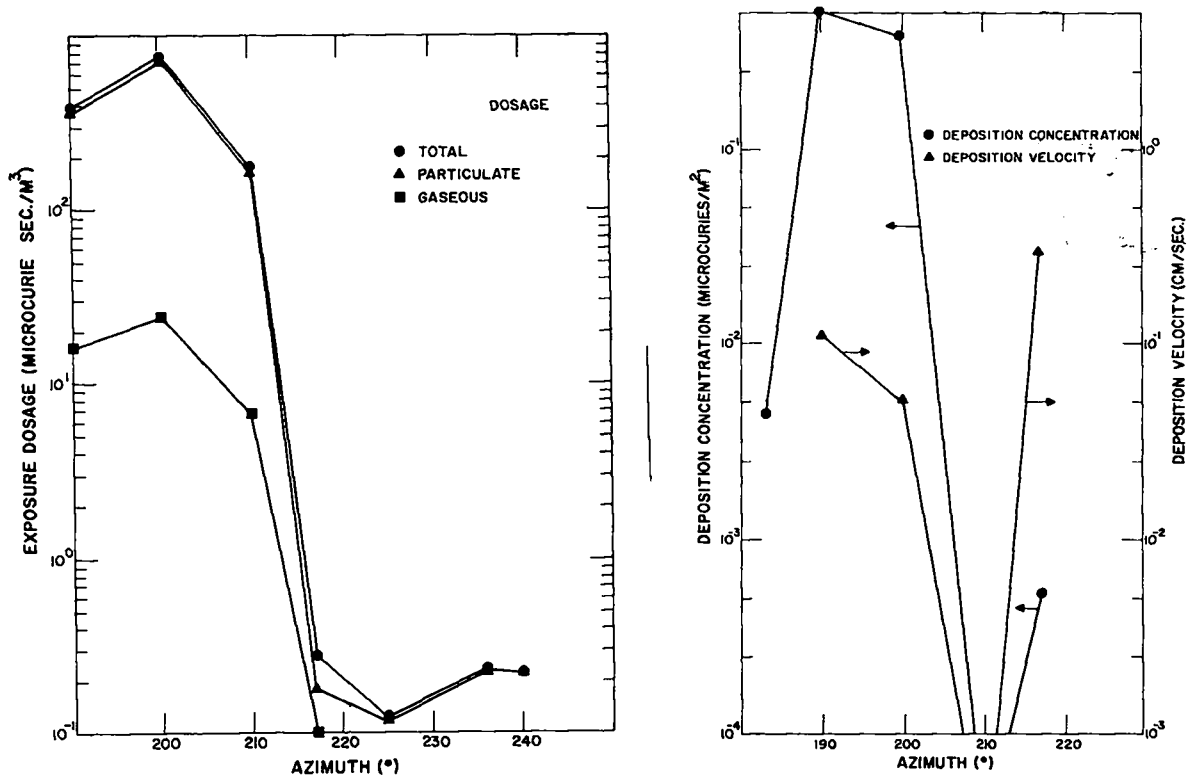

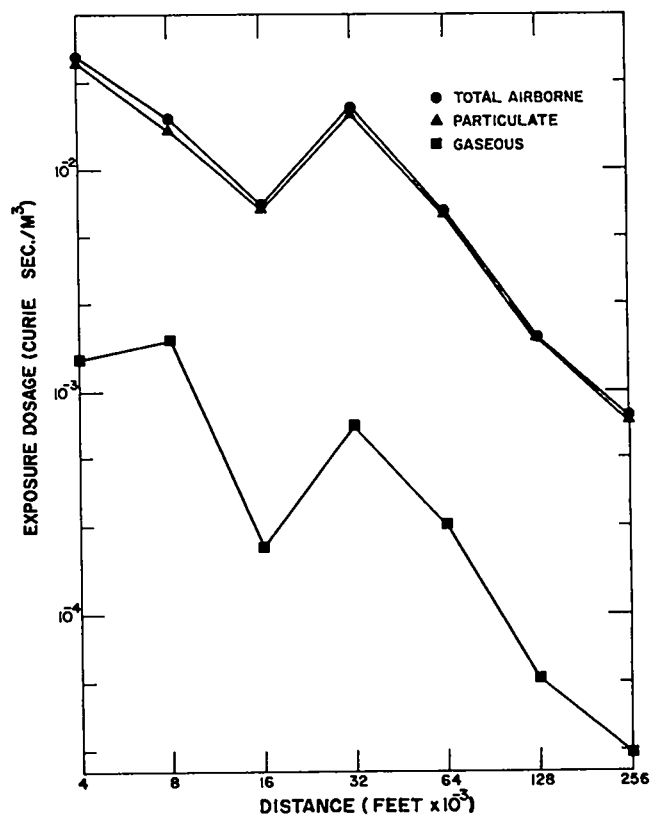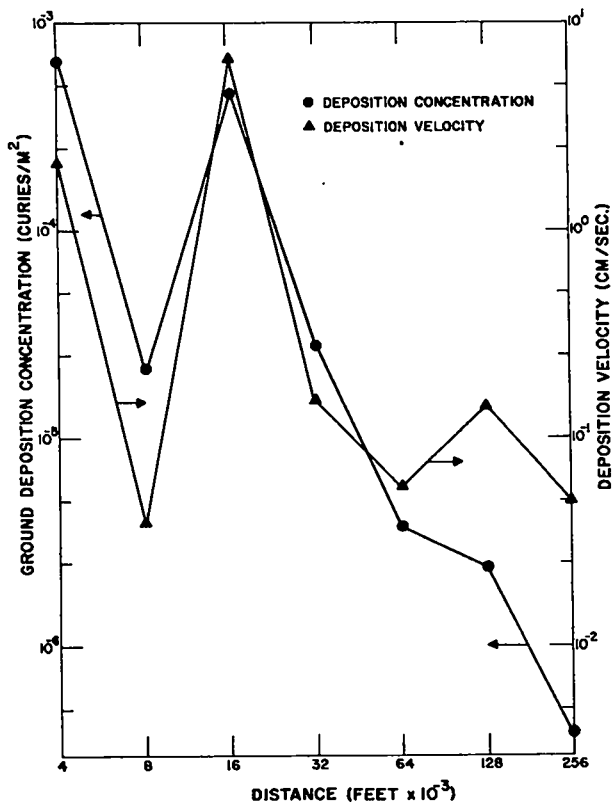Fig. 46.   Crosswind dosage, deposition, and deposition velocities — 256,000-ft arc.

55

Fig. 47. Cloud centerline dosage, deposition, and deposition velocities.
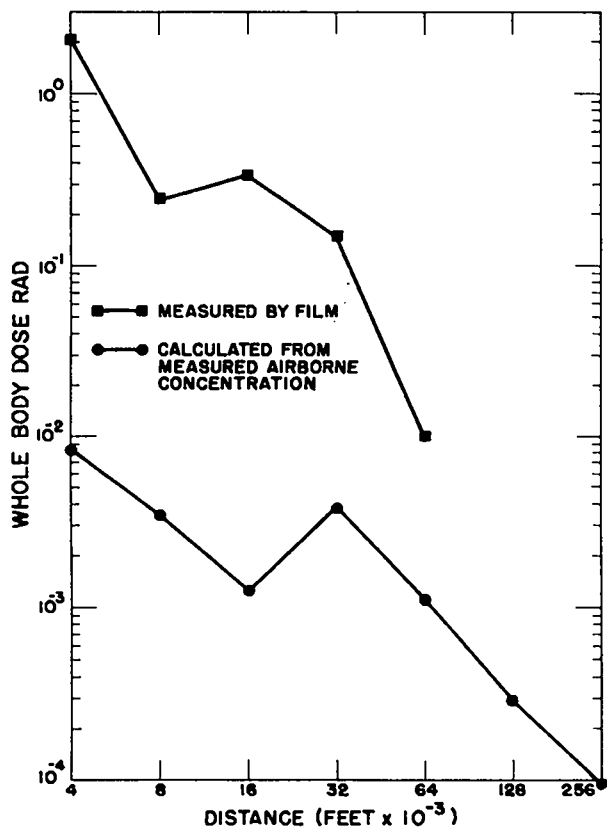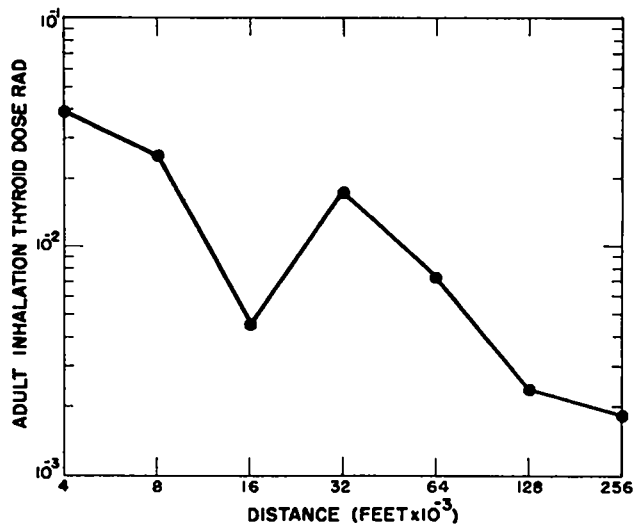

Fig. 48. Centerline whole-body dose.

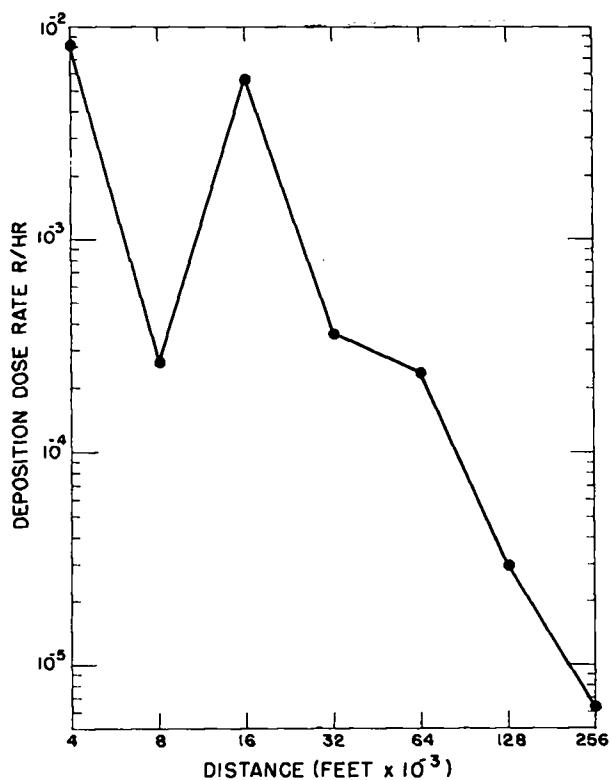Fig. 49. Centerline adult thyroid inhalation dose.

56

Fig. 50. Centerline deposition dose rate.

To obtain an estimate of the source term, or amount of radioactive material released to the cloud, calculations were made using the measured airborne activity concentrations and the dispersion equations of Sutton[17] and Pasquill.[18] Table XVI shows the values of source term vs. distance obtained. Only distances of 16,000 ft and beyond were used, since both models predict negligible ground concentrations from a perfect elevated point source at shorter distances. Even ignoring the two close-range arcs, one obtains an appreciable spread of values for the percentage of fission-product material released. Ignoring the value for 256,000 ft in the Sutton group, one gets as an average about 70% of the fission products released.

TABLE XVI. CALCULATED SOURCE STRENGTH VALUES VS. DISTANCE

Distance (ft)	Percent of Fission Products Released to Cloud	
	Sutton	Pacquill
16,000	33	1610
32,000	92	82
64,000	76	19
128,000	62	31
256,000	284	103

Ignoring the 16,000-ft value in the Pasquill group, one gets as an average about 60%. These average values agree fairly well with the figure of $\frac{2}{3}$, obtained independently by radiochemical analysis of cloud samples taken by aircraft a few minutes after the test, and of debris samples recovered from the test site.

Figure 51 compares pretest predictions of cloud centerline dosages, Sutton and Pasquill estimates using parameters measured during the test, and measured centerline dosages. For the pretest estimate, a 40% release of 10^{21} fissions was assumed, with 15-mph winds and neutral conditions. The posttest exercise used a 67% release of 3×10^{20} fissions and 25-mph winds. Calculations of Sutton's parameters were attempted using the meteorological data from the test, but gave an unsatisfactory spread of values. However, a judgment evaluation of those values resulted in a selection of n = 0.18 and C^2 = 0.067 for the Sutton parameters. Pasquill's stability category C was used for that part of the exercise. It is evident from Fig. 51 that the uncertainty in the pretest parameters led to an erroneous, but comfortably conservative, prediction. The calculations using the posttest data, (and also giving the models the benefit of every doubt) produced better, but still conservative, results. Even this extent of agreement is noteworthy in view of the distances in-
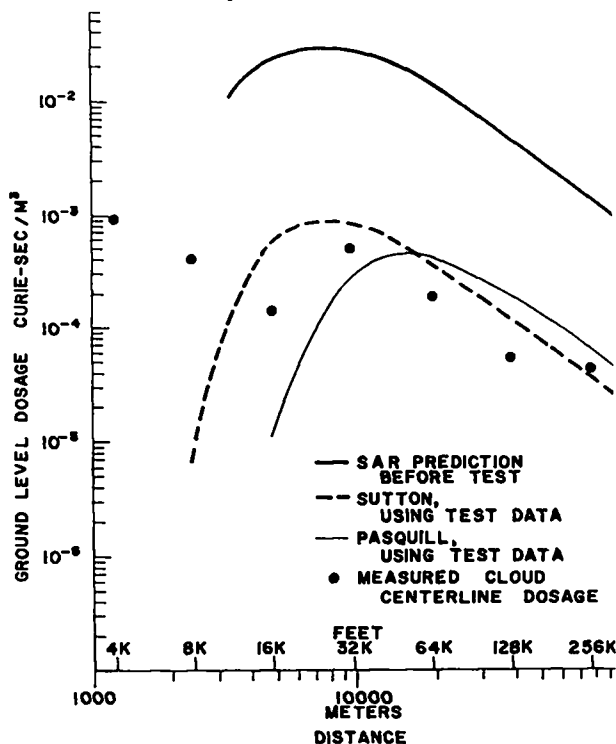

Fig. 51. Comparison of cloud data with theoretical predictions.

volved, however, and leads one to conclude that these two popular dispersion models are useful for predicting downwind radioactivity patterns, particularly since no better model appears to be available.

Beyond the 60 miles or so covered by the LASL array, the cloud wake was observed by the NATS aerial tracking aircraft,[16] and later by Bureau of Radiological Health of the State of California and U.S. Public Health routine air monitoring stations.[5]

The NATS aircraft was airborne approximately 2½ hours after the event, and the radioactive cloud was intercepted 1 hour 45 minutes later at an altitude of 9,000 ft near Pyramid Peak, on the western side of Death Valley, approximately 60 miles southwest of the test point. Figure 52 shows the subsequent track mapped by the aircraft. Preliminary analysis of the gamma pulse height spectra taken near the cloud indicated the possible presence of ^{135}I, ^{134}I, ^{88}Rb, and ^{88}Kr. The altitude of maximum activity appeared to be 7,000 ft MSL. The terrain prohibited the aircraft from descending below 7,000 ft MSL. Darkness and the mountainous terrain ended this first tracking procedure approximately 6 hours 30 minutes after the event.

At 11 hours 20 minutes after the Kiwi-TNT event. the NATS aircraft again attempted to locate the effluent cloud. Searching procedures were restarted near Daggett, California, at 2310 PST, 12 hours 10 minutes after the event. The actual flight path is shown in Fig. 53. Positive signals were received over the ocean from Los Angeles to near Santa Barbara. Gamma pulse height spectral data obtained in this area differed from normal background, and indicated the presence of photopeaks that would have been expected at that time after the Kiwi-TNT event. The aircraft stopped tracking at 0205 PST to refuel near Los Angeles. After refueling, it returned to the previous search area and again detected weak, but positive signals, indicating that the effluent was continuing to move farther out to sea.

A few days after the Kiwi-TNT event, Public Health officials observed increased radioactivity in routine air samples from the Barstow, San Bernardino, Los Angeles, and San Diego, California, areas on January 13 and 14, 1965. These samples helped to confirm the presence of the cloud wake out to the Pacific Ocean.
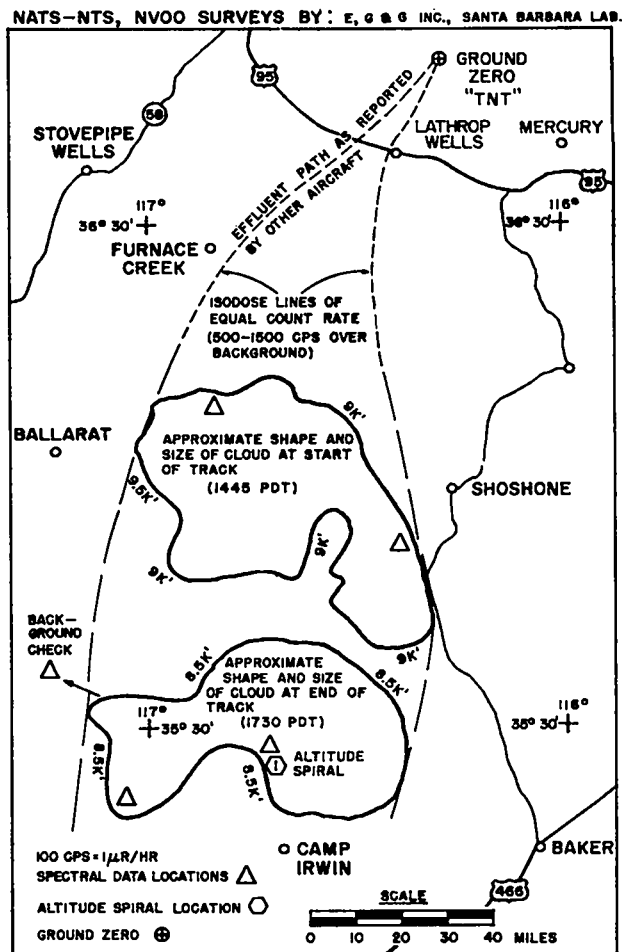
Fig. 52. Cloud track.

IX. THE RADIOLOGICAL COMPOSITION OF THE CLOUD

The qualitative analysis of the effluent samples collected by LASL used the method developed during normal tests in the Rover series. The method, described in detail in LA-3397-MS,[19] consists basically of following the decay of selected samples, and, after all data are collected, segmentally subtracting out (stripping) the activity of progressively shorter-lived isotopes from the activity of the mixture.

Samples are selected on the basis of initial activity, location in the array, and type. These samples are repeatedly counted for an extended period at intervals that depend upon the age of the sample. At each counting, a gamma pulse height spectrum is also obtained for each of these samples. The number of samples is reduced, when possible, by cross-comparison and elimination of all but one of any group exhibiting identical
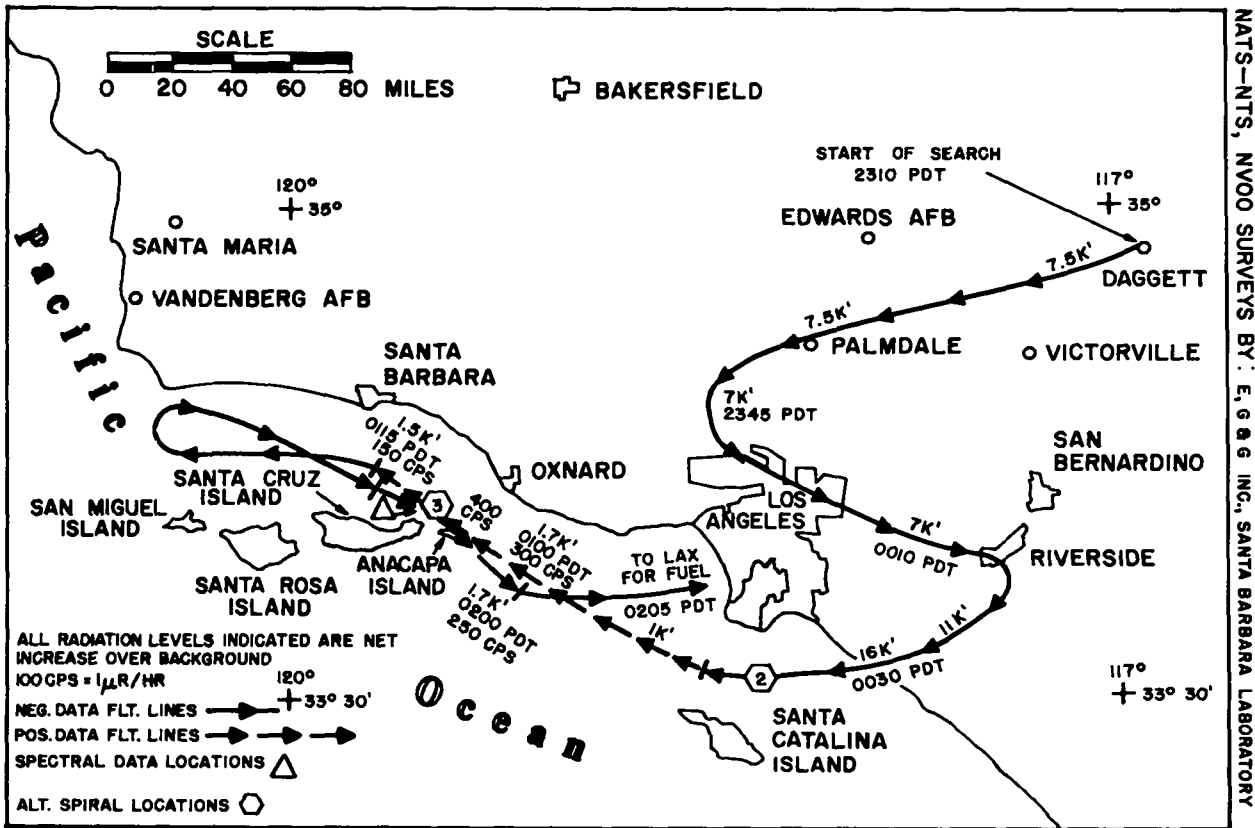
Fig. 53. Flight path of cloud-tracking aircraft.

characteristics. This process is continued until the longest-lived isotopic component can be identified and measured, or until the activity level of the sample becomes insignificant. The process of curve stripping is then employed to quantitatively determine the isotopic composition of the sample.

In the ideal strip analysis, the decay of the sample is followed until only a single long-lived isotope is present. The activity of this isotope is then subtracted from the activity of the mixture. The resultant curve is then plotted, and the process is repeated, subtracting this time the isotope of next-longest half life. Progressive subtraction is repeated until all isotopic activities have been determined. During the process, the gamma pulse height spectra are used to identify the isotopes present in significant quantities during selected periods of the decay. In practice, the ideal case is seldom encountered and the isotopic contributions to the activity must be subtracted in pairs or triplets. When this is necessary, a least-squares technique is employed to fit the activities of the appropriate pair or triplet to the tail of the residual curve. As a check on each analysis, a synthesized plot is made of the theoretical decay of the isotopes determined during the analysis, and this is

compared for goodness of fit with the original curve of sample decay data. The determined isotopic composition is also checked for consistency with gamma pulse height spectra for the sample.

For the Kiwi-TNT event, this method was used only for the charcoal cartridge and resin-coated tray samples. The gamma pulse height spectra for the filter samples revealed that these samples contained essentially gross fission products. This was confirmed by constructing hypothetical curves of gross fission-product activities, less those isotopes and their daughters which would have been gaseous at the time of collection, and comparing these curves to the sample decay curves. Detailed radiochemical analysis of cloud samples collected by aircraft a few minutes after the event further confirmed the comparison. The ratios of activity of the various fission products were found to be no more than 1.5 times the theoretical ratios of these products.

The analysis of the charcoal cartridges indicated that the gaseous material was mostly iodines and not greatly different from what would be expected from sampling a cloud of unfractionated fission products with the iodines still largely

59

in the gaseous state. The deposited activity was quite different from the airborne particulate activity, containing predominantly refractory isotopes. Iodine-135 was the only isotope of iodine identified in these samples.

Table XVII lists the apparent zero-time composition of the material collected by the charcoal cartridges and resin-coated trays as determined by the curve stripping technique. The activity, A_t, of any sample at any time, t, may be determined by

$$A_t = \Sigma_i A_i e^{-\lambda_i t},$$

where A_i is the value given in Table XVII for the *i*th isotope, and λ_i is its decay constant. Where parent-daughters are present, the appropriate Bateman equation should be used in the sum.

The presence of [135]Xe on the cartridges is probably due to ingrowth from the [135]I. When this growth begins is not precisely known, but a zero-time value of [135]Xe activity is given which produces an excellent fit to the data. The [135]Xe is probably completely swept out of the cartridges during sample operation, and is allowed to diffuse freely from them after active sampling but before they are packaged for counting. Xenon-133 does not similarly appear, because its gamma energy, 80 keV, is below gamma-counting system threshold of 100 keV. (Gamma counting must be used on the charcoal cartridges because their structure results in almost complete beta self-absorption.) The presence on the cartridges of the solid isotopes, [132]Te and [140]Ba-La is not well understood except that they exist as extremely fine particles, but this phenomenon has frequently been observed in other studies of fission products released to the atmosphere.

TABLE XVII.   DECAY CURVE DATA

Airborne Gaseous Material 4,000-ft arc		Airborne Gaseous Material 8,000-ft arc	
Isotope	% at Zero Time	Isotope	% at Zero Time
I-134	48.2	I-134	81.1
I-132	1.50	I-135	10.6
I-135	44.8	Xe-135	7.38
Xe-135	3.64	I-133	0.923
I-133	1.78	Te I-132	0.0179
Te I-132	0.0230	I-131	0.0340
I-131	0.0392	Ba-La-140	0.00640

Airborne Gaseous Material 16,000- to 256,000-ft arcs		Deposited Activity All Arcs	
Isotope	% at Zero Time	Isotope	% at Zero Time
I-134	76.3	I-135	59.9
I-135	15.8	Zr Nb-97	32.8
Xe-135	5.9	Mo-99	6.65
I-133	1.80	Ba-La-140	0.554
Te I-132	0.0288	Ru-103	0.0444
I-131	0.0712	Zr Nb-95	0.0444
Ba-La-140	0.0132		

X. THE IMPACT ON THE NEIGHBORHOOD

The material in this chapter is largely from the USPHS "Final Report of Off-Site Surveillance for the Kiwi-TNT Experiment."[5]

Under a Memorandum of Understanding with the Atomic Energy Commission, SWRHL conducts a program of radiological monitoring and environmental sampling in the off-site area surrounding the Nevada Test Site and the Las Vegas Bombing and Gunnery Range. In addition to their

routine sampling network, the USPHS placed additional monitors and sampling stations in the anticipated downwind direction from the Kiwi-TNT event to better document the impact of the test on the neighborhood.

Twelve ground monitoring teams tracked the cloud passage with portable instruments. Each team was equipped with an Eberline E500B (0-2,000 mR/hr on five scales), a Precision Model III Scintillator (0-5 mR/hr on six scales), and a Victoreen Radector Model No. AGB-50 B-SR (0-50,000 mR/hr on two scales). Positioning of the ground monitors was assisted by aerial dose-rate readings made by two PHS monitors in an Air Force U3-A aircraft, which was primarily engaged in aerial cloud tracking and sampling. Forty-five routine air samplers were operated in Nevada, Utah, Arizona, and California. In addition, 18 supplementary air samplers, and eight Eberline RM-11 dose-rate recorders (0.1 to 100 mR/hr on a single logarithmic scale) were placed in the anticipated downwind sector. All air samplers were equipped with Whatman No. 41 filters backed with MSA charcoal cartridges. Film badges were issued to 157 people off site, including 67 at Lathrop Wells, 30 in the Amargosa Farm area, and five at Death Valley Junction. The film badge

used was the DuPont type 555 film packet, with two films, 20- to 100-mR range and 100- to 2,000-mR range. Nine of the film badges were in or near the downwind sector. Seventy-four milk samples were collected and analyzed for fission products following the Kiwi-TNT event. The samples were collected from two ranches in the Amargosa Farm area and from 14 locations in southern California. Vegetation samples were collected from most milk sampling locations. Water samples were collected from two open ponds, at Death Valley Junction and at Shoshone, California, the day following the test. Figure 54 shows the downwind USPHS sampling and monitoring locations within approximately 75 miles of the test site. Figure 55 shows a larger area, out to the Pacific Ocean, where milk samples were collected in southern California.

All air samples were counted for gross beta activity immediately upon receipt at SWRHL. Samples exhibiting significant radioactivity were then further analyzed as described in Reference 5. All charcoal cartridges and filters were also analyzed by gamma pulse height analysis. The minimim detectability of this analysis for ^{131}I, ^{132}I, ^{133}I, and ^{135}I is approximately 200 pCi. Milk, water, and vegetation samples were analyzed by gamma pulse height analysis. The lower limit of detection for gamma emitters in milk samples in this system is 20 pCi/liter.

A summary of positive gamma dose-rate measurements made by the monitoring teams and dose-rate recording instruments is given in Table XVIII. The data indicate a measurable cloud width of approximately 5 miles by the time it reached Highway 95, just south of the Test Site border; the eastern edge of the cloud was approximately at Lathrop Wells. Farther downwind, measurable does rates occurred in the Amargosa Desert to the west of Highway 29. No activity was measurable in the Furnace Creek area of Death Valley. The maximum dose rate measured by a ground monitoring team was 70 mR/hr, approximately 1.5 miles west of Lathrop Wells on Highway 95. A numerical integration of dose rates vs. time gave a calculated external exposure dose of 5.7 mR for this location. This location is normally unpopulated, but there were eight persons engaged in sampling experiments there during the test. A similar calculation was made for the Amargosa Farm area and Death Valley Junction. The external gamma dose calculated for these populated locations did not exceed 0.5 mR. Highway 95 was remonitored at about 0900 the morning after the test. Some small residual contamination was found between Lathrop Wells and a point 4
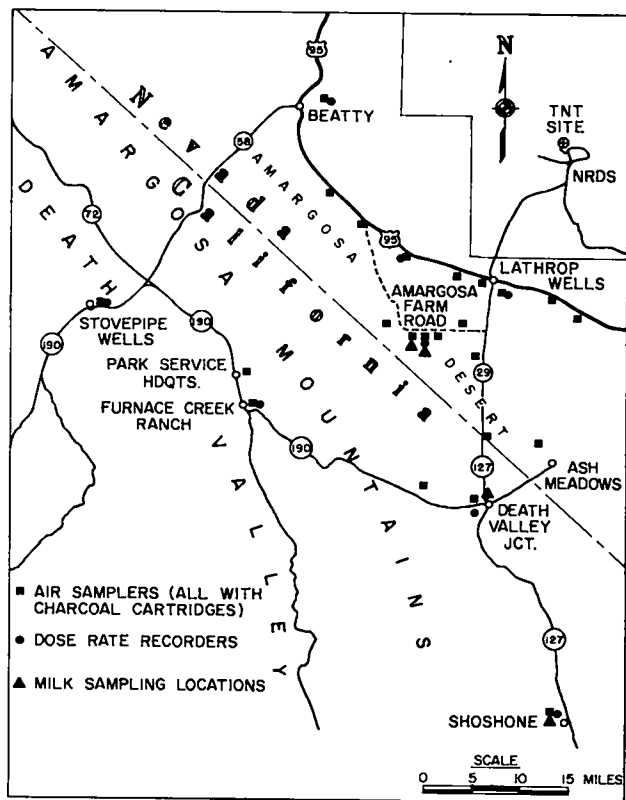

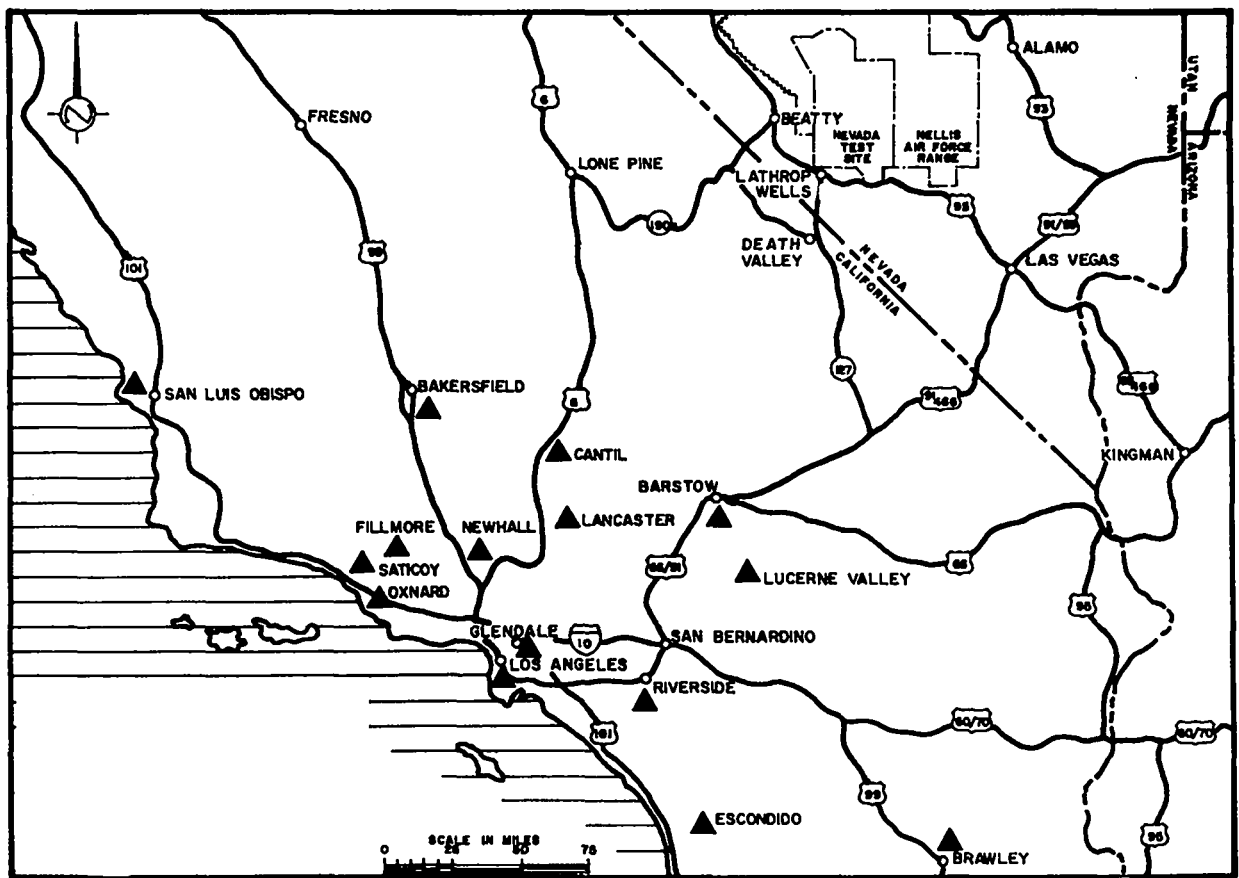Fig. 54. Downwind USPHS sampling and monitoring locations.

61

Fig. 55. Milk sampling locations.

miles to the west. A maximum net peak dose rate of 0.05 mR/hr was found 2.6 miles west of Lathrop Wells. A similar survey of Highway 29 and the Amargosa Farm area found no readings above background.

A summary of the milk sampling locations is shown in Table XIX. The Amargosa Desert locations and 14 California locations were sampled for approximately 1 week starting the day after the test. None of the 74 milk samples contained detectable quantities of fresh fission products. Animals at all but one location were being fed baled hay; the cows at Brawley, California, were fed green fodder. Natural vegetation samples from the Saticoy-Fillmore-Newhall area in California contained fresh fission products. However, cow feed and milk at these locations did not contain detectable quantities of fresh fission products, nor did vegetation samples from an area extending from Barstow to Santa Barbara, California. Neither of the water samples collected contained fresh fission products.

Table XX summarizes PHS air samples that exhibited positive activity. Because most of these samplers were in the same area as the LASL array, but not at identical locations, and were collected and analyzed in similar, but not identical, fashion, the temptation to compare airborne activity dosages measured by the two systems is overwhelming. Such a comparison reveals that order of magnitude discrepancies exist between samples which were not far apart. However, the consistency (or lack thereof) between the two sets of data appears to be about the same as that within each set.

The Bureau of Radiological Health of the State of California routinely operates 14 air samplers within the state. Kiwi-TNT effluent passage was noted on several samplers whose locations are given in Table XXI. The results of these analyses were supplied to SWRHL. The samples were counted within 2 days following collection, and the results were extrapolated to end of sample collection assuming a $t^{-1.2}$ decay. Natural

62

TABLE XVIII.   DOSE RATES MONITORED OFF THE TEST RANGE COMPLEX ON JANUARY 12, 1965.

Location*	Time of Peak Dose Rate (PST)	Time During Which Dose Rates Were Greater than Bkgd	Net Peak Gamma Dose Rate (mR/hr)
3 mi. N of Hwy. 95 on Lathrop Wells-NRDS Road (NRDS Boundary)	1143	1130-1207	70
Lathrop Wells	1146	1125-1148	2.0
1.5 mi. W of Lathrop Wells	1147	1138-1158	70
5 mi. W of Lathrop Wells	1207	1200-1220	0.18
Dansby's Ranch (5 mi. S of Lathrop Wells on Rt. 29 and 6 mi. W on Amargosa Farm road)	1252	1232-1324	0.67
15.3 mi. S of Lathrop Wells on Hwy. 29	1328	1305-1345	0.28
Death Valley Junction	1349	1315-1428	0.11
7.5 mi. W of Death Valley Jct. on Hwy. 190	1335-1415	1300-1440	0.23

Dose Rate Recorder Data on January 12, 1965

Location*	Time of Peak Dose Rate (PST)	Time During Which Dose Rates Were Greater than Bkgd	Net Peak Gamma Dose Rate (mR/hr)
Lathrop Wells	1146	1120-1250	2.0
Dansby's Ranch	1252	1145-1335	0.67
Death Valley Jct.	1349	1250-1430	0.11

Recorders at Beatty, Nevada, and Stovepipe Wells, Furnace Creek Ranch, and Shoshone, California, did not indicate activity above background.
*See Fig. 54.

TABLE XIX.   USPHS MILK SAMPLING ACTIVITY FOLLOWING KIWI-TNT

Location	Number of Days Sampled	Inclusive Dates
Lathrop Wells, Nevada		
Dansby's Ranch	6	1/13/65 to 1/19/65
Selbach Ranch	6	1/13/65 to 1/19/65
Barstow, California	8	1/14/65 to 1/22/65
Bakersfield, California	7	1/14/65 to 1/20/65
Cantil, California	1	1/15/65
Lancaster, California	1	1/15/65
Glendale, California	1	1/15/65
Lucerne Valley, California	1	1/14/65
Los Angeles, California	7	1/14/65 to 1/20/65
Riverside, California	6	1/15/65 to 1/20/65
Escondido, California	6	1/15/65 to 1/21/65
San Luis Obispo, California	7	1/14/65 to 1/20/65
Saticoy, California	2	1/15/65 to 1/18/65
Newhall, California	7	1/14/65 to 1/20/65
Fillmore, California	1	1/16/65
Brawley, California	7	1/15/65 to 1/21/65

TABLE XX. AIR SAMPLES WITH POSITIVE RESULTS COLLECTED FOLLOWING THE KIWI-TNT EXPERIMENT.

Location (See Figure 10.1)	Start-Stop Times for Samples (PST) 1/12/65	Volume Sampled (m³)	Analysis of Prefilters for Beryllium	Prefilter Gross Beta Concentration at End of Collection (pCi/m³)	Integrated Air Concentration (pCi-sec/m³)	Collector (b)	Gamma Pulse Height Analyses at End of Collection (pCi/m³)			
							^{131}I	^{132}I	^{133}I	^{135}I
Lathrop Wells	1015-1240	45	ND[a]	4.3×10^2	3.74×10^6	P	ND	ND	ND	ND
						C	ND	ND	ND	ND
Hwy. 95, 1.5 mi. W of Lathrop Wells	1045-1220	34	—	2.1×10^5	1.2×10^9	P	6.3×10^2	1.4×10^4	1.3×10^4	6.0×10^3
						C	1.5×10^2	2.1×10^2	2.9×10^2	1.9×10^3
Hwy. 95, 5 mi.. W of Lathrop Wells	1100-1530	87	ND	8.7	1.41×10^5	P	ND	2.5	3.2	ND
						C	ND	ND	ND	ND
Hwy. 29, 7 mi. S of Lathrop Wells	0800-1435	130	—	1.3×10^3	3.08×10^7	P	ND	1.2×10^2	1.2×10^2	40
						C	ND	4.3	3.5	18
Amargosa Farm Road 3.5 mi. W of Hwy. 29	0855-1610	166	—	1.9×10^3	4.96×10^7	P	ND	48	48	ND
						C	ND	39	28	34
Amargosa Farm Road 5.0 mi. W of Hwy. 29	0735-1513	150	—	4.1×10^3	1.12×10^8	P	ND	5.1×10^2	5.1×10^2	ND
						C	ND	24	23	59
Amargosa Farm Road 6.0 mi. W of Hwy. 29	0810-1440	125	ND	7.3×10^2	1.71×10^7	P	(no analysis)			
						C	ND	9.6	60	40
Amargosa Farm Road 6.5 mi. W of Hwy. 29	0810-1508	136	—	5.7×10^2	1.43×10^7	P	ND	61	61	ND
						C	ND	1.3	12	7.6
Amargosa Farm Road 9.3 mi. W of Hwy. 29	0825-1530	160	ND	92	2.35×10^6	P	ND	11	9.5	ND
						C	ND	1.3	7.3	2.3
Hwy. 29, 15.3 mi. S of Lathrop Wells	0845-1535	136	—	1.1×10^3	2.71×10^7	P	ND	1.2×10^2	1.5×10^2	26
						C	ND	2.8	28	15
Death Valley Jct.	0650-1510	168	—	2.4×10^3	7.20×10^7	P	ND	2.5×10^2	2.7×10^2	34
						C	ND	10	8.0	34
Hwy. 190, 7.5 mi. W of Death Valley Jct.	1310-1500	30	ND	2.7×10^4	1.78×10^8	P	ND	3.3×10^3	3.1×10^3	5.3×10^2
						C	ND	20	5.0×10^2	3.3×10^2

(a) ND = not detectable.
(b) P = prefilter,   C = charcoal cartridge.

TABLE XXI. CALIFORNIA STATE AIR SAMPLER LOCATIONS REPORTING EVIDENCE OF KIWI-TNT CLOUD PASSAGE.

Location	24-Hour Sample Ending 0800 PST on Date Shown	Volume Sampled (m³)	Prefilter Gross Beta Concentration at End of Collection (pCi/m³)
Barstow	1/13/65	64.4	360
Barstow	1/14/65	63.3	6.9
San Bernardino	1/13/65	60.1	16.4
San Bernardino	1/14/65	64.5	6.2
Los Angeles	1/13/65	58.1	6.3
Los Angeles	1/14/65	63.3	8.8
San Diego	1/13/65	81.8	3.3
San Diego	1/14/65	80.3	6.2

levels of radioactivity in air at the sampled locations generally do not exceed 2 pCi/m³. In addition, the Los Angeles station of the USPHS Radiation Surveillance Network reported fresh fission-product activity in samples collected following the Kiwi-TNT event. Twenty-four-hour samples ending on the mornings of January 13 and 14 at Los Angeles indicated gross beta concentrations of 0.93 and 1.82 pCi/m³, respectively, extrapolated to collection time. A gamma-ray analysis of these two samples indicated unquantitated traces of ^{95}Zr-Nb and $^{103, 106}$Ru-Rh on both days and ^{131}I on January 13; ^{132}Tc-I levels of 1.5 pCi/m³ were reported on both days.

Thyroids of several members of the USPHS off-site survey teams were counted at the USPHS Whole-Body Counting Facility to determine iodine uptake following the Kiwi-TNT event. All thyroid doses due to iodine were less than 3.3 ± 1 mR, and were due to the 131 and 135 isotopes. The monitor 1.5 miles west of Lathrop Wells who experienced a dose rate of 70 mR/hr was included in the study, and received the peak thyroid dose of 3.3 mR. Comparison of measured thyroid dose with that calculated from LASL air sampling data is quite good. Data from Table XIV and Fig. 49 indicate that a thyroid dose calculated from air sampling data for a monitor approximately 15 miles from the test point would be 4 mR.

XI. CONCLUSIONS

The Kiwi-TNT was a successful simulation of a maximum credible accident due to extremely rapid reactivity insertion into the core of a nuclear rocket reactor. This type of accident was of major concern at the time of its conception and planning; emphasis is now on the loss-of-coolant accident.

In the reactivity insertion accident, the fission process and deflagration occur essentially instantaneously. The fission products are produced and released at almost the same instant. Although postulation of the reactor core inventory of products due to any previous fissions is complicated because an infinite variety of fission-product inventories can be conceived, their effects can be extrapolated from the results of this test.

In the loss-of-coolant accident, many more parameters are involved than in the fission-product release. Fission-product release would not be instantaneous, and the release rate would depend upon whether the reactor was critical or subcritical at the time of the collant loss; it would depend upon the power level and previous power history of the core; each chemical element would behave differently, rather than all fission products being released in about equal proportions. Consideration of all these factors is appropriate only for particular cases and is too extensive for inclusion here. Therefore, only conclusions pertinent to the Kiwi-TNT and similar reactivity insertion incidents occurring with uncontaminated fissionable assemblies will be stated.

Severe property damage to normal objects and structures by the blast from the eruption would probably be limited to a radius of about 100 ft. Minor blast damage, such as window breakage, would be confined to about a 1,000-ft

radius. Personnel injuries from blast and heat would be almost inconsequential as compared to radiation injuries.

Out to approximately 300 ft, which is beyond the range of probable blast injury, radiation exposures would probably be fatal, being in excess of 750 rads. Between approximately 300 and 750 ft, varying degrees of radiation injury, including some fatalities, would occur as exposures would be between 100 and 750 rads. From 750 to approximately 2,000 ft downwind, little, if any, injury or clinical effects would occur, but exposures would exceed 3 rads and would require administrative investigation and reporting. Beyond approximately 1.5 mile, doses even in the path of the cloud would be below a few hundred millirad, and should present no problems.

The seriousness of radioactive contamination is difficult to assess, since it depends so heavily on the value and potential uses of the contaminated real estate. However, 1 day after the Kiwi-TNT event, contamination exceeding 100 mR/hr was within 1,200 ft downwind and 300 ft upwind of the test point; the 1 R/hr line at this time was 300 ft downwind and less than 100 ft upwind. By 1 week after the event, the 100 mR/hr area was 300 ft downwind and less than 100 ft upwind of the test point. Within a few hours of the test, contamination above 1 mR/hr was difficult to find beyond 2 miles, although a few "hot spots" of several mR/hr were discovered out to 10 miles on the day of the test. These rapidly decayed away to insignificance. Beyond 12 miles, no contamination above 1 mR/hr was found.

No radioiodine was discovered in milk following Kiwi-TNT; however, cows downwind during cloud passage were not grazing but were being fed baled fodder. Nevertheless, the minimal radioiodine found in samples of deposited activity and vegetation indicates that radioiodine contamination in milk, even if encountered, would have been well below levels of concern.

In the briefest summary, a Kiwi-TNT type of excursion, without a fission-product inventory in the reactor, creates inconsequential hazards to personnel and property beyond about 2 miles, a distance that can be reasonably expected to lie outside test areas.

REFERENCES

1. L. D. P. King (ed.), "Description of the Kiwi-TNT Excursion and Related Experiments," LA-3350-MS (Confidential RD), Los Alamos Scientific Laboratory (July 1966).

2. C. A. Fenstermacher, L. D. P. King, and W. R. Stratton, "Kiwi Transient Nuclear Test" (p. 226); and W. R. Stratton, C. A. Fenstermacher, L. D. P. King, D. M. Peterson, and P. M. Altomare, "Analysis of the Kiwi-TNT Experiment" (p. 250); AIAA Propulsion Joint Specialist Conference, June 14-18, 1965, Colorado Springs, Colo., AIAA Bull., 2, 5 (1965).

3. L. D. P. King, "Description of the Kiwi-TNT Excursion" (p. 126); W. R. Stratton, D. M. Peterson, and P. M. Altomare, "Analysis of the Kiwi-TNT Experiment" (p. 126); and Beverly Washburn and Charles Hudson, "Pin Technique for Displacement Measurements in Kiwi-TNT" (pp. 127-128); Trans. Am. Nucl. Soc., 8, 1 (1965).

4. L. D. P. King, "Safety Neutronics for Rover Reactors," LA-3358-MS (Confidential RD), Los Alamos Scientific Laboratory (October 1965).

5. "Final Report of Off-Site Surveillance for the Kiwi-TNT Experiment," SWRHL-17r, Southwestern Radiological Health Laboratory, U. S. Public Health Service, Las Vegas, Nevada (August 6, 1965).

6. "Nevada Aerial Tracking System, Very Preliminary Report of Kiwi-TNT Event," EG&G, Inc., Santa Barbara, California (January 21, 1965).

7. P. K. Lee and F. C. V. Worman, "Integral Gamma and Neutron Measurements on the Kiwi-TNT," LA-3304, Los Alamos Scientific Laboratory (May 1965).

8. E. E. Campbell (comp.), "Kiwi-TNT Particle Study," LA-3337-MS (Confidential RD), Los Alamos Scientific Laboratory (August 1965).

9. R. V. Fultyn and C. J. Boasso, "Fuel Element and Support Element Fragment Study —Kiwi Transient Nuclear Test," LA-3445-

MS (Confidential RD), Los Alamos Scientific Laboratory (December 1965).

10. H. F. Mueller and D. A. Wilson, "Analysis of Meteorological Data for the Kiwi-TNT Reactor Test," WBRS-LA-9, Weather Bureau Research Station, U. S. Department of Commerce, Las Vegas, Nevada (February 24, 1965).

11. R. Reider, "Kiwi-TNT 'Explosion'," LA-3351 (Official Use Only), Los Alamos Scientific Laboratory (July 1965).

12. F. W. Sanders, "Gamma Dose Rate Measurements—Kiwi Transient Nuclear Test," LA-3446, Los Alamos Scientific Laboratory (December 1965).

13. P. K. Lee and R. V. Fultyn, "Kiwi Transient Nuclear Test Dose Rate Survey," LA-3519-MS, Los Alamos Scientific Laboratory (March 1966).

14. U. S. Department of Commerce, Weather Bureau, "Meteorology and Atomic Energy," (prepared for U. S. Atomic Energy Commission), U. S. Government Printing Office, Washington, D. C. (July 1955).

15. E. A. Bryant, J. E. Sattizahn, and G. F. Wagner, "Radiochemical Measurements on Kiwi-TNT," LA-3290 (Confidential RD), Los Alamos Scientific Laboratory (May 1965).

16. R. W. Henderson and R. V. Fultyn, "Radiation Measurements of the Effluent from the Kiwi-TNT Experiment," LA-3395-MS, Los Alamos Scientific Laboratory (October 1965).

17. O. G. Sutton, *Micrometeorology*, McGraw-Hill Book Co., Inc., New York (1953).

18. F. Pasquill, *Atmospheric Diffusion*, D. Van Nostrand Co., Ltd., London (1962).

19. R. W. Henderson and R. V. Fultyn, "Radiation Measurements of the Effluent from the Kiwi-B4D-202 and -B4E-301 Reactors," LA-3397-MS, Los Alamos Scientific Laboratory (August 1965).

APPENDIX
Cloud Dimension Data Analysis

The locations of the cameras used exclusively to photograph the cloud for dimensional analysis were as follows:

East camera tower, 95.5°, 10,000 ft, 16-mm film, 12 frames/sec.

Control Point Building roof, 168°, 10,200 ft, 16-mm film, 24 frames/sec, and 70-mm film, 1 frame every 2 seconds.

North portable camera station, 29.5°, 11,200 ft, 16-mm film, 24 frames/sec.

R-MAD Building roof, 117.5°, 13,100 ft, 70-mm film, 1 frame every 2 seconds.

South portable camera station, 210°, 11,554 ft, 70-mm film, 1 frame every 2 seconds.

The azimuths and distances are from the Kiwi-TNT test point. All cameras were operated by EG&G personnel.

Analysis of the 16-mm film used a specially modified projector which allowed the film to be studied a frame at a time. This projector also contains a frame counter which allowed accurate determination of the time a specific frame was made.

The camera-projector system was treated as a simple lens system of unknown focal length. To obtain correct cloud dimension data, it was therefore necessary to have a reference object, of known size and distance, in the photograph. Fortunately, there were a meteorological tower and water tower at the test cell complex, and at least one of these appeared in all photographs used to obtain dimensional data. The analysis was as follows (see Fig. A.1).
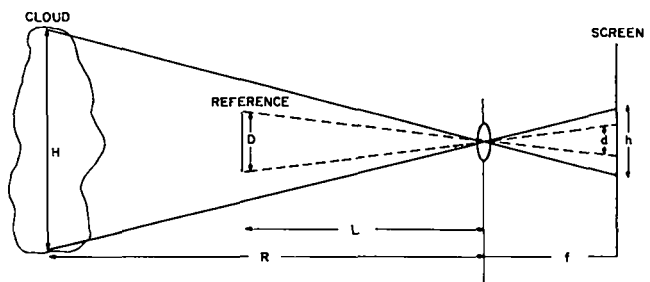

Fig. A.1. Geometric relationships assumed in determining cloud dimensions.

H = actual height of cloud
h = height of cloud on projection screen
D = actual height of reference object
d = height of reference object on screen
L = distance from camera to reference object
R = distance from camera to cloud
f = equivalent focal length of optical system.

Using the simple lens formula,

$$\frac{L}{D} = \frac{f}{d} \; ; \text{ and } \frac{R}{H} = \frac{f}{h} \tag{A.1}$$

$$\frac{Ld}{D} = f = \frac{Rh}{H} \tag{A.2}$$

$$H = \frac{RDh}{Ld} \tag{A.3}$$

The heights and distances of the reference objects were known. The distance to the cloud was calculated using the meteorological data given in Chapter III. From the photographs, a preliminary estimate of cloud altitude vs. time was made. An accurate track of the cloud was made using the wind speed and direction for each altitude, and from this track the cloud-to-camera distance could be ascertained.

Data obtained in this fashion are listed in Table A.I, and plotted in Figs. 2, 3, and 4.

TABLE A.I. CLOUD DIMENSION DATA

Time After Event (sec)	Distance from Test Point to Cloud Center (feet)	Horizontal Diameter (feet)	Vertical Diameter (feet)	Top Altitude (feet)	Center Altitude (feet)	Bottom Altitude (feet)
1	28.7			111		
2	62.4			199		
3	96.1	168	243	243	121	0
4	130	158	275	286	148	11
5	164	158	318	329	170	11
6	197	175	306	372	219	66
7	231	192	338	414	245	76
8	265	208	347	456	282	109
9	298	225	357	476	298	119
10	332	242	337	518	349	180
20	669	423	644	873	551	229
30	1024	612	768	1034	650	266
45	1556	640	927	1329	865	402
60	2089	727	853	1560	1133	706
90	3256	979	1096	2002	1454	906
120	4423	1017	1429	2610	1896	1181
150	5083	1728	1728	3072	2208	1344
180	5743	1989	1915	3431	2474	1516
210	6403	1812	1987	3472	2479	1486
240	7063	2034	1973	3517	2530	1544
270	7723	2159	2175	3640	2552	1465
300	8383	2567	2202	3717	2615	1514
330	9043	2722	2286	3857	2714	1572
360	9805	2941	2418	4046	2838	1628
390	10570	3292	2707	4087	2733	1380
420	11330	3596	2640	4172	2851	1531
450	12090	3979	2618	4199	2890	1581
480	12850	4379	2813	4276	2869	1463
510	13620	4655	2900	4407	2957	1507
540	14380	5665	2986	4459	2966	1473